

Master thesis : Microstructural characterization of the laser clad 316L+SiC composite coating

Auteur : Saggionetto, Enrico

Promoteur(s) : Mertens, Anne

Faculté : Faculté des Sciences appliquées

Diplôme : Cours supplémentaires destinés aux étudiants d'échange (Erasmus, ...)

Année académique : 2018-2019

URI/URL : <http://hdl.handle.net/2268.2/8213>

Avertissement à l'attention des usagers :

Tous les documents placés en accès ouvert sur le site le site MatheO sont protégés par le droit d'auteur. Conformément aux principes énoncés par la "Budapest Open Access Initiative"(BOAI, 2002), l'utilisateur du site peut lire, télécharger, copier, transmettre, imprimer, chercher ou faire un lien vers le texte intégral de ces documents, les disséquer pour les indexer, s'en servir de données pour un logiciel, ou s'en servir à toute autre fin légale (ou prévue par la réglementation relative au droit d'auteur). Toute utilisation du document à des fins commerciales est strictement interdite.

Par ailleurs, l'utilisateur s'engage à respecter les droits moraux de l'auteur, principalement le droit à l'intégrité de l'oeuvre et le droit de paternité et ce dans toute utilisation que l'utilisateur entreprend. Ainsi, à titre d'exemple, lorsqu'il reproduira un document par extrait ou dans son intégralité, l'utilisateur citera de manière complète les sources telles que mentionnées ci-dessus. Toute utilisation non explicitement autorisée ci-avant (telle que par exemple, la modification du document ou son résumé) nécessite l'autorisation préalable et expresse des auteurs ou de leurs ayants droit.



UNIVERSITÀ
DEGLI STUDI
DI PADOVA

Université de Liège – Università degli Studi di Padova

Faculté des Sciences Appliquées – Scuola di Ingegneria

**MICROSTRUCTURAL CHARACTERIZATION
OF THE LASER CLAD 316L + SiC COMPOSITE COATING**

Supervisors:

Prof. Anne Mertens

Prof. Irene Calliari

Student: ENRICO SAGGIONETTO

Academic year 2018/2019

Abstract

In this work the SS316L + SiC Metal Matrix Composites (MMCs) was characterized. Different amount of Silicon Carbide (SiC) was added as reinforcements in a matrix of 316L Stainless Steel (SS316L): 10% in volume and 20% in volume. The composites were produced by Laser Cladding (LC).

An evolution of the characteristics of the cladded deposit was observed with the change of LC process parameters, such as power, scanning speed and powders utilized. For the production of SS316L + 20% SiC deposit the powders were used in original (as-produced) and milled conditions. While for the SS316L + 10% deposit only original powders were utilized.

The deposits with 10% in volume of original SiC powders and with 20% in volume of milled SiC powders exhibit a compact structure with absence of porosity and/or cracks, and good interaction with the substrate.

The characterization was made by means of Optical Microscope (OM), Scanning Electron Microscope (SEM), Differential Thermal Analysis (DTA), Thermo Gravimetry Analysis (TGA), Macro-hardness tests and chemical analysis.

The powders of the two different compositions and after the milling process were characterized, especially by different thermal analysis and microscope observations. Considering their characteristic, the best condition for the Additive Manufacturing (AM) process was chosen and the samples were fabricated by LC. The microstructural characterization on the deposits revealed the formation of carbides that reinforce the matrix. The morphology and the composition of phases of the different deposits were compared by using microscope observations and thermal analyses.

Dedicato ai miei nonni Giancarlo e Antonietta

Acknowledgments

I want to acknowledge the University of Padova and especially prof. Irene Calliari for making the Erasmus possible and the University of Liège for welcoming me. An especial acknowledge is addressed to prof. Anne Mertens for supervising my Thesis and my work in Liège.

I want to thank all the 'Metallic Material Science' team: Jérôme Tchoufang Tchoundjang, Hakan Paydas, Olivier Dedry, Sylvie Reginster, Jocelyn Delahaye, Sylvie Salieri, Rosine Pirson. I appreciated all the moments spend with you in the office, in the laboratory and in the common room. Thanks also to Onur Ertuğrul from Turkey for the collaboration we have had during his stay in Liège. A big special thanks for helping me and for standing me go to my tutor Tommaso Maurizi Enrici, he has transmitted me all the passion he has for this job.

A big thanks for giving me the opportunity to do this experience and for giving me the support in all the moments go to my family: Antonio, Federica, Giorgio and Martina.

Thanks to all the French, Spanish and Italian friends known during the Erasmus period with whom I shared unforgettable moments.

Finally, I want to thank Liège, the 'cité ardente' (now I understand what it means) and the Belgian people, I will never forget you.

TABLE OF CONTENTS

<i>Abstract</i>	3
<i>Acknowledgments</i>	7
1 INTRODUCTION	17
2 STATE OF ART.....	19
2.1 Powder Metallurgy (PM).....	19
2.1.1 Additive Manufacturing (AM)	24
2.1.1.1 Laser Cladding (LC).....	27
2.2 Materials by Additive Manufacturing	28
2.2.1 Metal Matrix Composites (MMCs)	28
2.2.2 Importance of reactions	29
2.3 Utilized Materials	33
2.3.1 SS316L in classical and in Additive Manufacturing	33
2.3.1.1 Effect of addition of carbide-forming element	37
2.3.2 Silicon Carbide (SiC).....	39
3 EXPERIMENTAL METHODS	41
3.1 Original Powders	41
3.1.1 316L Stainless Steel (SS316L)	41
3.1.2 Silicon Carbide (SiC).....	42
3.2 Milled Powders.....	43
3.2.1 SS316L + 20% SiC.....	44
3.2.2 SiC	45
3.3 Deposit fabrication	46
3.3.1 SS316L + 10% SiC.....	50
3.3.2 SS316L + 20% SiC.....	51
3.4 Microstructural characterization.....	54
3.4.1 Samples preparation	54
3.4.2 Optical Microscope (OM) and Stream Analyse Software	57
3.4.3 Scanning Electron Microscope (SEM)	57
3.5 Differential Thermal Analysis (DTA)	58
3.6 Hardness test.....	60

4 RESULTS.....	61
4.1 Powders characterization.....	61
4.1.1 Original powders	61
4.1.1.1 316L Stainless Steel powder.....	61
4.1.1.2 Silicon Carbide powder	63
4.1.1.3 SS316L + 10% SiC powder.....	64
4.1.1.4 SS316L + 20% SiC powder.....	67
4.1.2 Milled powders	69
4.1.2.1 SS316L + 20% SiC powder.....	69
4.1.2.1 Silicon Carbide powder	74
4.2 Laser cladded deposits characterization	78
4.2.1 Cladded deposit SS316L + 10% SiC.....	78
4.2.1.1 Microscope observations	78
4.2.1.2 Thermal analysis.....	92
4.2.1.3 Macrohardness.....	98
4.2.2 Cladded deposit SS316L + 20% SiC.....	99
4.2.2.1 Microscope observations	99
5 DISCUSSION.....	109
5.1 Role of oxygen contamination.....	109
5.2 Optimization of cladded deposit.....	114
5.3 Evolution of SS316L with SiC addition	116
6 CONCLUSIONS	123
7 PROSPECTS	125
8 REFERENCES.....	127
9 ANNEXES	131
Annex 1: Datasheet SS316L powder.....	131
Annex 2: Datasheet SiC powder.....	132

List of figures

Figure 1: Gas atomizator and powders by atomization [4][5]	21
Figure 2: Powders by chemical methods [7][8]	21
Figure 3: Production routes in Powder Metallurgy [1]	23
Figure 4: Laser Additive Manufacturing processes of metallic components [11]	25
Figure 5: Laser Sintering schematic machine [11]	26
Figure 6: Laser Melting schematic machine [13]	26
Figure 7: Laser Cladding schematic machine [16]	27
Figure 8: SS316L/TiC composite [20]	29
Figure 9: SS316L/CeO ₂ composite [21]	30
Figure 10: SS304/Al ₂ O ₃ composite [22]	30
Figure 11: SS316L/WC composite [24]	31
Figure 12: SS316L/SiC composite	32
Figure 13: AISI Austenitic Grades - Type 300 [30]	33
Figure 14: Correlation between G, R and the microstructure [31]	34
Figure 15: Austenitic Stainless Steel microstructures [33]	35
Figure 16: Microstructure in an as-cast Fe-25Cr-5Mo-0.82C alloys [34]	36
Figure 17: Microstructure in laser cladding coating of SS316L [35]	36
Figure 18: M ₇ C ₃ carbide [36]	37
Figure 19: M ₆ C eutectic carbide [37]	38
Figure 20: M ₂ C eutectic carbide [37]	38
Figure 21: MC eutectic carbide [37]	39
Figure 22: SS316L powder	41
Figure 23: SiC powders at different magnification	42
Figure 24: Milling equipment [43]	43
Figure 25: Example of powders on a disc	44
Figure 26: DUOCLAD VI LF 2000 [24]	46
Figure 27: (a) Feeding towers [24], (b) Turntable	47
Figure 28: Coaxial nozzle by IREPA [24]	48
Figure 29: Laser cladding schematic process	48
Figure 30: Deposit analysed in this study	49
Figure 31: Laser cladding parameters	50
Figure 32: Deposit S10.0	51
Figure 33: Deposits S20.0, S20.06, S20.07	52
Figure 34: Cut deposits	54
Figure 35: Samples for DTA tests	55
Figure 36: Characteristic of samples for DTA tests	55
Figure 37: STRUERS equipment [48]	56
Figure 38: Samples after preparation	56
Figure 39: Olympus BX60 [49]	57
Figure 40: Phillips XL30 FEG-ESEM [50]	57
Figure 41: NETZCH STA 449C Jupiter for DTA tests [51]	58

Figure 42: EMCO MIC 010 [52].....	60
Figure 43: Particle size distribution of 316L powders.....	61
Figure 44: DTA and TG heating curve for SS316L powder.....	62
Figure 45: DTA cooling curve for SS316L powder	62
Figure 46: Optical Microscope observation on SS316L after DTA test.....	63
Figure 47: Particle size distribution of SiC powders	63
Figure 48: DTA and TG heating curve for SS316L+10%SiC powders	64
Figure 49: DTA cooling curve for SS316L+10%SiC powder.....	65
Figure 50: Optical microscope observation on SS316L+10%SiC powders after DTA tests	66
Figure 51: DTA and TG heating curve for SS316L+20%SiC powders	67
Figure 52: DTA cooling curve for 316L+20%SiC powder	67
Figure 53: Optical microscope observation on SS316L+20%SiC powders after DTA tests	68
Figure 54: Stage 1 (30 min milling).....	69
Figure 55: Stage 2 (1 h milling).....	70
Figure 56: Stage 3 (2 h milling).....	71
Figure 57: Stage 4 (4 h milling).....	72
Figure 58: Stage 5 (6 h milling).....	73
Figure 59: DTA & TG heating curves for SS316L+20%SiC powders	74
Figure 60: SEM micrograph of different milling on SiC powders	75
Figure 61: DTA heating curve for SS316L original + 20%SiC milled powders.....	76
Figure 62: XRD on powders	77
Figure 63: Overview of sample S10.0	78
Figure 64: Optical microscope observations on S10.0	79
Figure 65: SEM micrograph of sample S10.0.....	80
Figure 66: Track zones.....	81
Figure 67: Chemical analyse zone on the track	82
Figure 68: Composition profile on the track zone	82
Figure 69: Heat Affected Zone	84
Figure 70: Chemical analyse on the heat affected zone.....	85
Figure 71: Composition profile [%] on the heat affected zone.....	85
Figure 72: EBSD on sample S10.0	87
Figure 73: EBSD phase map vs SEM micrograph.....	88
Figure 74: Investigation on the EBSD zone.....	89
Figure 75: Compositions of the points on the EBSD zone	90
Figure 76: Chemical analyse on the EBSD zone	90
Figure 77: Profile compositions in the EBSD zone	91
Figure 78: DTA and TG heating curves for S10.0.....	92
Figure 79: DTA cooling curves for S10.0.....	93
Figure 80: Optical Microscope observations on sample 'Surface 3' after DTA.....	94
Figure 81: Optical Microscope observations on sample 'Core 1' after DTA	95
Figure 82: DTA heating curves up to peak H3	96
Figure 83: Observations on sample 'Core 2' after thermal analyse up to 1240 °C	97
Figure 84: Macrohardness grid on left section of S10.0.....	98
Figure 85: Macrohardness: SS316L+10%SiC vs SS316L.....	98
Figure 86: Overview of the sample S20.0.....	99

Figure 87: Optical microscopy observation on sample S20.0	99
Figure 88: SEM observations on sample S20.0	100
Figure 89: Chemical analyse 1 on sample S20.0	101
Figure 90: Composition profile 1 on sample S20.0	101
Figure 91: Chemical analyse 2 on sample S20.0	102
Figure 92: Composition profile 2 on sample S20.0	103
Figure 93: 2D pores distribution in the sample S20.0.....	104
Figure 94: 3D pores distribution in the sample S20.0.....	104
Figure 95: Dimensional evolution of the pores in the sample S20.0	105
Figure 96: Optical microscope observations on the sample S20.06	106
Figure 97: Optical microscopy observations on the sample S20.07	107
Figure 98: DTA & TG heating curves for SS316L+20%SiC powders	110
Figure 99: Focus on DTA H1 heating peak	110
Figure 100: Ellingham diagram [54].....	111
Figure 101: Air between powders	112
Figure 102: Evolution of SS316L+20%SiC cladded deposit	115
Figure 103: Track microstructure on sample S10.0.....	116
Figure 104: Heat affected zone microstructure on sample S10.0	117
Figure 105: Schematic reconstruction of a single grain in the track and in the heat affected zone.	118
Figure 106: DTA & TG heating curves of SS316L+10%SiC cladded deposit	119
Figure 107: Focus on peak H4	120
Figure 108: Focus on peak H3	121
Figure 109: Phases present on samples S20.0 and S20.06.....	122

List of tables

Table 1: Chemical composition of the SS316L powder (Annex 1).....	41
Table 2: Chemical composition of the SiC powder (Annex 2).....	42
Table 3: Milling parameters for SS316L+20%SiC.....	44
Table 4: Milling stage for SS316L+20%SiC.....	44
Table 5: Milling parameters 1 for SiC.....	45
Table 6: Milling parameters 2 for SiC.....	45
Table 7: Milling parameters 3 for SiC.....	45
Table 8: Parameters for cladded deposit of SS316L+10%SiC.....	50
Table 9: Geometric characteristic of S10.0.....	51
Table 10: Parameters for cladded deposit of SS316L+20%SiC.....	51
Table 11: Geometric characteristic of S20.0, S20.06, S20.07.....	53
Table 12: DTA tests on powder.....	59
Table 13: DTA tests on deposit.....	59
Table 14: Principal heating peaks for SS316L powder.....	62
Table 15: Principal cooling peaks for SS316L powder.....	62
Table 16: Principal heating peaks for SS316L+10%SiC powder.....	64
Table 17: Principal cooling peaks for 316L+10%SiC powder.....	65
Table 18: Principal heating peaks for SS316L+20%SiC powder.....	67
Table 19: Principal cooling peaks for SS316L+20%SiC powder.....	68
Table 20: Principal heating for 316L+20%SiC milled powders.....	74
Table 21: Principal heating peaks for 316L original + 20%SiC milled.....	76
Table 22: Atomic compositions [%] on the track profile.....	83
Table 23: Atomic compositions [%] on the heat affected zone.....	86
Table 24: EBSD phases.....	86
Table 25: Compositions in the EBSD zone.....	91
Table 26: Principal heating peaks for S10.0.....	92
Table 27: Principal cooling peaks for S10.0.....	93
Table 28: Atomic Compositions 1 in sample S20.0.....	102
Table 29: Composition 2 in the sample S20.0.....	103
Table 30: Atomic composition [%] of phases on S10.0 microstructure.....	117
Table 31: Atomic composition [%] of the grain and the cell border in the heat affected zone.....	118
Table 32: Atomic composition [%] of phases on S20.0 and S20.06 cladded deposit.....	122

1 INTRODUCTION

Powder Metallurgy (PM) is an ancient materials processing technology. This technology has evolved from the traditional processes such as die compaction, injection moulding, rolling, hot/cold isostatic pressing etc. to the recent Additive Manufacturing (AM), popular known as 3D printing. This technology has developed in the last 25 years, within the new industrial revolution in aerospace, defence, automotive and medical industries. The success of this materials processing is due to the many advantages in comparison with classic processes, like near net shaping, production speed, freedom of design and cost saving. All those advantages have been enhanced with the possibility of the Additive Manufacturing technologies and opening doors for new structures and applications. Furthermore, new materials have been developed in Additive Manufacturing, that were impossible to cast in the past. In fact, with the invention of technologies capable of combining very different raw materials to create a new product, the chase by major industries worldwide towards Additive Manufacturing has begun. Many achievements have been made in the field of Metal Matrix Composites (MMCs), thanks to the development of technologies such as Laser Cladding, Selective Laser Melting, Direct Metal Laser Sintering etc.

The main feature that makes Metal Matrix Composites from laser technologies attractive is the possibility to create products with tailored properties by varying the raw materials. Depending on the type of matrix and reinforcement, the microstructure of the material changes and consequently the mechanical, physical and chemical properties. Currently, important progresses have been made in this field, but many behaviours of the matrix/reinforcement interaction have not been fully understood and only few alloys can be reliably printed.

In this study laser cladding process has been applied to reinforce 316L Stainless Steel with SiC particles, in the hope to improve the wear resistance. Particular attention was focused on the fabrication and the microstructure of two different composition of the cladded deposits. The composite materials SS316L + 10% (in volume) and SS316L + 20% (in volume) of SiC powders were characterized by means of several characterization technique. A tailored powder preparation by milling was set in order to fabricate a sound deposit by Laser Cladding machine. The chemical interactions between the two powders during the Additive Manufacturing process were clarified. Those considerations have played an important role in the difficulty fabrication of the composite.

2 STATE OF ART

2.1 Powder Metallurgy (PM)

Powder metallurgy (PM) is a peculiar branch of the metallurgy, in which the production and utilization of metal powders constitute the main interest. The term 'Powder Metallurgy' has an umbrella meaning since it covers a wide range of manufacturing processes for metallic components.

Traditionally, powder metallurgy is divided in two industrial categories, ferrous precision parts and hard metals used on the automotive industry. The major tonnage produce in PM consists of ferrous parts ($1 \cdot 10^6$ t of iron and steel) that generate an annual turnover of an estimated $15 \cdot 10^9$ \$ worldwide. While hard metal parts generate an estimated turnover of about $18 \cdot 10^9$ \$ at an annual tonnage of 75 000 t. Both product groups have started their growth in the 1920s with the combination of tungsten carbide (WC) with iron-base alloys by Schroter and Skaupy in Berlin, and in the 1930s with the production of oil pump gears for cars in United States. During World War II, in Germany metallurgists adapted compacting techniques known for ceramic components to metallic powders. PM had a large expansion after the war in the car industry sector, with the introduction of tailored alloy grades such as steel made from Ni-Cu-Mo diffusion bonded powders and by Cr or Cr-Mo alloyed types, by combining sintering and heat treatments. When the 'diesel crisis' started, diesel engine cars were banned from the city centres and they have begun to be replaced by electric or hybrid cars; so, PM industry has to be prepared for a fundamental change of its product. Today the challenge of PM is to find new applications, thanks to of its flexibility regarding properties, geometries, materials, and processing [1].

Characteristics of PM like prize or uniqueness and captive applications are the main advantages of his processes. The metal powder industry competes directly with other metalworking practices such as casting, forging, machining. Its cost is advantageous on making complex shaped parts and minimizes the need for machining and other conventional processes. PM parts have a good surface finishing and they can be treated to increase wear resistance or strength. The process provides part-to-part reproducibility and controlled microstructure. Moreover, it allows to fabricate materials that are difficult to process by other techniques. [2]

The aim of manufacturing high quality component by PM is to control the properties of the powder, such as particle size distribution, particle morphology and composition. Generally, the use of powders for specific engineering applications requires properties such as formability, apparent density, compressibility and weldability [3].

Most of metals are available in form of powders, in different shape and size that depends on the way they were produced. There are three main methods of metal powder production: mechanical, chemical and physical. The mechanical methods include various type of atomization and milling processes. The main principle of all atomization technologies is the fragmentation of a stream of molten metal by the impact of water, gas, oil or by mechanical dispersion. The molten metal is divided in small droplets that crystallize in flight. Gas atomization is used when water atomization is not possible because of the reactivity of the metal. Powders obtained by gas atomization process present a spherical or near to spherical shape (Figure 1), necessary for many AM processes. Today the most used gases are nitrogen and argon. Nitrogen is not completely inert. On the other hand, the insolubility of argon in metals can lead to porous or hollow spheres, so depending on the desired final product, a correct preliminary choice must be made. With water atomization process, particles have irregular shape that provides good green strength by interlocking of the particles (Figure 1). The gas atomization process involves many variables such as the temperature, the diameter of the molten metal stream and the geometry of the nozzle. Oil atomization is also used but requires special safety measures. Its advantage is that the oxidation of the powder surface can be avoided. Another recent process is the plasma atomization, but it has many limitations. Other types of atomization process are centrifugal atomization, in which centrifugal force is used to disperse the molten metal. Finally, the production of fine chips by machining techniques such as milling or turning is an easy way to produce powders but it is also expensive. Milling consists of repeated welding, fracturing and rewelding of powder particles in a high energy mill. The average particle size for most metals produced by milling is $>100\ \mu\text{m}$ depending on the ductility of the powder. Typical mills are tumbling ball mills, vibratory mills and attritors. As milling is an energy-intensive process, the risk of impurities incorporated by wear of the mill and balls is high. The advantage of this process is the possibility to use different raw materials and develop new materials and alloys such as amorphous alloys, intermetallic compound and metal matrix composites [1].

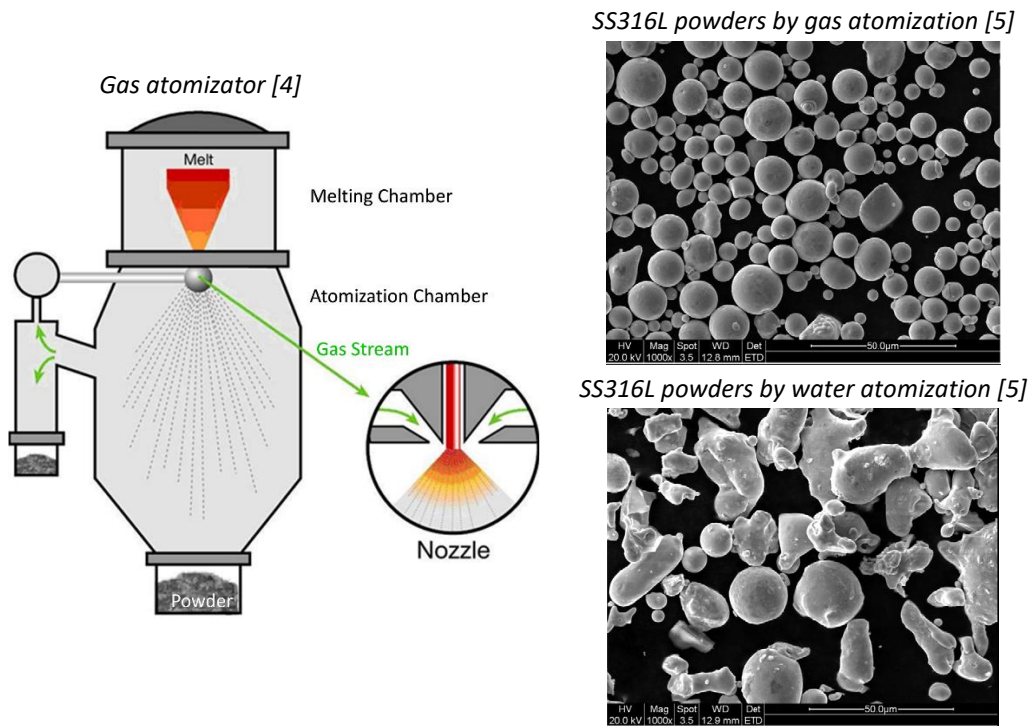


Figure 1: Gas atomizer and powders by atomization

The physical and chemical methods include electrolysis, carbonyl process and plasma spheroidization. The first consists in allocation of electrode components, which occur when the solution or electrolyte melt carry current. The limitation of this process means an ability to receive pure metal, but not alloys. The carbonyl process allows to produce nickel and iron powder by a reaction of the crude metal with gaseous carbon oxide under pressure and high temperature. Finally, the plasma spheroidization is used as additional treatment in order to change the particles shape to spherical [6]. In Figure 2 are shown some powders by chemical production methods.

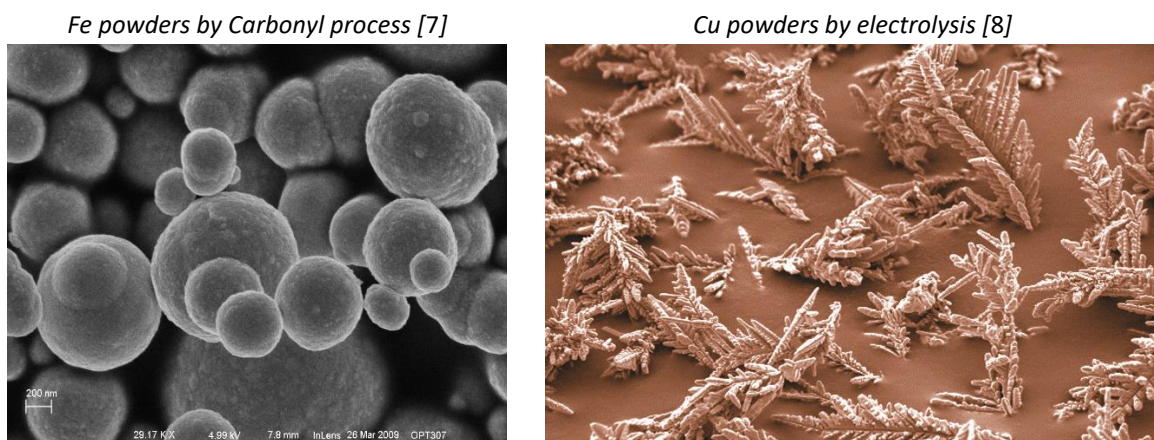


Figure 2: Powders by chemical methods

The different applications for metal powders usually require the appropriate physical, chemical and technological properties. Particle size, particle shape and structure and specific surface determine to a considerable extent of the properties of finished compacts from powder. They also have a strong effect upon the behaviour of powder during processing [9].

Concerning particle size, different definitions are used: the sieve diameter which is the width of the minimum square aperture through which the particle will pass in sieve analysis and the projected area diameter which is the diameter of a circle having the same projected area as the particle in random orientation. Chemical properties can be characterized by two categories of analysis: bulk analysis gives the general chemical composition of the powder using a coupled plasma optical emission spectrometry or X-Ray fluorescence spectrometry, surface analysis gives information about the surface composition using X-Ray photo electron spectroscopy or Scanning Electron Microscopy (SEM) combined with energy dispersive X-Ray spectrometry (SEM-EDX). Technological properties can be characterized by various ISO or ASTM standard methods. The most important technological properties are flow behaviour, apparent density and compressibility [1,10].

PM components produced from corrosion-resistant alloys are a growing area of PM applications. Stainless steel PM alloys has a high demand in many industries, including automotive, chemical processing, medical, aerospace and recreational. Processing of PM stainless steel is critical to achieve satisfactory corrosion resistance: many cases of underperforming of these steel parts in terms of corrosion resistance are due to improper process. Improved understanding of the PM of Stainless Steel can extend the use of PM technology in terms of economic value and in applications [10].

The various production routes are depicted in [Figure 3](#).

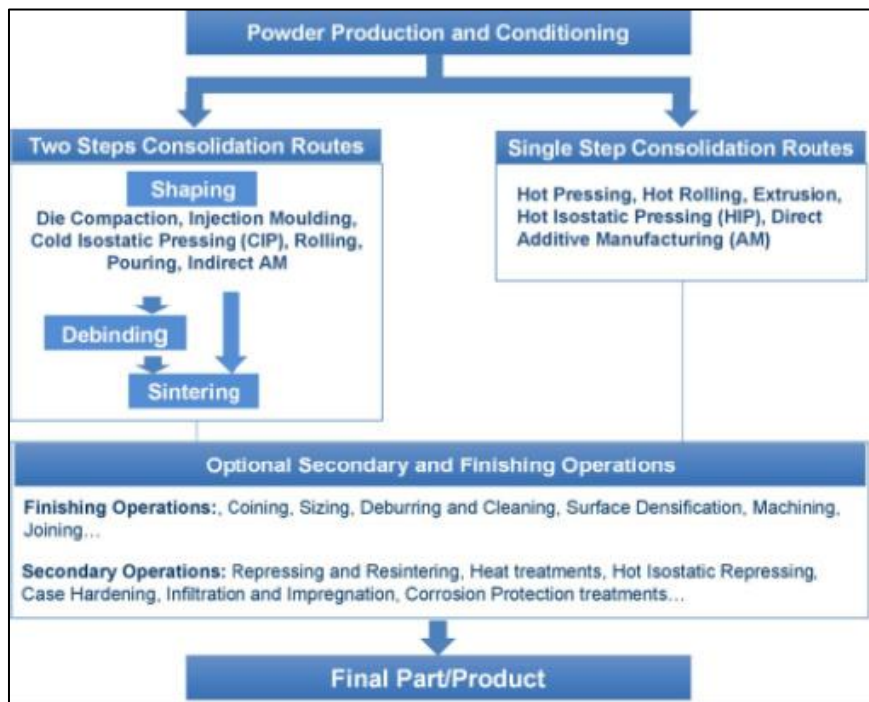


Figure 3: Production routes in Powder Metallurgy [1]

After the powder production, the conditioning step is also important. To proceed to the desired composition of an alloy through the powder route, there are various main alloying paths. Some production methods provide metal powder that require soft milling to obtain a suitable powder. The addition of binders and pressing aids is necessary to provide the desired compaction properties. Blending of powders is performed by dry mixing or mixing of suspension. After mixing, the powders should be handled with special care because de-mixing can be caused by transport, vibration or free falling. If the powders show inadequate flow behaviour, a treatment of agglomeration, spray drying or granulation may be necessary [1].

The consolidation can be developed in two steps or in single step. The first step of the two-step process is the rigid die compaction. It gives the possibility to produce PM components in different shapes and sizes with a low cost compared with other methods. Powders with a low cohesive nature require some quantity of lubricant which can be added in a blending operation. Another method is powder injection moulding, suitable for manufacturing large number of components in different shapes and sizes. It is applied when tolerance and cost are important factors. This technology evolved from the common injection moulding for plastic parts. In the Cold Isostatic Pressing (CIP) the powder is poured into a flexible mould made of rubber that is immersed in a liquid pumped at high pressure. Pressure is transmitted in all directions from the liquid to the powder through the flexible mould.

The dimensional control is in principle less precise than in die compaction, but it gives the possibility to incorporate some metallic parts to the mould to produce a more accurate surface. CIP has become an important process for the production of some PM materials such as molybdenum and tungsten, tungsten heavy alloys and high speed steels. In the rolling process the powder is compressed in a rolling mill. The rolling operation can be carried out at room or elevated temperatures and the set up can be continuous or semi-continuous [3]. After these many types of first step, the second step of a two-step process is the sintering. The sintering is defined as the thermal treatment of a powder or compact at a temperature below the melting point of the main constituent, for the purpose of increasing its strength by bonding the particles together. Sintering can be performed in different variants, depending on the phases present: solid state, reaction, liquid phase, activated. For a PM stainless steel component, the sintering process involves a number of factors such as the type of furnace, temperature or atmosphere. Regarding the consolidation in one step, the main processes are Hot Isostatic Pressing (HIP) and most recently Additive Manufacturing (AM). In HIP a gas medium is used to apply pressure at high temperature to porous part. The combination of pressure and temperature allows achieving virtually full density at lower pressure than CIP and lower temperature than sintering, so the grain growth can be inhibited [1].

2.1.1 Additive Manufacturing (AM)

Additive manufacturing is the name for the rapid prototyping processes, also known as 3D printing. At the beginning, the aim of this technology is to create quickly a basic model from which the final product and further models can be derived. Since the first technique for AM became available in the late 1980s and to fabricate models and prototypes, AM technology has experienced more than 20 years of development. The layer by layer manufacturing technology was first established in the 1971 patent of Ciraud, which is considered as the precursor of 3D laser cladding processes. Nowadays, the development of AM techniques is aiming to produce complex-shaped functionally metallic components, including metals, alloys and Metal Matrix Composites (MMCs) that cannot be easily produced by the conventional methods [11]. A definition given by the ISO/ASTM 52900-15 is: “process of joining materials to make object from 3D model data, usually layer upon layer, as opposed to subtractive manufacturing methodologies”. In this definition there is the key to how AM works. It is that parts are made by adding material layer by layer, each layer is a thin cross-section of the part derived from the original CAD data [12].

AM refers to an advanced technology used for the fabrication of three-dimensional near-net-shaped functional components. This because is viewed as the new industrial revolution, making its

way into a continuously increasing number of industries, such as aerospace, defence, automotive, medical, architecture, art, jewellery and food. This technology does not require moulds, fixtures or tooling that increase the time production. Also, near net shaping minimizes material use and waste. Other advantages and benefits of AM technologies are the production speed, design freedom, cost saving and green manufacturing. Referring to AM for metal component, each AM process has its specific characteristic in terms of useable materials, processing procedures and field of application. The prevailing AM technology for the fabrication of metallic components has three basic processes: Laser Sintering (LS), Laser Melting (LM), Laser Metal Deposition (LMD) (Figure 4).

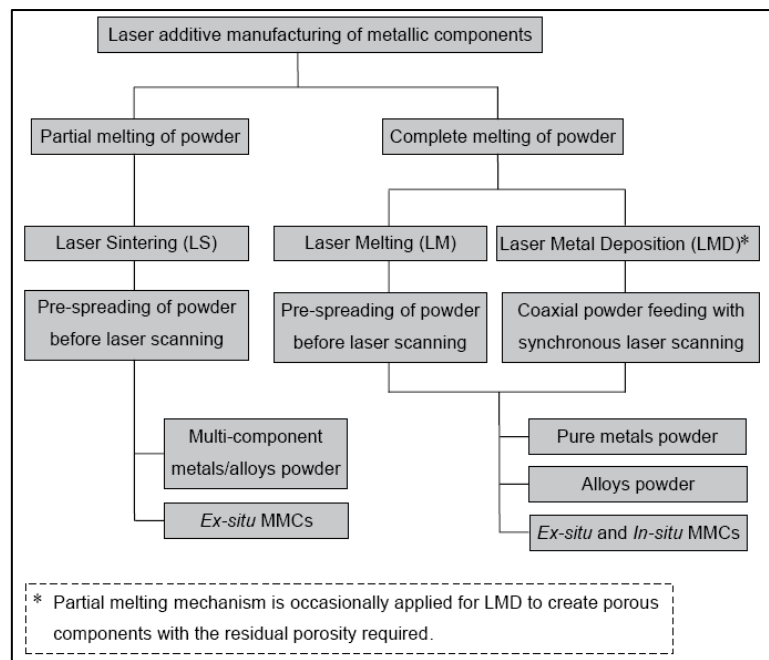


Figure 4: Laser Additive Manufacturing processes of metallic components [11]

Laser sintering (LS) is based on the layer by layer spreading of powder and subsequent Laser Sintering. Normal LS system consists of a laser, an automatic powder layering apparatus and other accessories (Figure 5). Different type of laser can be used, including CO₂, Nd: YAG, fiber laser, disc laser, etc. The choice of the laser has an influence on the consolidation of the powders because the laser absorptivity of materials depends on the laser wavelength and because the laser energy density determines powder densification. The LS process starts with the positioning of a substrate on the building platform. The protective inner gas is fed into the building chamber to reduce oxygen content. Subsequently a layer is deposited on the substrate and the laser beam scans the powder bed surface to form layer-wise profiles according to CAD model. Finally, the previous procedures are repeated and the parts are built layer by layer [11].

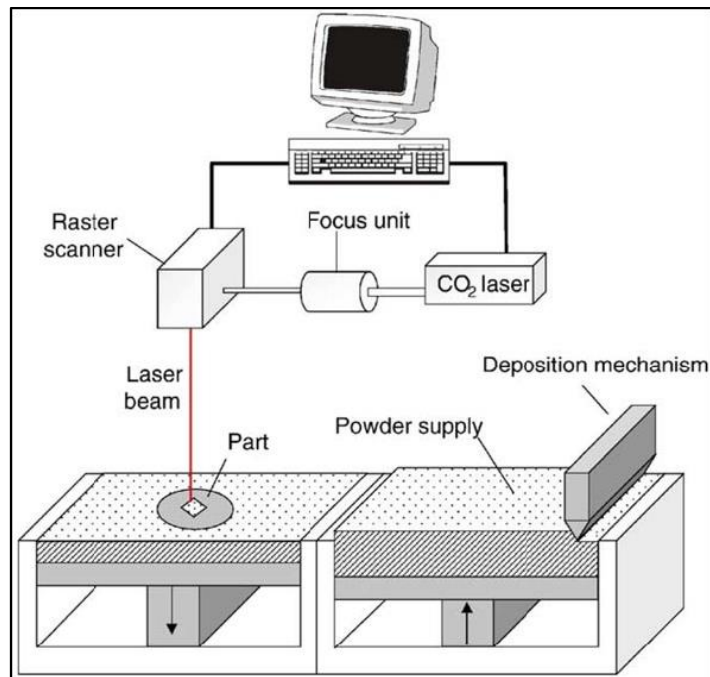


Figure 5: Laser Sintering schematic machine [11]

Laser Melting (LM) (Figure 6) has been developed by the increase of the demand to produce fully dense components with mechanical properties comparable of those of bulk materials. The only difference with LS is based on the complete melting/solidification mechanism. LM requires a high energy level which is realized by applying good beam quality, high laser power and thin powder layer thickness. The disadvantages are the risk for the instability of the molten pool due to the full melting mechanism [11].

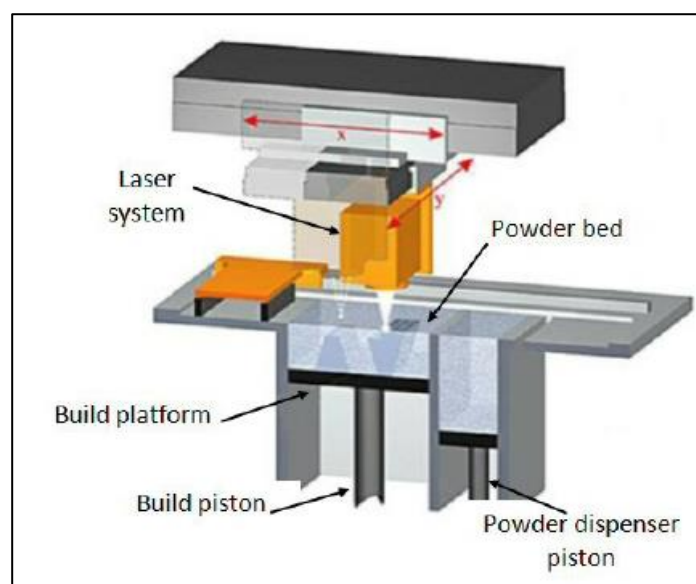


Figure 6: Laser Melting schematic machine [13]

Finally, Laser Metal Deposition (LMD) follows the general principles of Additive Manufacturing, but the difference with LS and LM is the powder supply. In fact, the LMD powder process. the delivery system is designed to deliver powder via the nozzles. A focus on this process is done in the section 2.1.1.1.

2.1.1.1 Laser Cladding (LC)

In order to improve the surface properties of metallic mechanical parts, such as the resistance against wear and corrosion, several thermal surface treatments can be used, such as flame spraying, plasma spraying and arc welding. Depending on the applied technique, common problems are a combination of a poor bonding of the applied surface layer to the base material, porosity, thermal distortion of the workpiece, mixing of the surface layer with the base material and the inability of a very local treatment. One of the techniques that overcomes these problems is Laser Cladding (LC) [14].

The principle behind laser cladding is the formation of the coating by melting the coating material and a thin layer of the substrate with a scanning laser beam normal to the surface. In two-step laser cladding, the coating material is pre-deposited on the substrate and melted with the laser beam to form the coating, while in the single-step the material is injected into the melt pool created by the laser beam and melts to form the coating. The positive effects of laser surface treatments are based on a change of the microstructure of the material composition on the surface layer. The treated area is heated by absorption of energy delivered by the laser beam. The heated layer is self-quenched after passing of the laser beam by diffusion of heat to the cold bulk. The result is a grain refinement and the formation of metastable phases and/or altered microstructures due to the high heating and cooling rates in the surface layer [15].

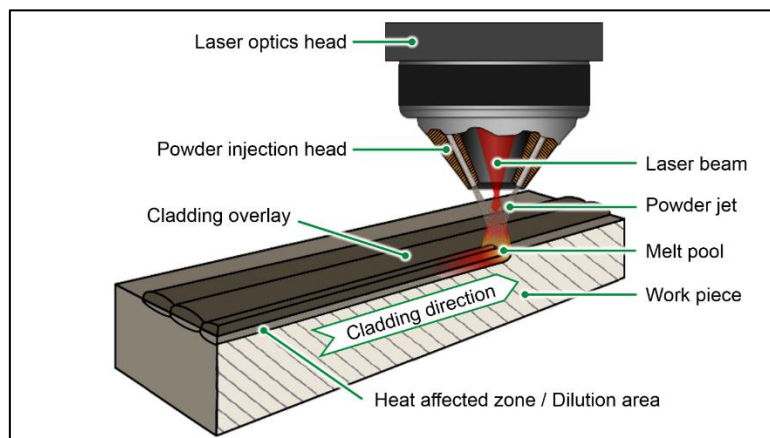


Figure 7: Laser Cladding schematic machine [16]

2.2 Materials by Additive Manufacturing

2.2.1 Metal Matrix Composites (MMCs)

A composite material can be defined as a material consisting of two or more physically and/or chemically distinct, suitably arranged or distributed phases. Generally, the continuous phase is the matrix in which the reinforcing phase is distributed. When the matrix component is a metal, a composite is called Metal Matrix Composite (MMC) [17].

The technologies to manufacture MMCs were still relatively immature by the early 1970s. By the late 1970s, the paradigm for materials development and commercialization began to change. An increased emphasis on affordability and a heightened sensitivity to risk, even in military systems, made it difficult to certify new high performance materials for applications. Research and development of MMCs was reinvigorated in the 1980s, when large technology programs provided a focal point once again for material with the highest performance, such as the National Aerospace Plane in the United States and similar programs in other countries. As a result of these activities, MMCs have found many applications in commercial sectors in the past two decades, such as the ground transportation (auto and rail), thermal management, aerospace, industrial, recreational and infrastructure industries [18].

MMCs have many advantages over monolithic metals including a higher specific modulus, higher specific strength, better properties at elevated temperatures, lower coefficient of thermal expansion and better wear resistance. On the debit side, their toughness is inferior to monolithic metals and they are more expensive at present. MMCs offer a unique balance of physical and mechanical properties. They provide high thermal and electrical conductivity, good resistance to aggressive environments, good impact and erosion resistance and good fatigue and fracture properties. Additional functionalities can be designed into some MMCs through appropriate selection of constituents [19].

MMCs reinforcements can be generally divided into five major categories: continuous fibers, discontinuous fibers, whiskers, wires and particulate. Generally, reinforcements are ceramics, in particular oxides, carbides and nitrides which are used because of their excellent combinations of specific strength and stiffness at both ambient temperature and elevated temperature. In particular, particle reinforcements have assumed special importance for many reasons. Particle reinforced composites are inexpensive as conventional metallurgical processing techniques such as casting or powder metallurgy can be used. They offer the potential for higher usage temperatures than the

unreinforced metal, enhanced modulus and strength, increased thermal stability, better wear resistance and relatively isotropic properties compared to the fiber reinforced composites [19].

Earlier on, the role of the matrix was considered to be that of a binder to ensure strength and stiffness of fibers or other types of reinforcement. Over the years, however, it has been realized that the matrix microstructure and consequently its mechanical properties have a considerable influence on the performance of a composite. This is particularly true on the metal matrix composites because the very act of incorporating a reinforcement can result in change in the microstructure of the metallic matrix and, consequently, in their structural properties such as strength and toughness [18].

2.2.2 Importance of reactions

Some studies are present in the literature on the investigation of composite coatings with a metal matrix reinforced with various elements by AM processes. Typical matrix are SS316L, Ti, Al, SS304, reinforced by TiC, TiB₂, CeO₂, Al₂O₃, SiC. The reactions that occur during the manufacturing process lead to different microstructures and different properties, depending on the materials utilized as matrix and reinforcement.

TiC particles were used to reinforce a matrix of SS316L (Figure 8). In this case, the addition of TiC particles refined the cell size of the TiC/SS316L composites. The reinforced material was well bonded with the SS316L and there were a large number of dislocations near the TiC particles. The abrasion performance of the composite was improved by adding the TiC particles [20].

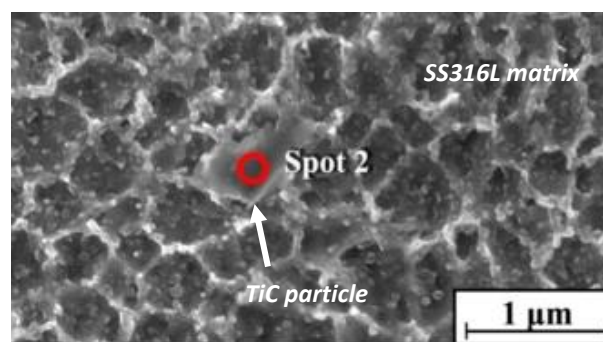


Figure 8: SS316L/TiC composite [20]

The addition of CeO₂ as reinforcements in a matrix of SS316L (Figure 9) does not alter the phase formation, but it affects the microstructure of the composite, which is refined compared with the unreinforced SS316L [21].

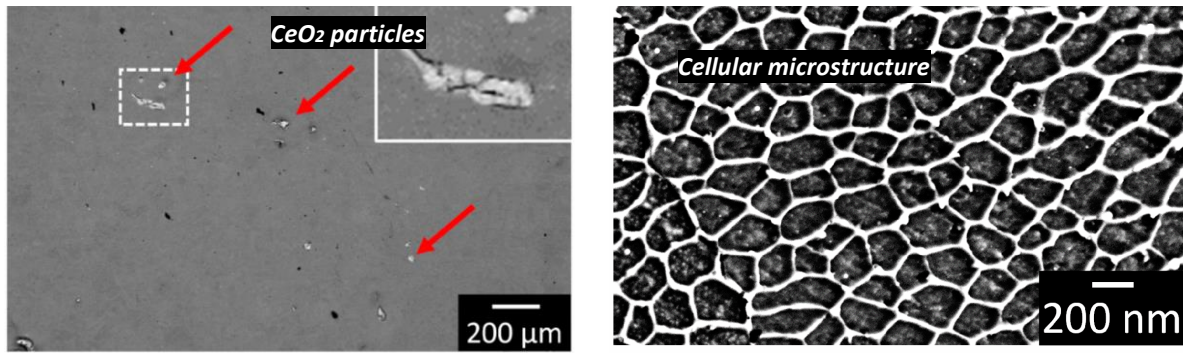


Figure 9: SS316L/CeO₂ composite [21]

The addition of Al₂O₃ in a matrix of SS304 by laser cladding is a suitable technique to obtain defect free coatings with higher hardness, corrosion resistance and wear resistance than conventional SS304. The microstructure is characterized by planar, cellular and dendritic crystals, and fine equiaxed grains (Figure 10) [22].

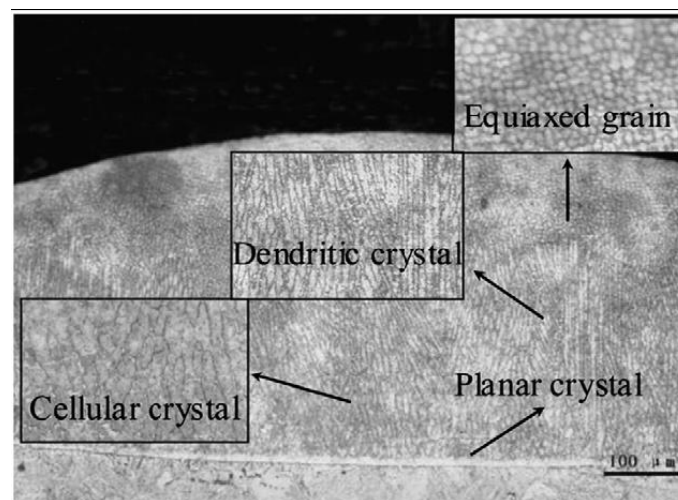


Figure 10: SS304/Al₂O₃ composite [22]

Two important MMCs in terms of wear resistance are SS316L/WC and SS316L/SiC. SS316L/WC composite coatings exhibit a high survival rate of WC powder, due to the limited dissolution of WC in the SS316L matrix (Figure 11). The microstructure is characterized by cellular dendrites. WC particles are surrounded by an interfacial reaction layer enriched with both W and Fe. The result of this deposit is a higher hardness than the reference SS316L. Indeed, different amounts of WC powders were added, up to 20 vol. %: the addition of WC resulted in a marked increase of hardness. A volume fraction higher than 20 vol. % leads to cracks, as a result of the development of internal stresses due to thermal mismatches between the matrix and the reinforcement. [23].

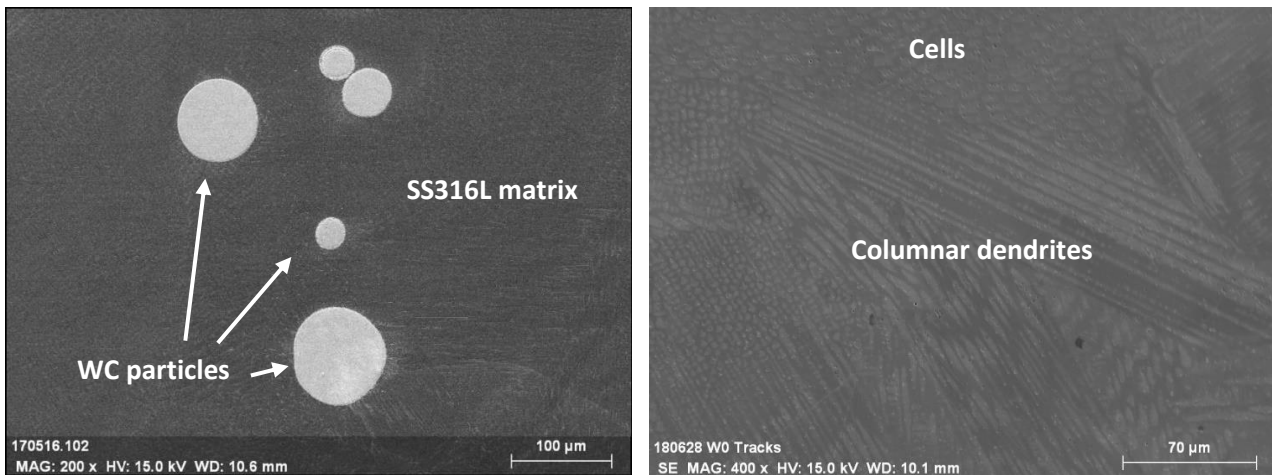


Figure 11: SS316L/WC composite [24]

The behaviour of SiC as reinforcement on 316L Stainless Steel was investigated to improve tribological and mechanical properties. SiC has not the same behaviour of WC as reinforcement of metallic matrix. The formation of iron silicide and the carbon precipitation had negative effect on the chemical and thermal compatibility of the SiC/Fe system. W.M. Tang et al [25] checked the behaviour of Si/Fe system in a range from 1073 to 1373 K. At 1073 K the solid-state reaction between SiC and Fe take place severely. The reaction products are Fe_3Si , graphitic carbon precipitates and $Fe(Si)$. Although several Fe silicides exist, only Fe_3Si was detected in the reaction zone. The reason is attributed to the thermodynamical stability of SiC at the temperature investigated because of the very high bonding strength of Si-C. The decomposition of SiC requires to overcome an activation barrier. During the SiC/Fe reaction, once a layer of SiC is decomposed, Si atoms diffuse away and react with Fe to form a layer of Fe_3Si silicide in front of the constituent C. The Fe concentration at the SiC reaction interface decreases dramatically and the SiC decomposition become more difficult. In order to further decompose SiC, a critical level of Fe concentration is required. Concurrently, the dissociated C atoms, in front of the SiC reaction interface form a small cluster and aggregate. W.M. Tang et al in another study [26] checked the microstructure of the reaction zone of SiC/Fe-20 Cr, after annealing at 1373 K for 20h. The reaction zone is mainly composed of Fe_3Si , Cr_3Si , M_7C_3 -type carbide (M=Cr, Fe) and graphitic carbon. It is divided in two zones, the first zone is rich in Si and Fe and poor in Cr, the second is composed by Fe_3Si , Cr_3Si and M_7C_3 . The second zone has an extremely high Cr content, a low Fe content and no Si content. The Si atoms from the SiC, selectively react with the Fe atoms to form Fe_3Si . Meanwhile, the C atoms selectively react with Cr atoms from the Fe-20 Cr alloy to form the M_7C_3 -type carbide. These selective reactions of Si, C, Fe and Cr is attributed to the high formation enthalpies of Fe_3Si and Cr_7C_3 . These studies lead to the fact that there is a significant dissolution of the SiC particles into an austenitic steel matrix.

Typically, in the SiC/316L sintered composite, SiC particles should be located between the austenite grains. The SS316L matrix was found to interact strongly with the SiC reinforcement with a formation of a low melting Fe-SiC phase. The use of high sintering temperature resulted in an increased amount of Fe-SiC being formed [27].

Various studies were carried out to investigate the laser cladding of SiC as reinforcement of SS316L matrix. The microstructure of austenitic stainless steel with the addition of SiC powders is composed of primary dendrites of austenite phase and interdendritic lamellar M_7C_3 eutectic carbides. The dissolution of SiC phases during laser alloying leads to the formation of phases such as SiC phase, FeSi or Fe_3Si depending on the dilution rate of alloyed layer [28].

Another study presents the fabrication of SiC (5 and 20 wt%) dispersed SS316L by direct laser cladding. A continuous, defect free microstructure enriched in Cr and Si grains is formed. The grain boundary network is composed of very fine SiC, Cr_3C_2 and Fe_2Si (Figure 12) [29].

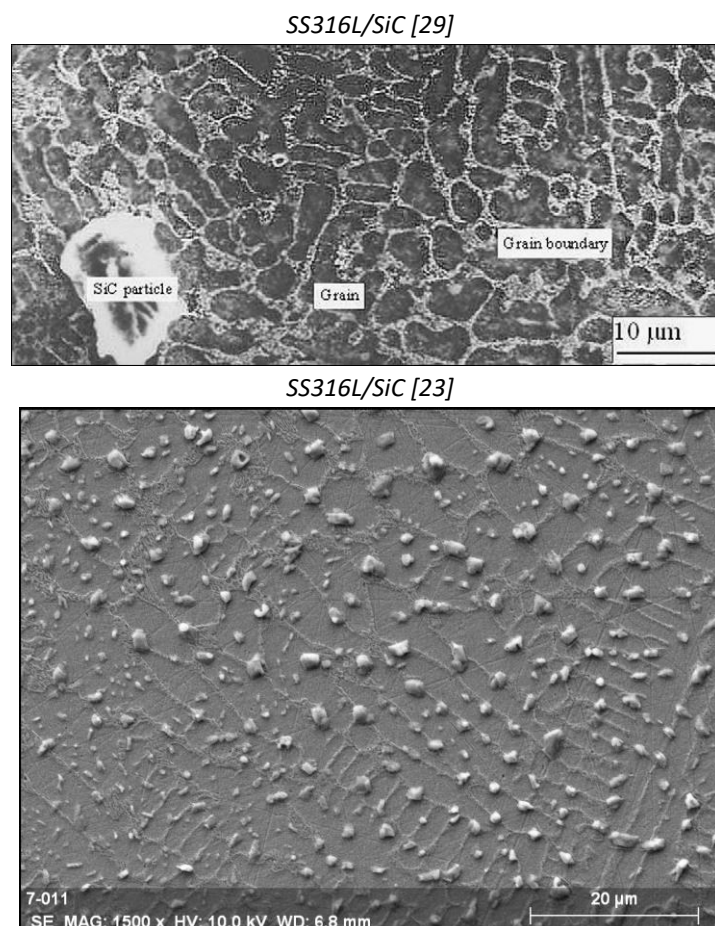


Figure 12: SS316L/SiC composite

2.3 Utilized Materials

2.3.1 SS316L in classical and in Additive Manufacturing

Stainless steel belongs to the family of ferrous alloys and it exhibits peculiar properties and characteristics which are otherwise unavailable in other grades. Three main categories of stainless steel exist: ferritic, austenitic and martensitic. They are different in term of compositional, microstructural and crystallographic features. The basis for stainless steel is the binary iron-chromium system. In particular, the austenitic stainless steels are formed by the addition of a γ austenite stabilizer element, such as nickel or manganese. The most common austenitic alloys are widely known as the 300 series (Figure 13). They exhibit the highest corrosion resistance of the stainless steels group as well as very good thermal properties, very good toughness and weldability.

AISI Type no.	Nominal composition, %				
	C	Mn	Cr	Ni	Others
301	0.15 max.	2.0	16–18	6.0–8.0	
302	0.15 max.	2.0	17–19	8.0–10	
304	0.08 max.	2.0	18–20	8.0–12	
304L	0.03 max.	2.0	18–20	8.0–12	
309	0.20 max.	2.0	22–24	12–15	
310	0.25 max.	2.0	24–26	19–22	
316	0.08 max.	2.0	16–18	10–14	2–3Mo
316L	0.03 max.	2.0	16–18	10–14	2–3Mo
321	0.08 max.	2.0	17–19	9–12	(5 × %C) Ti min.
347	0.08 max.	2.0	17–19	9–13	(10 × %C) Cb-Ta min.

Figure 13: AISI Austenitic Grades - Type 300 [30]

Increasing levels of Cr and Mo increase the resistance to general corrosion, pitting and crevice corrosion, while high levels of Ni and Mo improve resistance to stress corrosion cracking. The weldability of austenitic stainless steel is higher than other grades of stainless steel. Indeed, the stability of the austenite phase lead to less thermal and residual stresses, resulting in weld joints that are ductile and tough even in the as-welded condition. Mo and Cr that are carbide former, which promote carbides in the grain boundaries of the Heat Affected Zone during welding in grades like 316 and 317 [30].

The austenitic stainless steels are used in wide types of applications and industries. Typical areas of use include piping systems, heat exchangers, tanks and process vessels for the food, chemical, pharmaceutical, pulp and paper. Currently metal parts made of 316L are produced by thermomechanical processes, which include casting, rolling, forging, extrusion and welding operations. When the part is unusual in shape or has fine internal features the drawback is the cost that will increase rapidly. The complexity of those parts is impossible to realize with the classical manufacturing processes. In these cases laser cladding process is preferred [31].

The mechanical properties of these parts are determined by the solidification microstructure, that depends on the local solidification conditions.

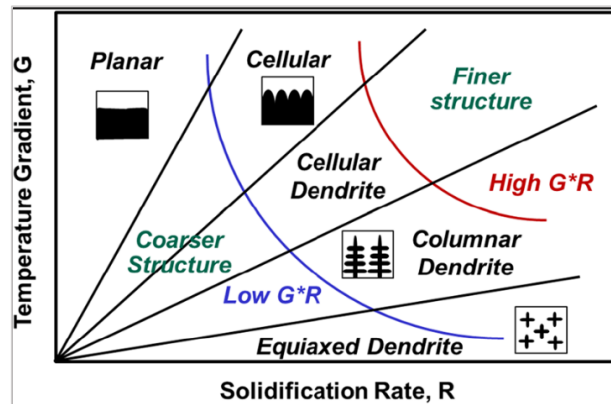


Figure 14: Correlation between temperature gradient G , solidification rate R and the microstructure [31]

During transformation from liquid to solid, the solidification behaviour controls the distribution of solute and the size of the microstructure. Referring to Figure 14, the critical parameters determining the solidification microstructure are the temperature gradient G , solidification rate R , undercooling ΔT and alloy constitution. Depending on these conditions, the microscopical shape of the solid-liquid interface varies from planar to cellular dendritic, to columnar dendritic and to equiaxed dendritic. A planar growth occurs when G is very high or/and R is extremely low value. As R increases, the solidification morphology can shift to cellular, columnar and then equiaxed dendritic. Most metal alloys are solidified in cellular, columnar or dendritic mode in Additive Manufacturing [32].

In the classical manufacturing processes metals solidify as columnar dendritic or equiaxed mode. There has been extensive discussion in literature on the solidification of austenitic stainless steel in classical manufacturing processes. N.Suutala et al. [33] propose a classification of the austenitic microstructure in three categories: microstructure type A where the delta ferrite (that may be the first phase to form upon solidification) is vermicular and located at the cell boundary, microstructure type B where both vermicular and lathy ferrite are present and the delta ferrite is located mainly at the cell axes, microstructure type C where the lathy structure predominated. The general microstructure in type A is very regular due to the solidification substructure and is independent of the presence of delta ferrite. The ferrite has vermicular appearance and is located between cells or cellular dendrites. The ferrite content in type C microstructure is much higher. The structure consists of large grains of the lathy phases. Type B show a ferrite content intermediate between type A and C. The structure can consist of cells full of lathy ferrite surrounded by austenite or of vermicular ferrite embedded in an austenitic matrix (Figure 15).

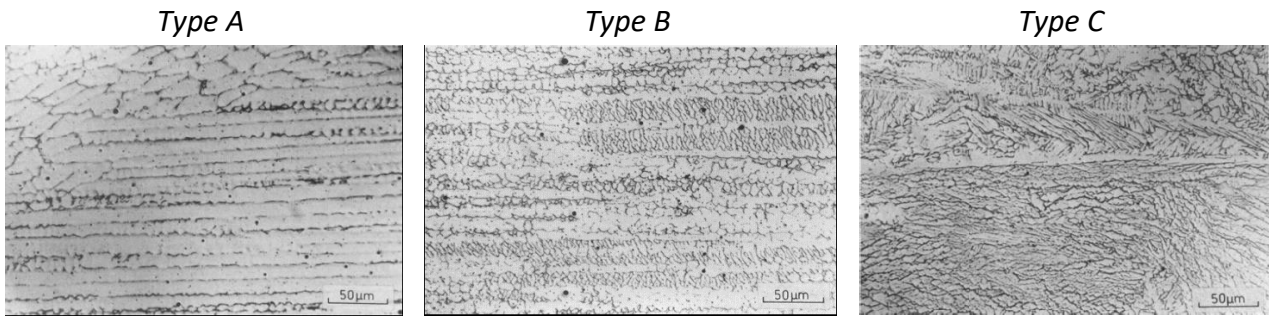


Figure 15: Austenitic Stainless Steel microstructures [33]

Other studies on the system Fe-Cr-Mo-C, in particular on an as-cast Fe-25Cr-5Mo-0.82C alloys, showed the formation of eutectic carbides [34]. The microstructure of the alloy revealed the presence of three distinct areas, as expected in a hypoeutectic as-cast alloys. The alloy consists of primary dendrites with secondary and ternary branches of Fe-Cr-Mo solid solution and eutectic carbides in the interdendritic zones. Dendrites can exhibit equiaxed shapes in top and in the bottom of the ingot, while columnar dendrites are present in the middle (Figure 16), as explained in the description of Figure 14.

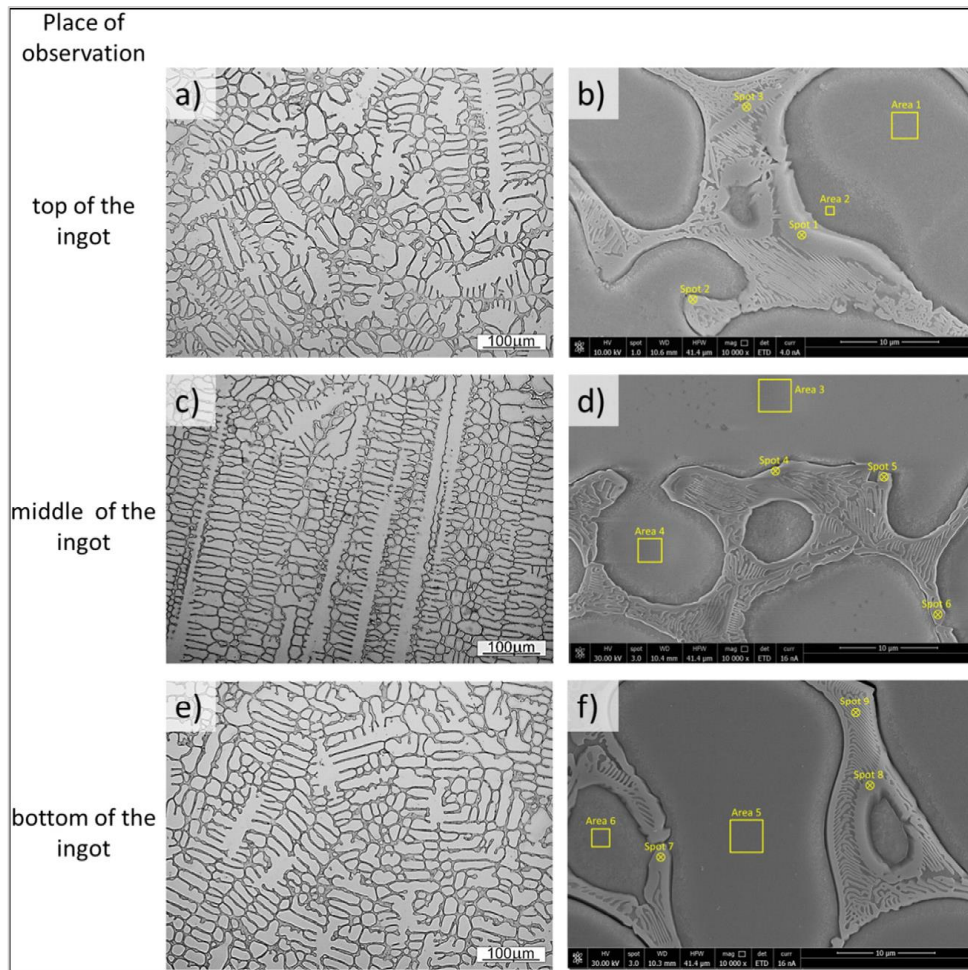


Figure 16: Microstructure in an as-cast Fe-25Cr-5Mo-0.82C alloys [34]

A typical microstructure in laser cladding coating of SS316L presents clusters of cells of different sizes, randomly dispersed microvoids and the presence of dark spots of inclusions (Figure 17) [35].

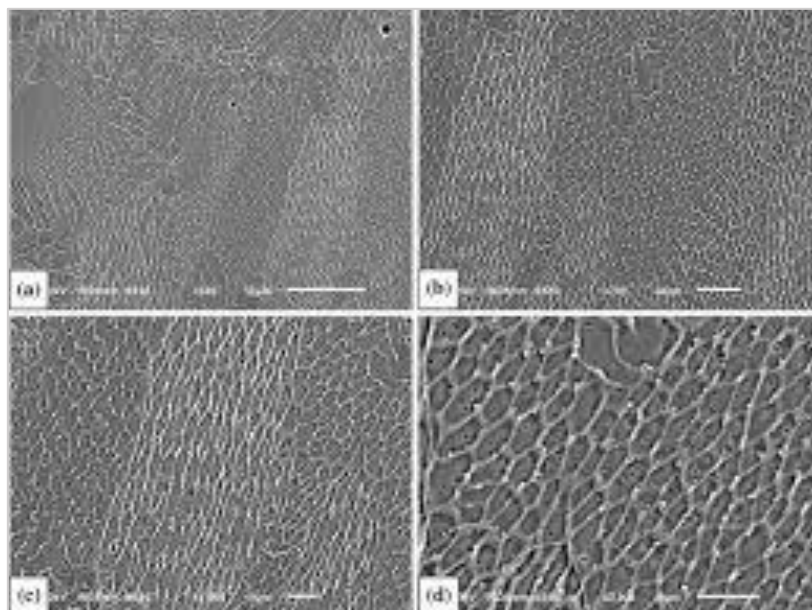


Figure 17: Microstructure in laser cladding coating of SS316L [35]

2.3.1.1 Effect of addition of carbide-forming element

The Fe – Cr – C – Mo system allows the formation of carbides such as $M_{23}C_6$, M_7C_3 , M_3C_2 , M_6C , MC, each promote by some specific elements. M_7C_3 carbides are important in the wear resistance of a material. The initial growth morphology, the crystallographic structure of the M_7C_3 are investigated by Sha Liu et al in conventional manufacturing processes [36]. This carbide is not a single block but a combination of multiple parts (Figure 18). In the solidification process of the molten alloy, the primary M_7C_3 carbide precipitates at high temperature. Among the initially growing M_7C_3 carbides, some may form the carbide shell by revolving growth direction. The constantly growing and revolving protrusion may enclose some small carbides within the carbide shell. Lateral step exists on the lateral plane. Ultimately, bulky M_7C_3 carbide is formed. Furthermore, the growth of the protrusions can also cause the coalescence of adjacent M_7C_3 carbides. The primary M_7C_3 carbide is rich in C and Cr, but poor in Fe atoms. In the coalescence process the C and Cr atoms in the gaps are continuously consumed, which decreases the diffusions of C and Cr atoms towards the M_7C_3 /liquid interface. It causes the gap filling process to remain incomplete. Moreover, with the continuous absorption of the mobile atoms, when their concentrations are reduced to a certain degree, the coalescence process of the M_7C_3 is terminated. Therefore, there are always several holes in the centre and gaps on the edge of the primary M_7C_3 .

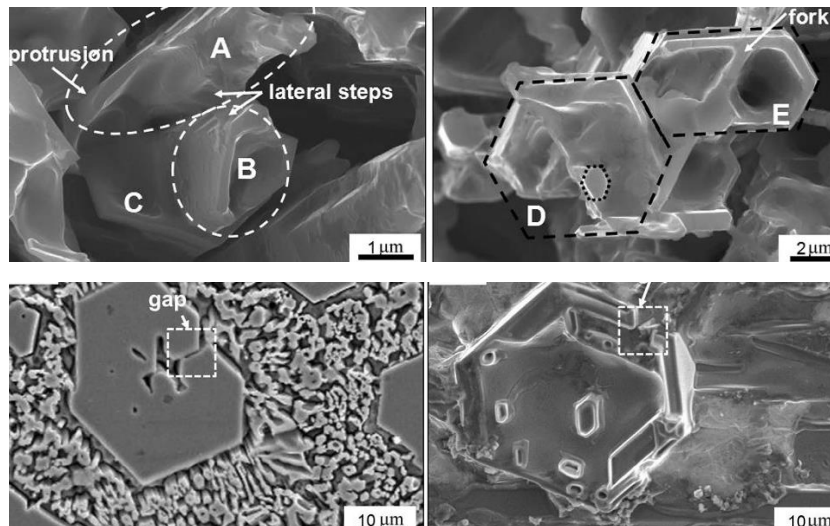


Figure 18: M_7C_3 carbide [36]

Eutectic carbides such as M_2C , M_6C , MC are the results of eutectic reactions between C and carbide former elements present in the interdendritic liquid [37]. M_6C is promoted by W and Mo. The 3D morphology of eutectic M_6C is characterised by the presence of a central platelet of M_6C carbide, from which secondary platelet of M_6C may arise separated from each other by austenite. These secondary platelets are usually thicker at the end, interrupting the continuity of the austenite and

forming a wall of carbide around eutectic colony. The morphology of this carbide is not influenced by the chemical composition or cooling rate, except that at faster cooling rates the distance between platelets decrease. The M_6C carbide has a complex FCC crystalline structure (Figure 19) [37].

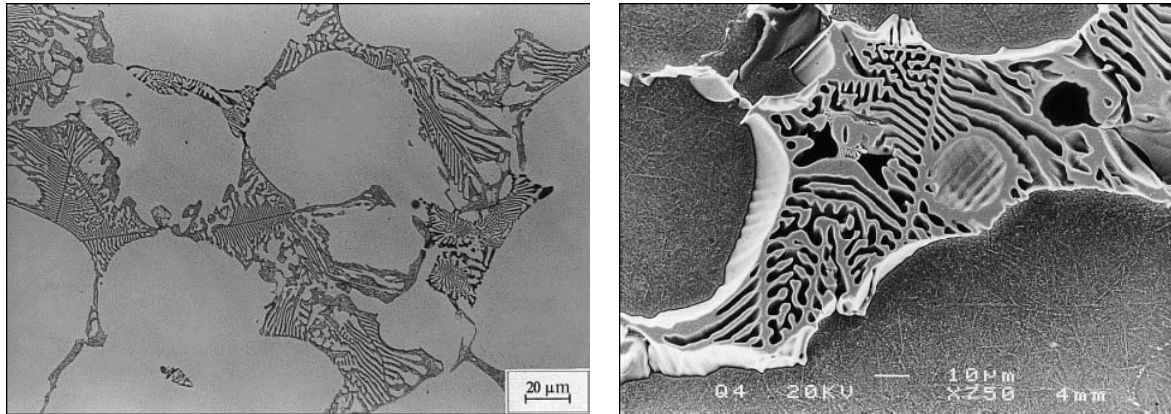


Figure 19: M_6C eutectic carbide [37]

M_2C is promoted by Mo, V and W. There are two type of M_2C eutectic morphology (Figure 20): irregular and complex regular. Irregular M_2C is characterised by a ragged boundary that does not clearly outline the interface between the matrix and the eutectic pool. The morphology is platelike with a tendency to assemble as radiating clusters. It is promoted by low cooling rates. Complex regular M_2C is characterized by a smooth boundary that clearly outlines the interface between the matrix and the eutectic pool. It shows a regular distribution of M_2C carbide over a small area forming cells with macrofacets. M_2C carbide has a hexagonal crystalline structure [37].

Eutectic morphology		
Optical	SEM	
		IRREGULAR
		COMPLEX REGULAR

Figure 20: M_2C eutectic carbide [37]

High melting temperature elements such as V, Nb, Ti and Ta tends to associate with carbon as MC carbide, in primary or eutectic condition. Figure 21 shows the different morphologies of MC carbide: divorced with isolated crystal, irregular with a petallike morphology and complex regular with a branched petallike morphology. MC carbide has a FCC structure [37].

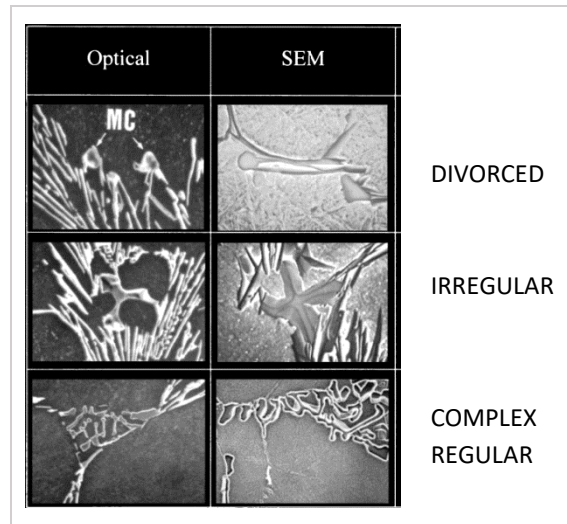


Figure 21: MC eutectic carbide [37]

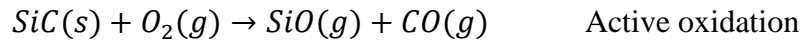
2.3.2 Silicon Carbide (SiC)

Silicon carbide is an interesting material that has found application in a variety of industries. It exhibits highest corrosion resistance of all advanced ceramics, a high hardness, high strength up to high temperature and a good thermal shock resistance. On the other hand, it present limitations such as high cost, brittleness, low toughness. It is characterized by many crystal types of microstructure, depending on the formation method. The most common are cubic, hexagonal and rhombohedral structures. [38].

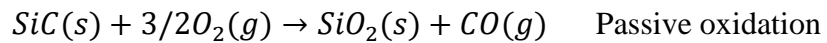
It is widely recognised that SiC ceramic has a high potential for advanced structural applications, as well as for the production of composite materials and electronic devices. In most of these usages, SiC parts or fibres (particles, whiskers, etc.) are in direct contact with metal parts or matrices. The properties and performance of such ceramic/metal systems are either controlled or strongly influenced by the microstructure and properties of SiC/metal interfaces.

When SiC particles are mixed with a stainless steel, there is a high risk of oxidation during the heating stage of the sintering or other manufacturing processes, when the temperature is still too

low to promote reduction of the most stable oxides. As is reported in the study of T. Narushima et al. [39] the oxidation of SiC powders can be divided into two types: active and passive oxidation, described as follows.



It results in the weight lost of the SiC particles.



It results in the weight gain of the SiC ceramics because of generating the oxide membrane on the SiC surface. Because the decomposition of SiC is very limited during sintering, less Si or C atoms are generated, and dissolved into the matrix. The oxidation of SiC is not useful to improve the thermal stability of the SiC/Fe interface.

3 EXPERIMENTAL METHODS

3.1 Original Powders

In the deposit fabrication through the laser cladding machine the particles must have specific characteristics. The powders size should be around 40-200 μm , otherwise they could create clusters and agglomerates on one side or cause great local pressures on the pipes on the other side. Spherical shape is preferred to an irregular shape since sharp edges could damage and/or clog pipes in the equipment. Moreover, irregular shape decreases the powder flowability leading to irregular powder feeding during the cladding process.

In this study, two different type of powders were considered: 316L Stainless Steel (SS316L) powder and silicon carbide (SiC) powder. Granulometry and X-Ray Diffraction on them were done at the Faculty of Science of ULiège [40].

3.1.1 316L Stainless Steel (SS316L)

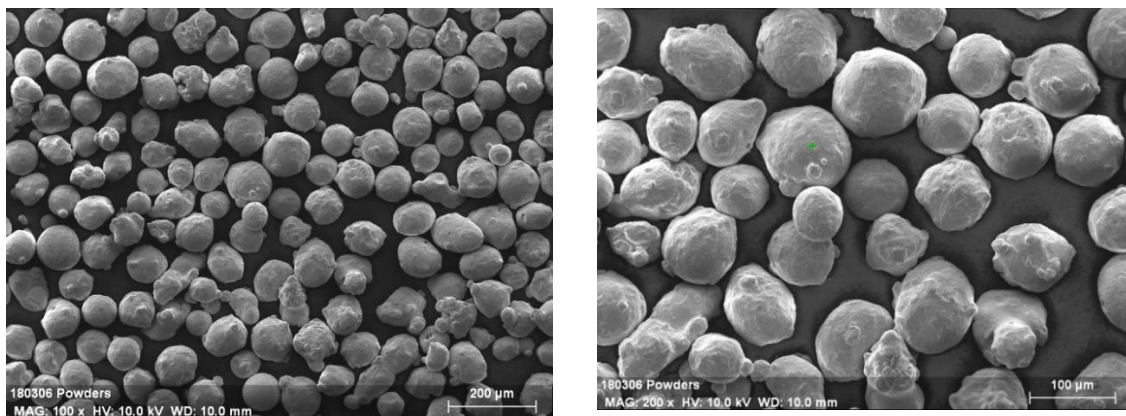


Figure 22: SS316L powder

Globular-spherical SS316L powders were provided by ‘Höganäs’ [41], a Swedish company. In Table 1 chemical composition of the powders is shown:

<i>Element</i>	C	Fe	Mo	Ni	Cr	Mn	Si
<i>%wt</i>	<0.03	Bal.	2.0-3.0	10.0-14.0	16.0-18.0	1.0-2.0	<1.0

Table 1: Chemical composition of the SS316L powder (Annex 1)

3.1.2 Silicon Carbide (SiC)

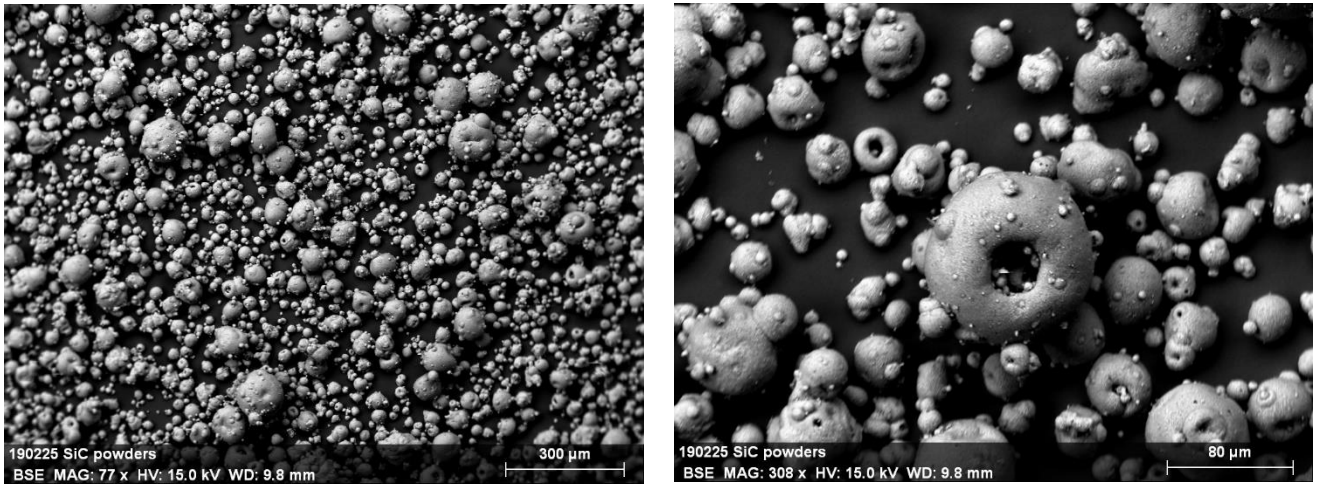


Figure 23: SiC powders at different magnification

SiC powders were provided by ‘H.C. Starck Ceramics GmbH’ [42], a German company. In Table 2 the chemical composition of the powders is given as follows:

<i>Element</i>	C	Fe	B	O	Al	Ca	Si
<i>%wt</i>	31-33	max 0.2	0.3-0.5	max 5	max 0.04	max 0.01	Bal.

Table 2: Chemical composition of the SiC powder (Annex 2)

The general morphology of these SiC powders is spherical, but many cavities and satellites are observed (Figure 23). SiC spherical powders are difficult to find in the market since generally they have irregular shape.

3.2 Milled Powders

Powder milling was done in order to optimize the deposit of SS316L + 20%SiC. The several problems of this composite will be shown in chapter 4.2.2. Two different milling approaches were done, on the manual mixture of SS316L and 20% SiC powders and on SiC powders alone.

The aim of this process is to break and deform the SiC particles, in order to eliminate their internal porosities. The limit of the treatment is the loss of the globular-spherical morphology from the excessive milling, since it could create particles with sharp edges and then problems during laser cladding process.

The device used for this pre-treatment was ‘Pulverisette 6’ [43]. The equipment is composed by a double turning system in which a bowl is located. During the milling, powders and balls are placed into the bowl. The internal part of the bowl and the used balls are tungsten carbide (WC), as shown in Figure 24.



Figure 24: Milling equipment [43]

This device allows to set up the bowl rotational speed, the milling time, the break time and the number of repetitions.

For each milling procedure, the process was stopped after a specific time and a small amount of powders was collected and put on a disc with adhesive paper (Figure 25) in order to check the effect of the milling process with SEM. Microscopy observations, chemical analyses and DTA tests were done on milled powders as is explained in chapter 4.1.



Figure 25: Example of powders on a disc

3.2.1 SS316L + 20% SiC

The set-up of the device for the manual mix of SS316L powders + 20% SiC powders is shown in the Table 3. The device was stopped after different milling time (Table 4).

Powders to mill	316L+20%SiC
Powders weight	450 g
Balls number	12
Ball to powder ratio	1 : 5
Rotational speed	180 rpm
Break time	10 min / 30min

Table 3: Milling parameters for SS316L+20%SiC

STAGE N°	MILLING TIME
Stage 1	30 min
Stage 2	1 h
Stage 3	2 h
Stage 4	4 h
Stage 5	6 h

Table 4: Milling stage for SS316L+20%SiC

3.2.2 SiC

Three different milling strategies (Table 5, Table 6, Table 7) were realized on the SiC powders in order to have the same modification occurring in the milling of the manual mix but keeping the two powders separate.

Powders to mill	SiC
Powders weight	100 g
Balls number	13
Ball to powder ratio	1 : 1
Milling time	20 min, 1 h
Rotational speed	150 rpm
Break time	10 min / 30min

Table 5: Milling parameters 1 for SiC

Powders to mill	SiC
Powders weight	200 g
Balls number	5
Ball to powder ratio	1 : 5
Milling time	30 min, 1 h
Rotational speed	150 rpm
Break time	10 min / 30min

Table 6: Milling parameters 2 for SiC

Powders to mill	SiC
Powders weight	200 g
Balls number	8
Ball to powder ratio	1 : 3
Milling time	30 min, 1 h
Rotational speed	150 rpm
Break time	10 min / 30min

Table 7: Milling parameters 3 for SiC

3.3 Deposit fabrication

The samples were fabricated by Sirris [44] with a DUOCLAD VI LF 2000 as shown in Figure 26. This machine is developed by BeAM and it uses the CLAD (Direct Laser Additive Construction) process developed by IREPA LASER [45].



Figure 26: DUOCLAD VI LF 2000 [24]

In this section is reported the main characteristic of the functioning of this machine.

Powders are inserted on the top of a powder feed. The machine is equipped with a double powder feed, in particular MediCoat DUO (Figure 27a) [46]. In this case, it is possible to work with different powders depending on the deposit composition.

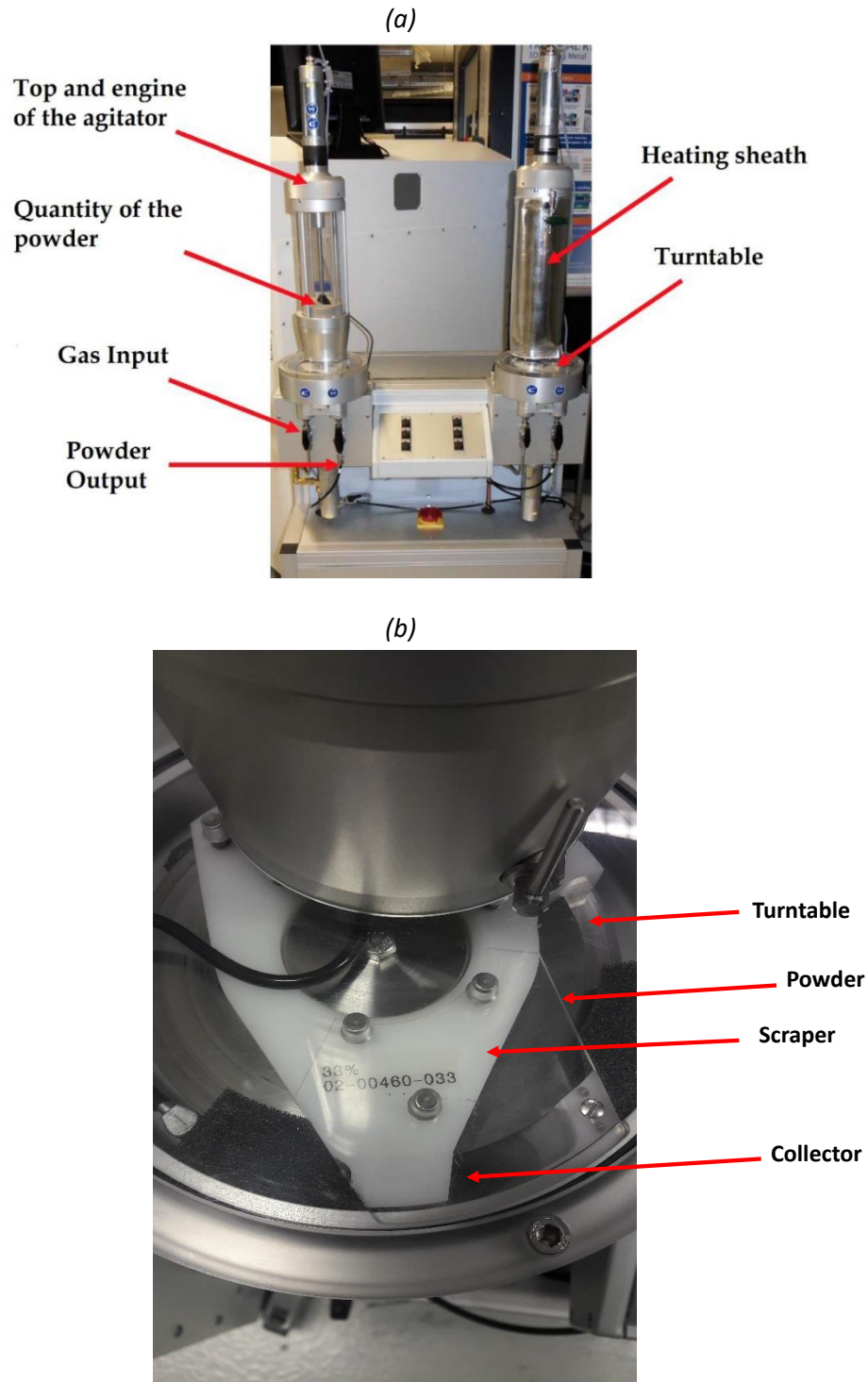


Figure 27: (a) Feeding towers [24], (b) Turntable

During cladding, the turntable (Figure 27b) of the tower turns at different speeds depending on the powder natures and the requested powder feedings. The powder is mechanically mixed by an agitator and it is placed below the tower, on the turntable. The scraper and the collector homogenise the powder stream on the turntable before falling in the pipe. In this phase, the powder is also mixed with argon that bring the powder until the nozzle. The quantity of argon [min^{-1}] depends again on the nature of the powders.

The nozzle is an important part of the machine because it conveys the laser, the gas and the powders.

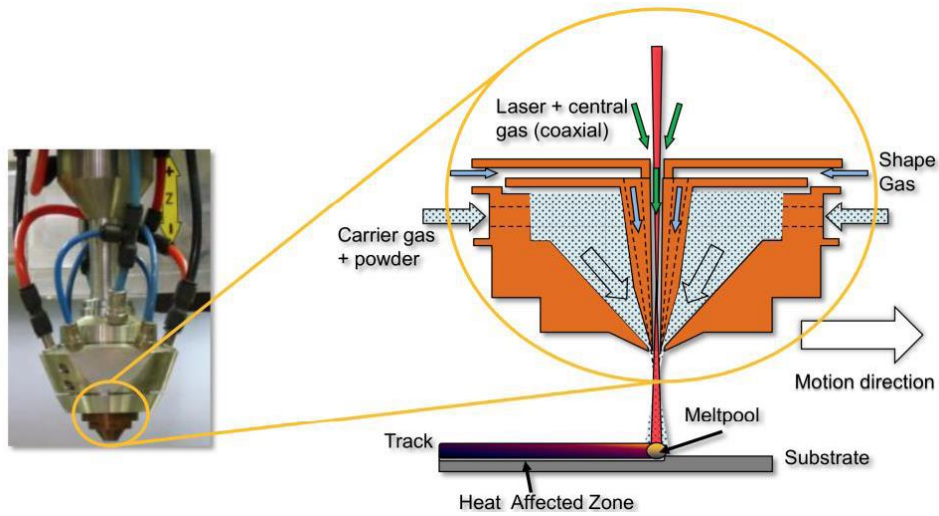


Figure 28: Coaxial nozzle by IREPA [24]

A coaxial nozzle (Figure 28) developed by IREPA [45] was used to produce the samples. The nozzle is placed coaxially to the laser beam. It has different inputs: the laser enters through the top with a central gas inlet to protect the laser from rising fumes, the powder enters on the left, coming with a carrier gas from the feeding tower, the shape gas enters on the right, that is responsible for shaping the powder cone.

The schematic process is shown in Figure 29. Different set up are possible: the laser beam starts from the left and it moves on the right. When it passes to the next layer it can continue over the last track or it can move over the first track.

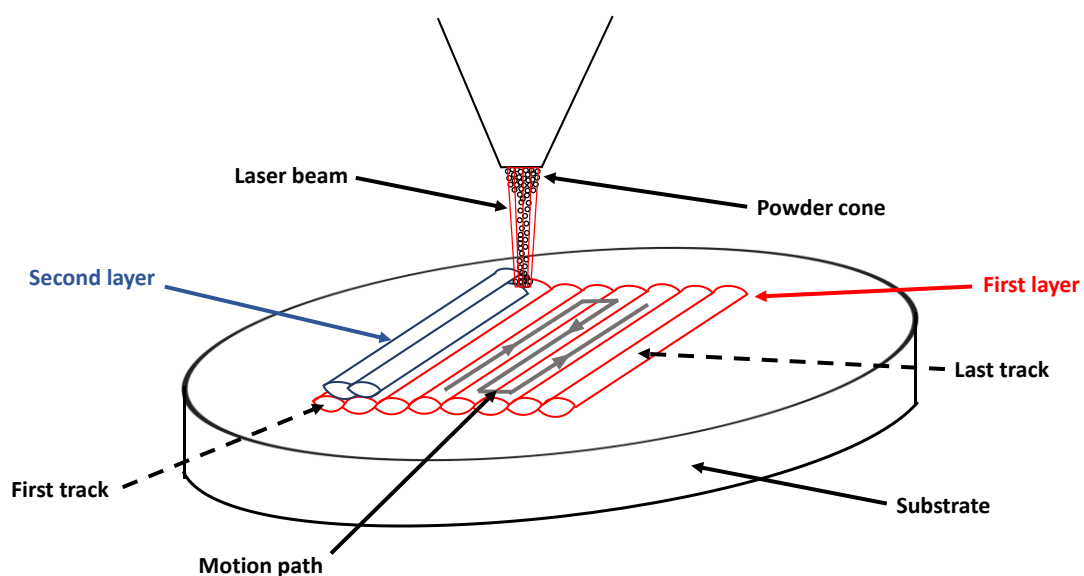


Figure 29: Laser cladding schematic process

In this study the four cladded deposits are analysed. One has 10% SiC in volume and three have 20% SiC in volume. The codification of the name and the deposits analysed are shown in Figure 30.

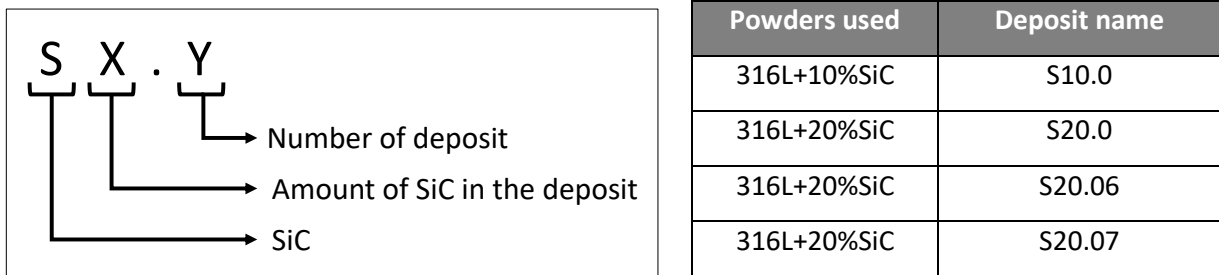


Figure 30: Deposit analysed in this study

Different parameters were used (Figure 31). Two different powers and relative scanning speed were given to the machine. The laser worked with the lower power-scanning speed couple during the curve of the changing track of the deposit, while during the linear deposition of the laser cladding the higher power-scanning speed couple was used. The lines visible in the Figure 31 correspond to the different couple power-scanning speed, while the points indicate the incident energy that is the ratio between the higher value of power and scanning speed.

For the fabrication of the deposit of 316L + 10% SiC, two different types of parameters were tried: one set up is present in literature (point and line green in Figure 31) [29], the other is from the fabrication of the cladded deposit of 316L + WC (point and line blue in Figure 31) [47]. Both the cladded deposit with the two different set-up present good surface quality, without visible porosity and/or external cracks. It was preferred the set-up present in literature since it is faster.

For the first production of the cladded deposit of 316L + 20% SiC (sample S20.0) the same parameters of the sample S10.0 present in literature were used. In order to achieve better result, both the scanning speed and the power were decreased. This set up was used in the sample S20.06. In particular, the purpose was to increase the incident energy. Finally, for the sample S20.07 was used a set up with a higher scanning speed, but with low power. In this case, the incident energy was kept at around 90 J/mm according to the literature. Moreover, the first two layers of the deposit were done with only SS316L with the parameters of the 316L+WC composite.

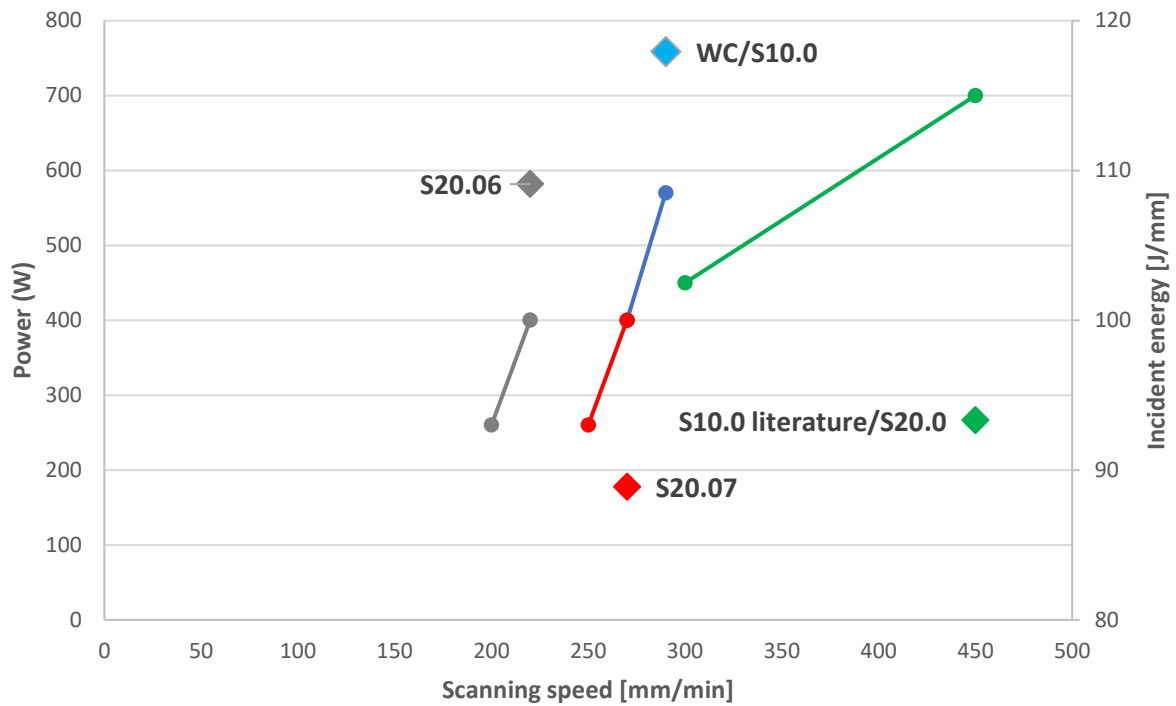


Figure 31: Laser cladding parameters

3.3.1 SS316L + 10% SiC

The main parameters for the set-up of the laser cladding machine are shown in Table 8.

Sample	Scanning Speed [mm/min]	Power [W]	Incident Energy [J/mm]
S10.0 [29]	300 - 450	450 - 700	93

Table 8: Parameters for cladded deposit of SS316L+10%SiC

The deposit after the fabrication is shown in Figure 32. It appears regular and without external defects.

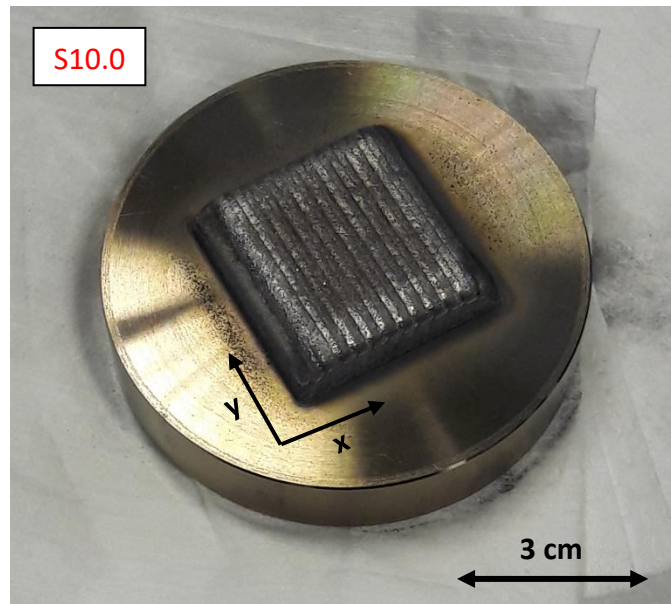


Figure 32: Deposit S10.0

The geometric characteristics are shown in Table 9.

Sample	Height	X [mm]	Y [mm]
S10.0	10	37	38

Table 9: Geometric characteristic of S10.0

3.3.2 SS316L + 20% SiC

The main parameters for the set-up of the laser cladding machine are shown in Table 10.

Sample	Scanning Speed [mm/min]	Power [W]	Incident Energy [J/mm]
S20.0 [47]	300-450	450-700	93
S20.06	200-220	260-400	109
S20.07	250-270	260-400	89

Table 10: Parameters for cladded deposit of SS316L+20%SiC

The deposit after the fabrication and the relatives geometric characteristics are shown in Figure 33 and in Table 11. The tracks of all the deposits are well visible and the external look is naturally with a shiny metallic colour without any cleaning. Nevertheless, the S20.0 and especially S20.06 exhibit cracks at the deposit-substrate interface. Instead, the S20.07 is more regular than the other deposits and it does not present cracks.

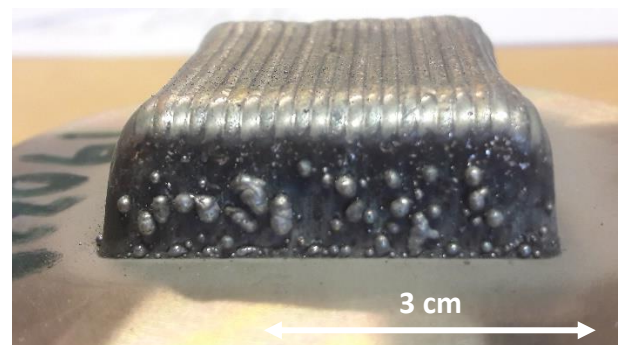
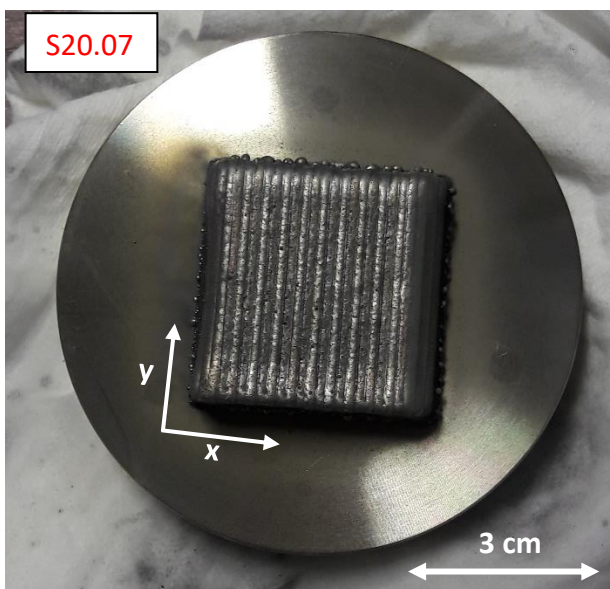
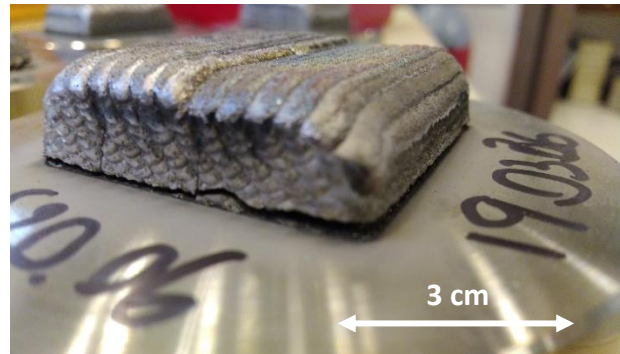
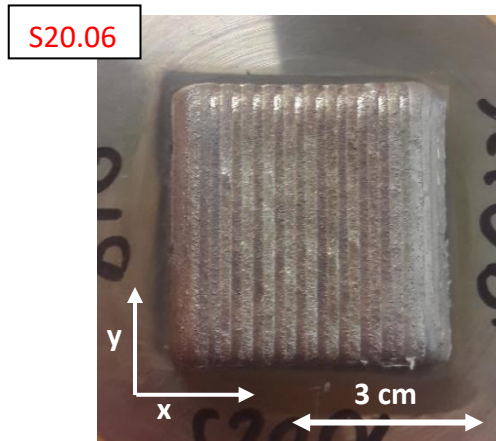
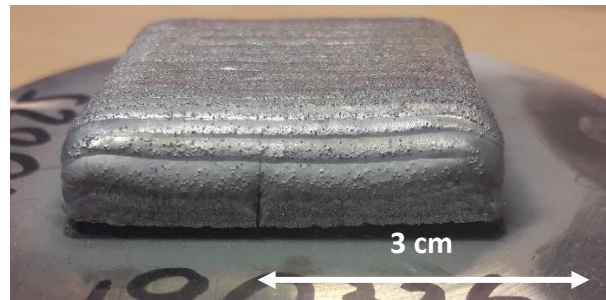
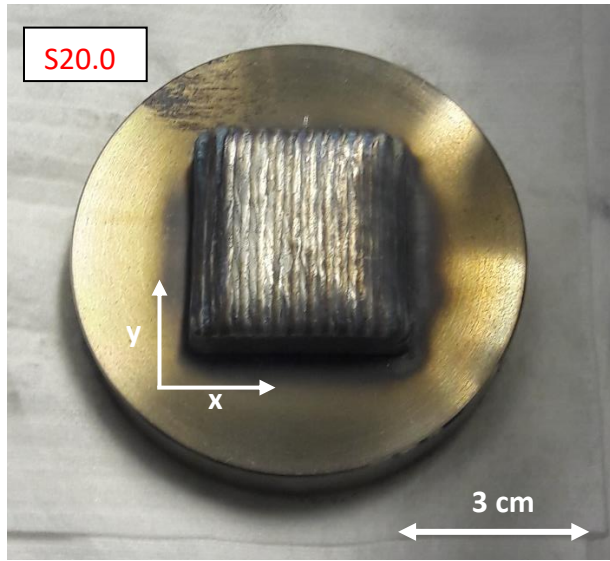


Figure 33: Deposits S20.0, S20.06, S20.07

Sample	Height [mm]	X [mm]	Y [mm]
S20.0	13	38	40
S20.06	13	38	38
S20.07	13	38	38

Table 11: Geometric characteristic of S20.0, S20.06, S20.07

Both the feeding towers were utilized in order to produce S20.0 and S20.06, respectively with the original SS316L powders in the first tower and original SiC powders in the second one. During the fabrication of these samples many big sparks were observed, with a high light intensity. The laser beam in contact with powders had a high light intensity as well. In addition, gas around the deposit and in the chamber was observed.

Principally one feeding tower was utilized to produce sample S20.07, using milled SS316L + 20% SiC powders, and secondarily original SS316L powders in the other tower. This deposit is characterized by the first two layers of original SS316L and the rest of the layers by milled SS316L + 20% SiC powders. This was a preliminary choice in order to avoid the presence of cracks as in the previous samples.

3.4 Microstructural characterization

In order to characterize the deposits were done different workings on them in order to have an internal section to analyse. The two devices utilized for the microstructure observations are Optical Microscope (OM) and Scanning Electron Microscope (SEM).

3.4.1 Samples preparation

The deposits were cut by Spark Erosion Machine to obtain cylinder samples for thermal analyses or different sections for the microstructural characterization. In addition, was utilized a precision Cut-Off Machine to the normal cutting of metal.

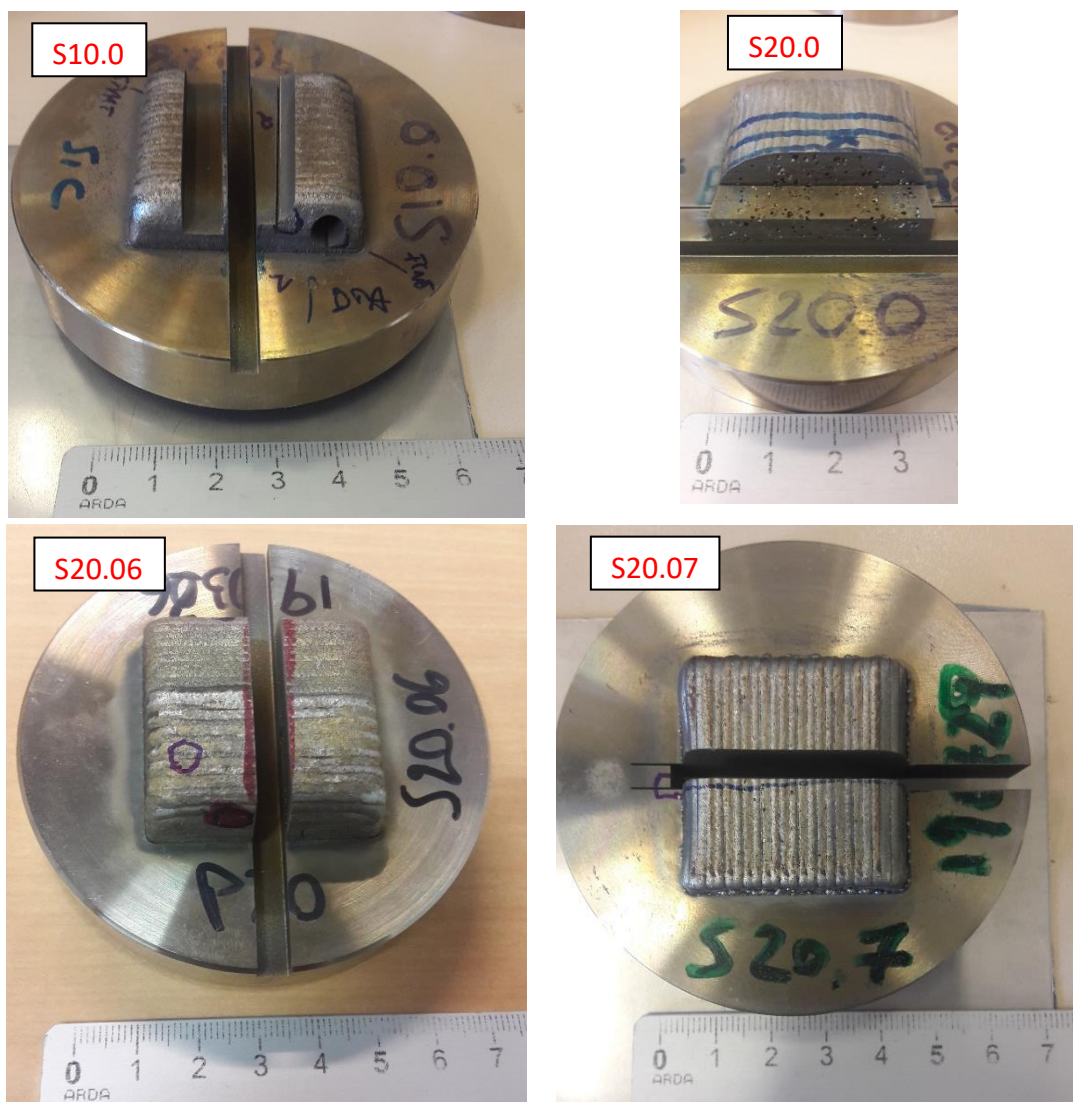


Figure 34: Cut deposits

Some particular pieces were obtained on the deposit S10.0 for DTA tests (Figure 35 and Figure 36).

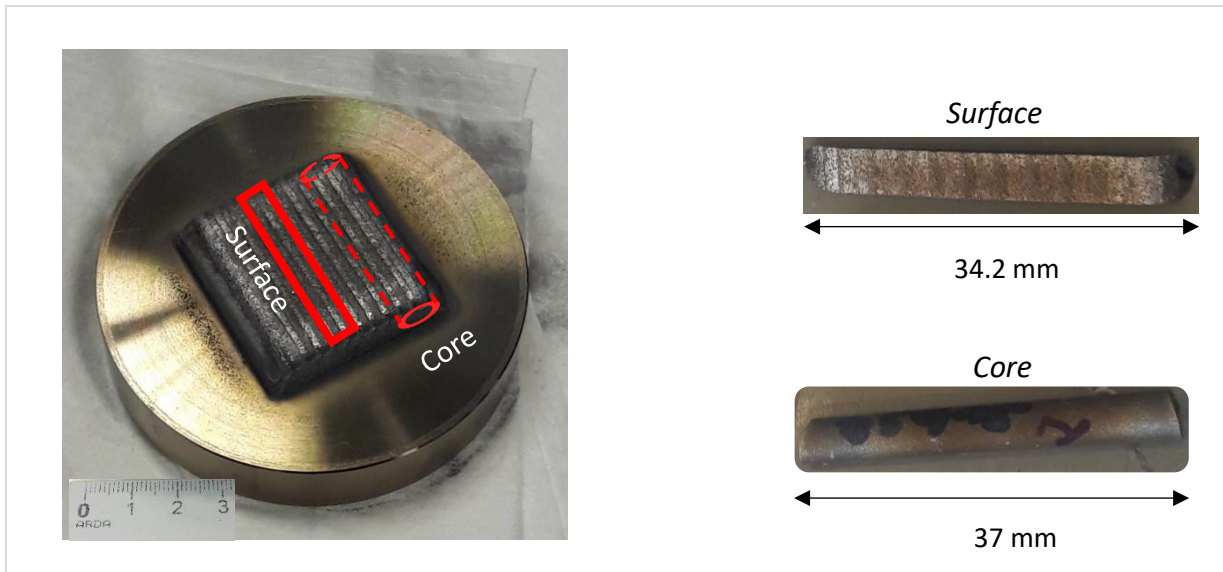


Figure 35: Samples for DTA tests

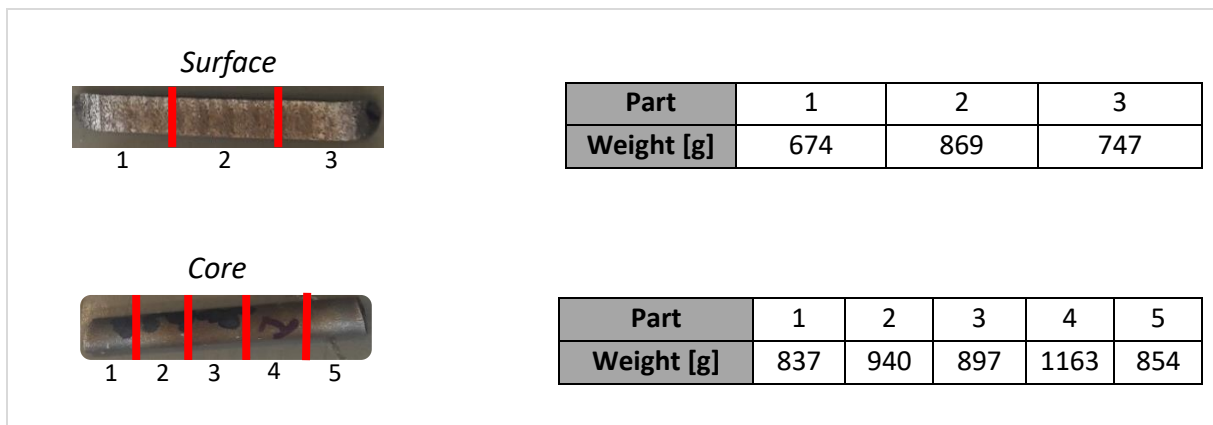


Figure 36: Characteristic of samples for DTA tests

The cut sections were prepared with different techniques. First, they were incorporate in Bakelite using a STRUERS Citopress-1 (Figure 37a) [48]. Afterwards, polishing steps were done with the STRUERS Tegramin-30 [48] to arrive to a mirror polished surface. In order to observe the differences among the microstructure's phases, an etching of diluted aqua regia was applied on the samples as well. The last step to the sample preparation was a treatment with an Oxide Polishing Suspension (OPS), composed of colloidal silica (Figure 37b).

STRUERS Citopress-1



STRUERS Tegramin-30



Figure 37: STRUERS equipment [48]

In Figure 38 are visible the samples after all the steps of the preparation.

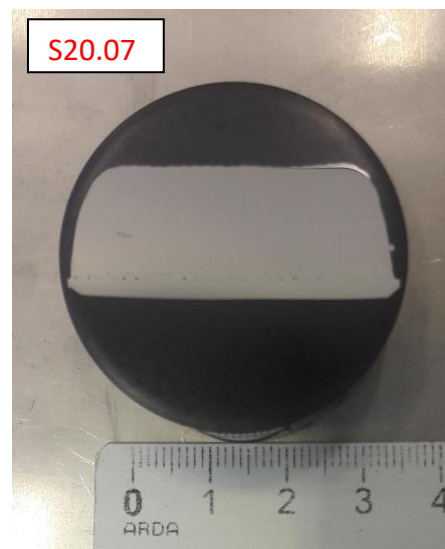
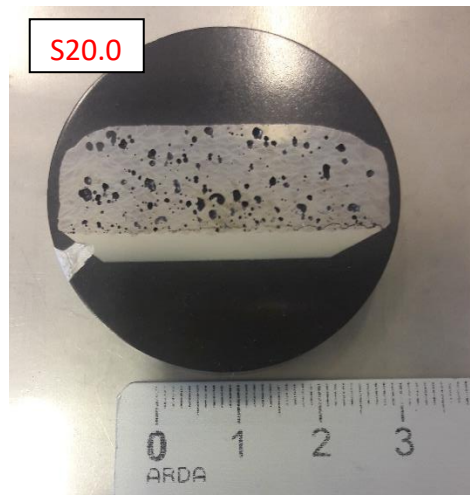
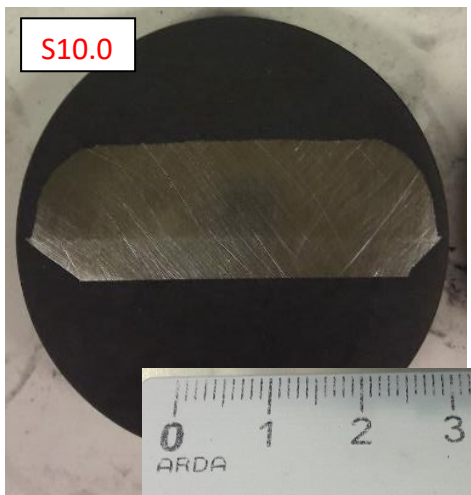


Figure 38: Samples after preparation

3.4.2 Optical Microscope (OM) and Stream Analyse Software

OM analyses were performed with an Olympus BX60 Microscope (Figure 39) [49]. Analyses were done at magnifications of 2.5x, 5x, 10x and 20x.



Figure 39: Olympus BX60 [49]

The Stream Analyse Software [49] was utilized to analyse some pictures obtained from Optical Microscope. The software has many options as acquiring, processing, measuring images. In this study, the software was utilized to analyse the section of sample S20.0 to check the porosity.

3.4.3 Scanning Electron Microscope (SEM)

SEM analyses were done with a Phillips XL30 FEG-ESEM (Figure 40) [50]. It is equipped with an EDAX detector (Energy dispersive x-ray detector with an ultra thin window). The EDAX software allows to make point analysis, linescan and spectral mapping.



Figure 40: Phillips XL30 FEG-ESEM [50]

3.5 Differential Thermal Analysis (DTA)

The DTA tests were performed with a NETZCH STA 449C Jupiter DTA (Figure 41). This device can observe the mass changes, oxidation/reduction behaviour, decomposition and corrosion studies. It can operate under a high vacuum or under protective atmosphere [51].



Figure 41: NETZCH STA 449C Jupiter for DTA tests [51]

For this study, DTA was used to investigate the thermal behaviour of the powders and of cladded deposits.

The DTA tests on powders are listed in Table 12.

Powders	Heating Temperature [°C/min]	Range Temperature [°C]	Cooling Temperature [°C/min]
SS316L	5	0-1550	5
SS316L+10%SiC	5	0-1550	5
SS316L+20%SiC	5	0-1550	5
SS316L + 20% milled SiC 1:5 30 min	5	0-1550	5
SS316L + 20% milled SiC 1:3 1 h	5	0-1550	5
milled mix SS316L+20%SiC 1:5 1h	5	0-1550	5
milled mix 316L+20%SiC 1:5 2h	5	0-1550	5
milled mix 316L+20%SiC 1:5 4h	5	0-1550	5
milled mix 316L+20%SiC 1:5 6h	5	0-1550	5

Table 12: DTA tests on powder

The surface part and the cylinder of the deposit S10.0 of Figure 36 were used for different DTA tests (Table 13). The aim was to check the difference between the core of the deposit and the external part.

Deposit part	Heating Temperature [°C/min]	Range Temperature [°C]	Cooling Temperature [°C/min]
Substrate (316L)	5	0-1550	5
Surface 3	5	0-1550	5
Core 1	5	0-1550	5
Core 3	5	0-1550	5
Core 2	5	0-1240	20

Table 13: DTA tests on deposit

3.6 Hardness test

Hardness indentation was done on sample S10.0. The device utilized was the EMCO M1C 010 (Figure 42) [52]. This is considered a digital low-load hardness testing machine. It is possible to utilize Vickers, Brinell, Knoop and Rockwell testing with various weights. DIN EN ISO, ASTM E-92 HV 30 were used in this study. The hardness tester is equipped with an automatic tool for the exchange of lens and indenter, fully automatic test cycle, automatic lens focusing, leading-edge high-resolution CCD camera, fully automatic image evaluation and manual cross slide.

In this work the test was done manually. It is then possible to calculate the hardness value by measuring the distances between the rhombus edges with an appropriate software for the image analysis, ecos010/image.



Figure 42: EMCO M1C 010 [52]

4 RESULTS

4.1 Powders characterization

Powders characterization is useful in order to understand the particles behaviour. In every process the morphology, dimensions, physical and chemical properties of powders have influence on the final result. This section shows the result of the characterization on original powders SS316L, SiC, SS316L + 10% SiC, SS316L + 20% SiC and milled powders SS316L + 20% SiC, SiC.

4.1.1 Original powders

4.1.1.1 316L Stainless Steel powder

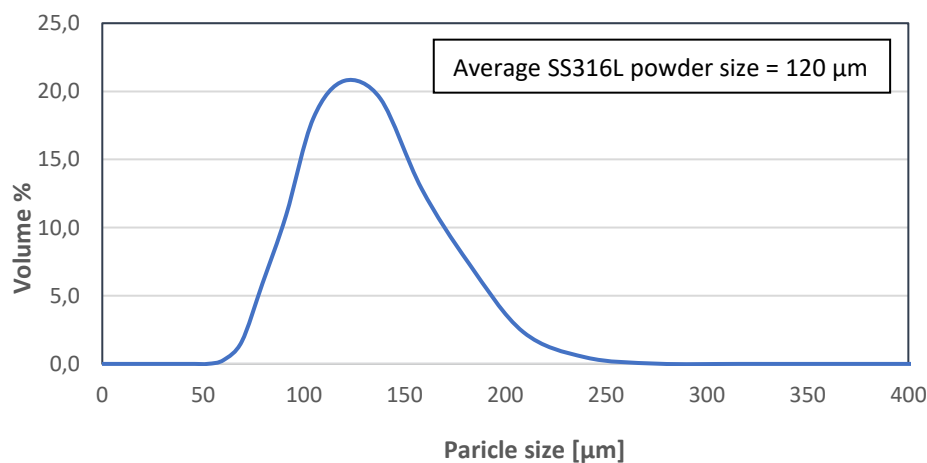


Figure 43: Particle size distribution of 316L powders

Figure 43 shows the amount of powders in volume % in function of the particle size of SS316L.

The size range is from 60 µm to 270 µm with an average value of 120 µm.

DTA heating and cooling curves relative to SS316L powder are shown in the next figures (Figure 44, Figure 45).

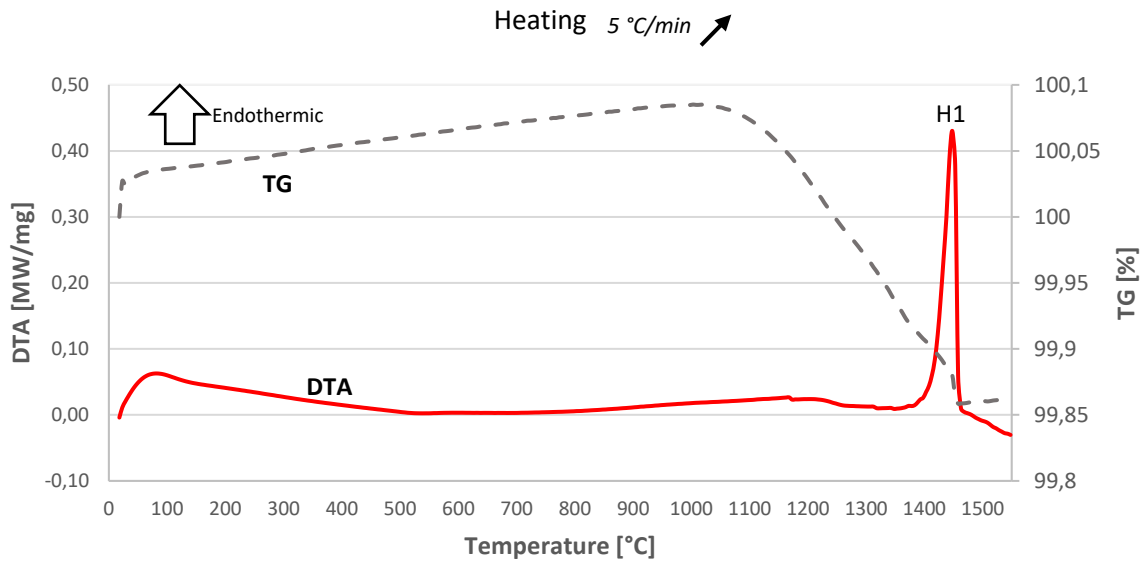


Figure 44: DTA and TG heating curve for SS316L powder

Peak	Start Temperature [°C]	Max/Min Temperature [°C]	End Temperature [°C]	Reaction or phase transformation
H1	1120	1136	1150	Austenite fusion

Table 14: Principal heating peaks for SS316L powder

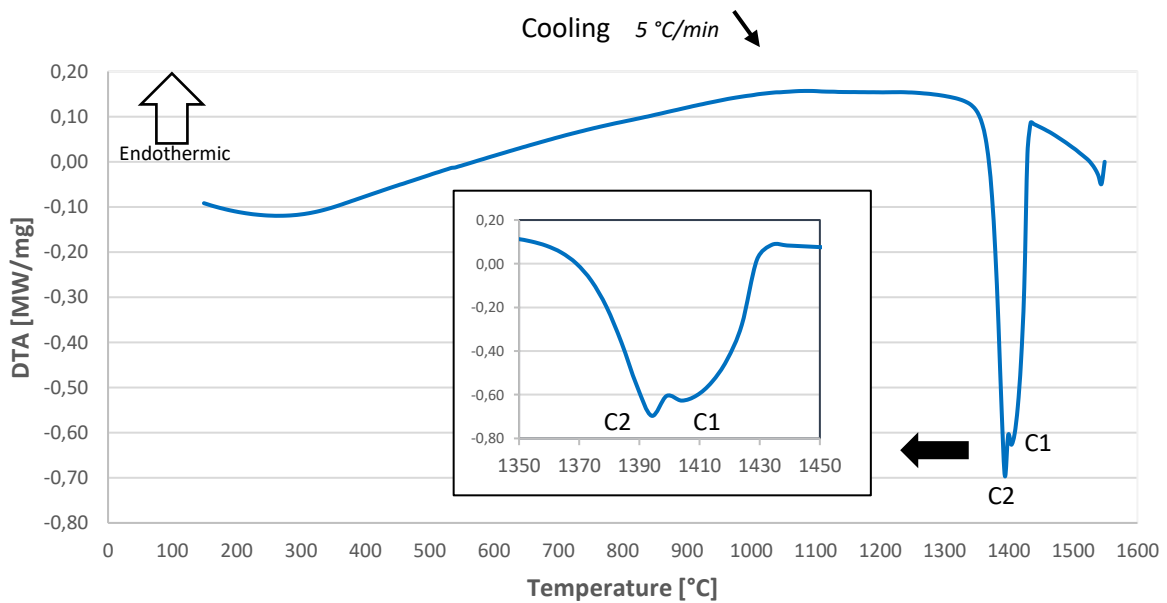


Figure 45: DTA cooling curve for SS316L powder

Peak	Start Temperature [°C]	Max/Min Temperature [°C]	End Temperature [°C]	Reaction or phase transformation
C1	1438	1404	1399	Austenite solidification
C2	1400	1394	1364	δ ferrite solidification

Table 15: Principal cooling peaks for SS316L powder

Optical microscope observations to solidify powders after DTA are illustrated in Figure 46.

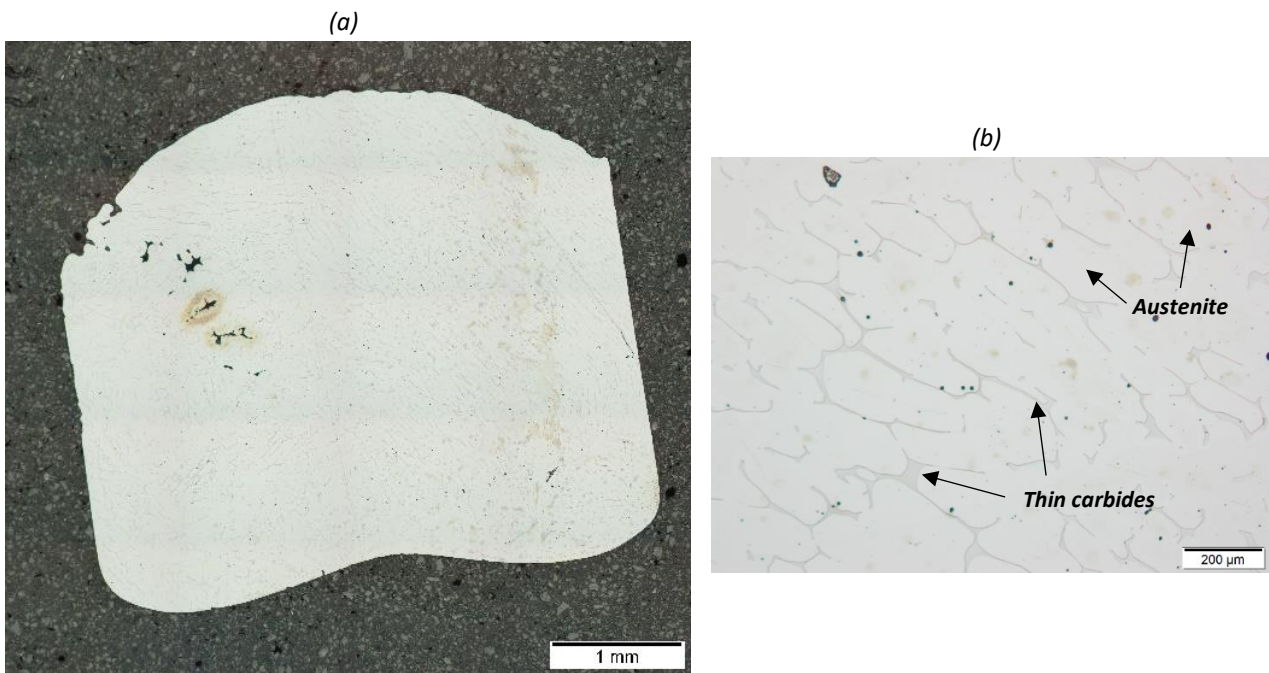


Figure 46: Optical Microscope observation on SS316L after DTA test

Powders after DTA are not completely compact, as is visible on the left zone of Figure 46a. Referring to a focus on the microstructure (Figure 46b), an austenitic matrix with several thin carbides is present.

4.1.1.2 Silicon Carbide powder

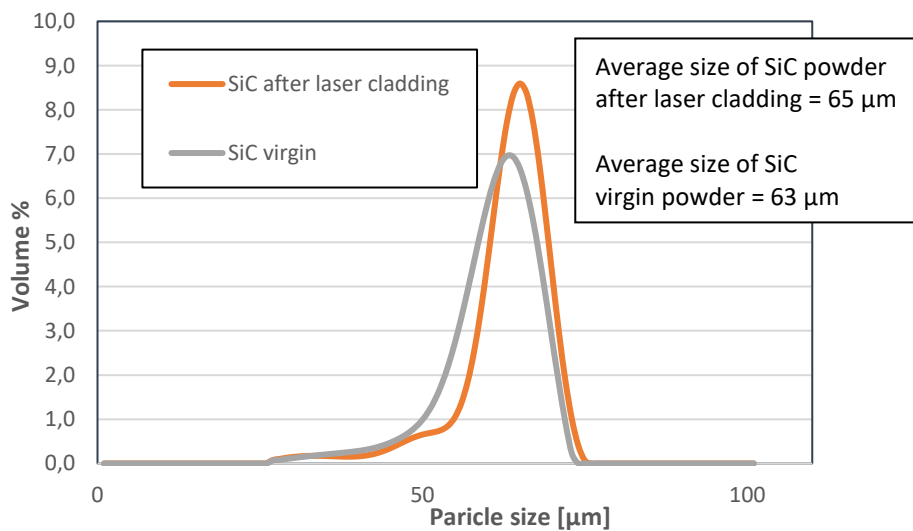


Figure 47: Particle size distribution of SiC powders

In Figure 47 the average particles distribution of SiC after laser cladding and SiC virgin are shown. SiC powder after laser cladding is referred to the powder take from the nozzle of laser cladding machine after the process, while SiC virgin is referred to the powder as product. The curve of SiC powder after laser cladding is shifted to the right with respect to the curve of SiC virgin powder, with an increase of the average dimension. This means that during laser cladding the smaller SiC powders dissolve in the atmosphere when they exit from the nozzle, and only the bigger particles reach the substrate.

4.1.1.3 SS316L + 10% SiC powder

DTA heating and cooling curves are visible in the next figures (Figure 48, Figure 49).

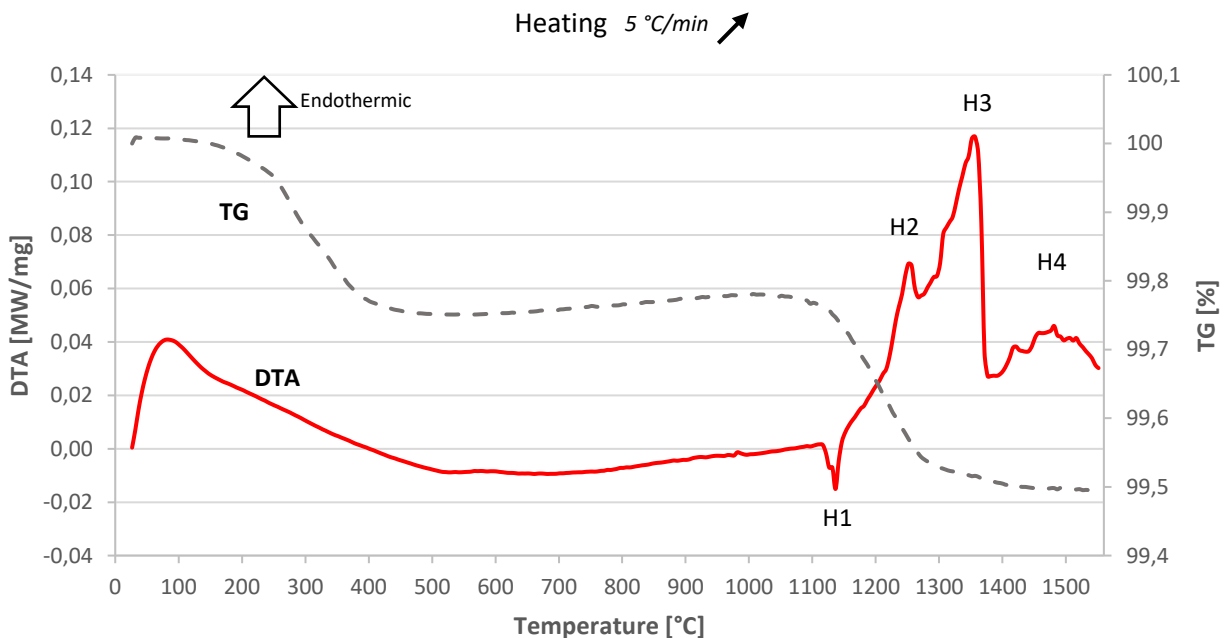


Figure 48: DTA and TG heating curve for SS316L+10%SiC powders

Peak	Start Temperature [°C]	Max/Min Temperature [°C]	End Temperature [°C]	Reaction or phase transformation
H1	1120	1136	1150	Oxidation
H2	1240	1256	1271	Austenite fusion
H3	1271	1356	1381	Austenite fusion
H4	1400	?	?	SiC fusion

Table 16: Principal heating peaks for SS316L+10%SiC powder

The presence of two austenite fusion peaks (H2, H3 in Figure 48) is due to inhomogeneous SS316L + 10% SiC powders in the crucible of the DTA device. There are some parts with more density of SS316L than other parts and this leads to the fusion of the austenite at different temperature.

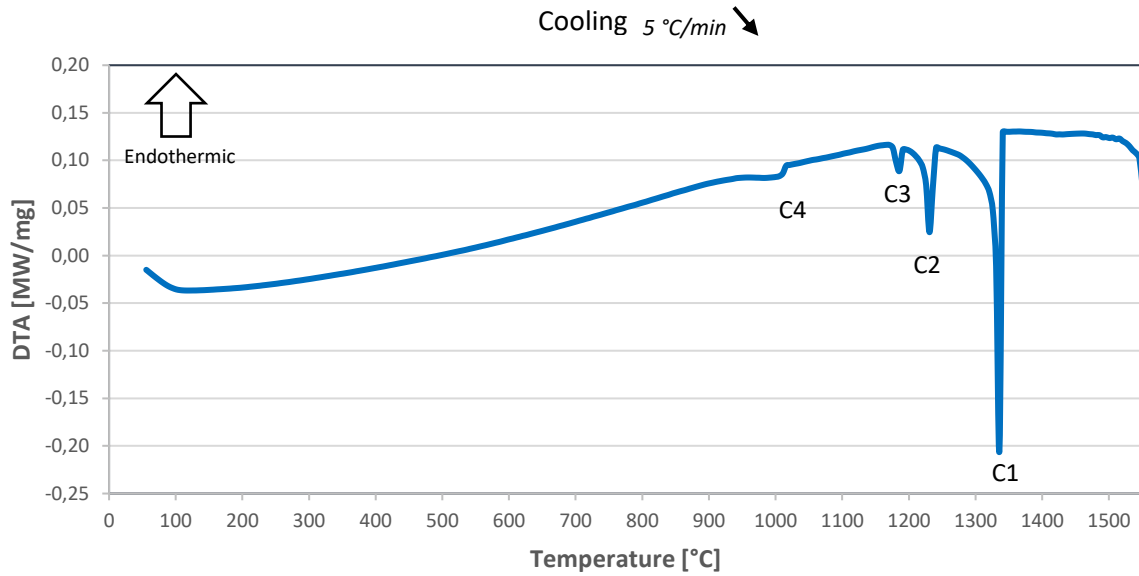


Figure 49: DTA cooling curve for SS316L+10%SiC powder

Peak	Start Temperature [°C]	Max/Min Temperature [°C]	End Temperature [°C]	Reaction or phase transformation
C1	1346	1336	1321	Austenite solidification
C2	1246	1231	1200	M ₇ C ₃ solidification
C3	1200	1186	1175	M ₂ C solidification
C4	1020	1005	945	Precipitation from peritectoid [47]

Table 17: Principal cooling peaks for 316L+10%SiC powder

OM observations to solidify powders are shown in Figure 50.

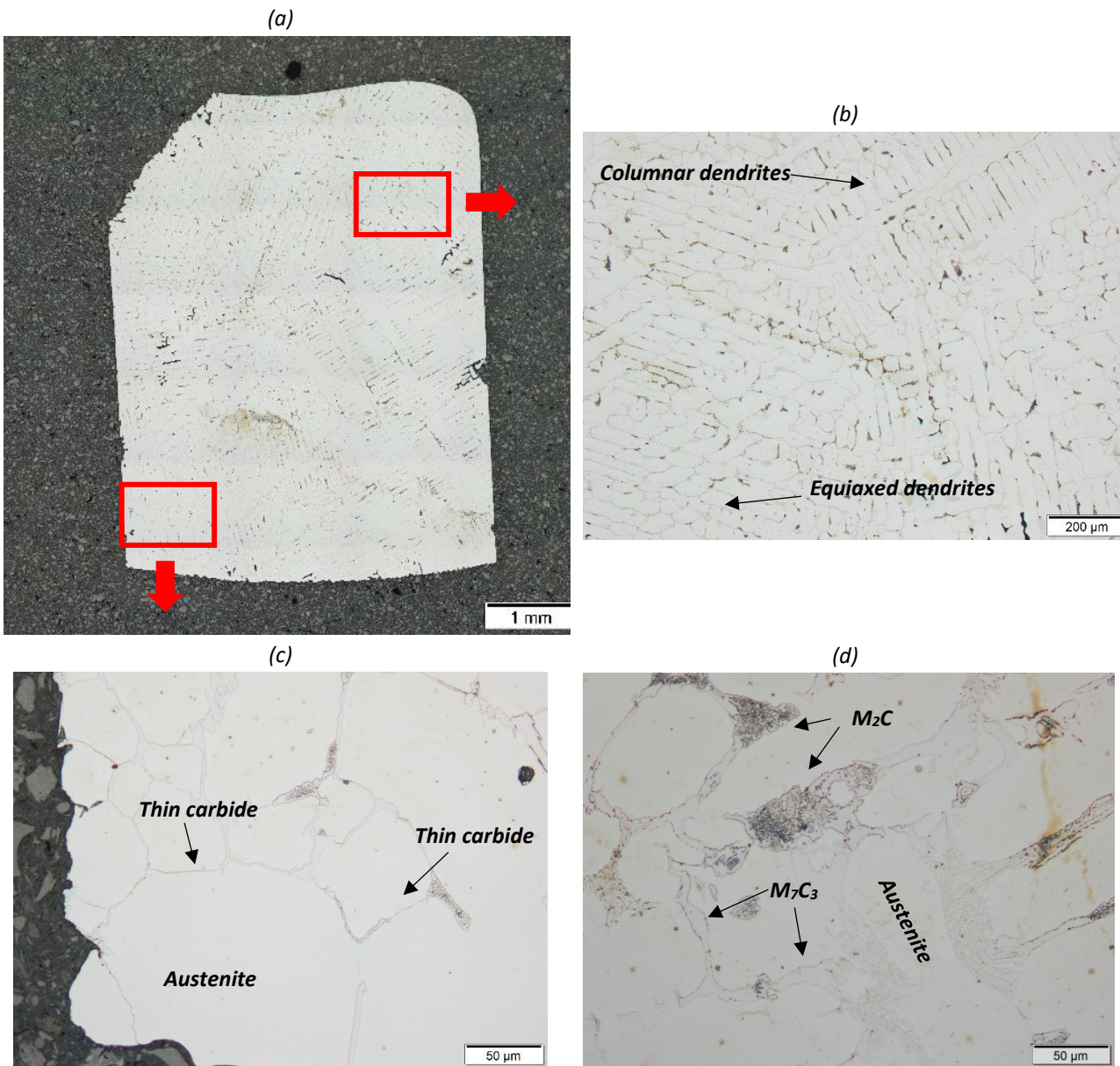


Figure 50: Optical microscope observation on SS316L+10%SiC powders after DTA tests

The solidification starts from the border where powders are in contact with the crucible, in fact it is possible to see the solidification direction of the microstructure. In particular in Figure 50b are evident columnar dendrites and equiaxed dendrites. In Figure 50c there is a focus of the bottom left corner of the overview (Figure 50a), where different carbides are present. In fact it can be noticed thin carbides, but also complex carbides, in particular M_2C and M_7C_3 , indicated on the focus in Figure 50d. M_7C_3 carbides are formed after the austenite, because their shape follows the austenite cell.

4.1.1.4 SS316L + 20% SiC powder

DTA heating and cooling curves are visible in the next figures (Figure 51, Figure 52).

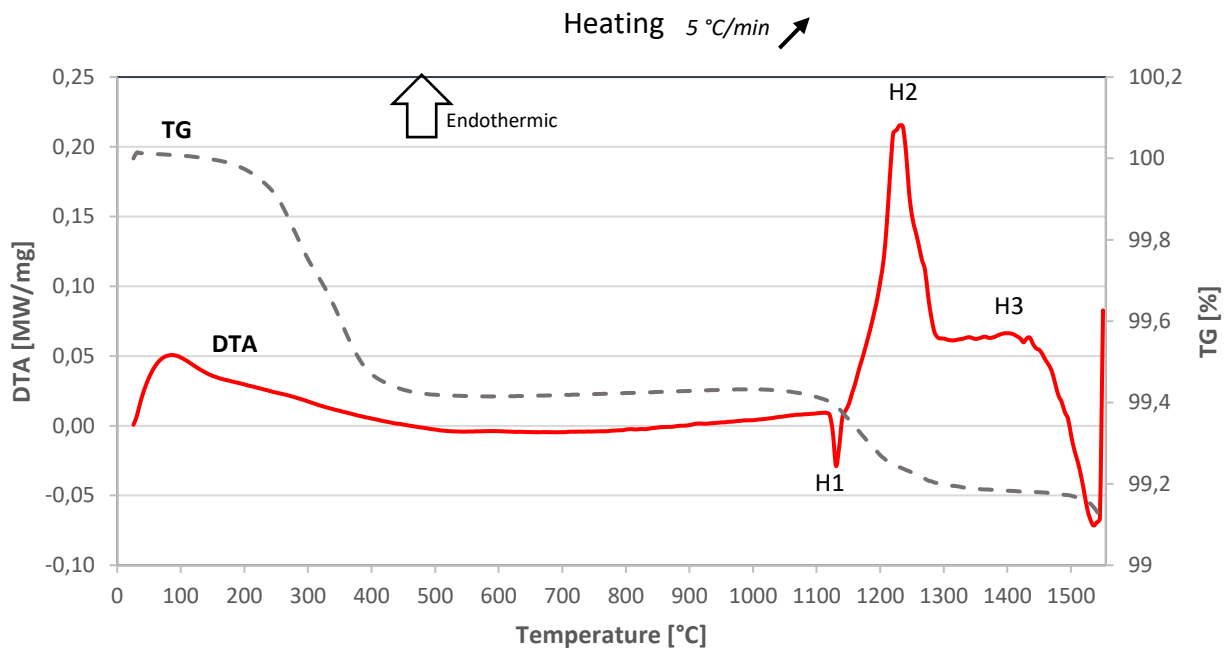


Figure 51: DTA and TG heating curve for SS316L+20%SiC powders

Peak	Start Temperature [°C]	Max/Min Temperature [°C]	End Temperature [°C]	Reaction or phase transformation
H1	1120	1130	1150	Oxidation
H2	1175	1236	1305	Austenite fusion
H3	1335	?	?	SiC fusion

Table 18: Principal heating peaks for SS316L+20%SiC powder

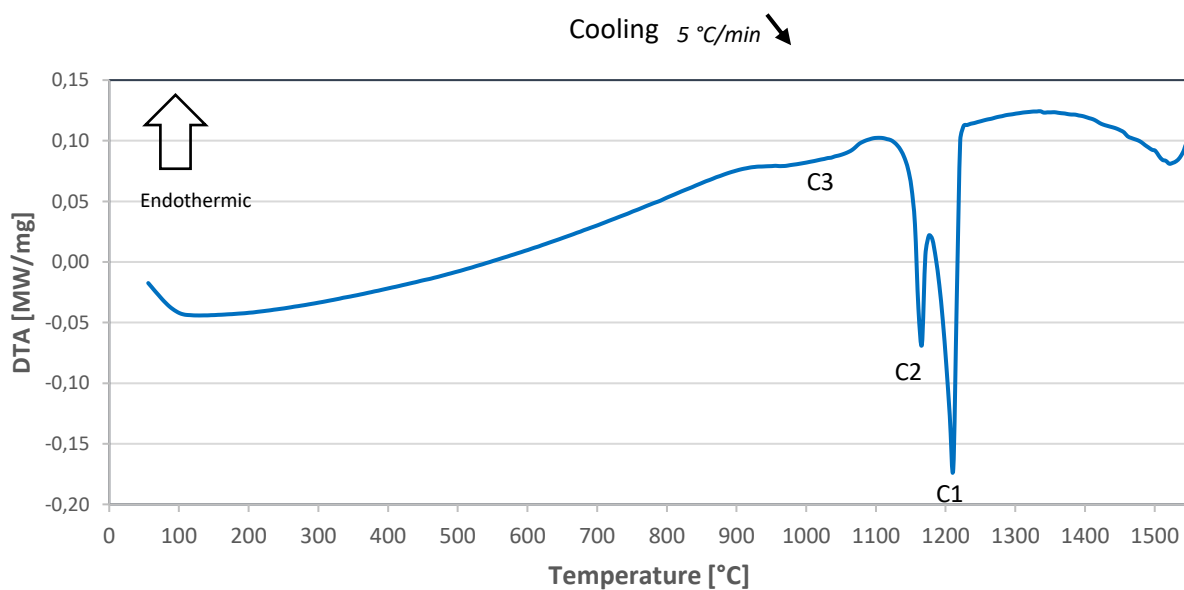


Figure 52: DTA cooling curve for 316L+20%SiC powder

Peak	Start Temperature [°C]	Max/Min Temperature [°C]	End Temperature [°C]	Reaction or phase transformation
C1	1231	1211	1181	Austenite solidification
C2	1181	1166	1130	M ₇ C ₃ solidification
C3	1086	1021	931	Precipitation of secondary carbides

Table 19: Principal cooling peaks for SS316L+20%SiC powder

OM observations on solidify powders are shown in Figure 53.

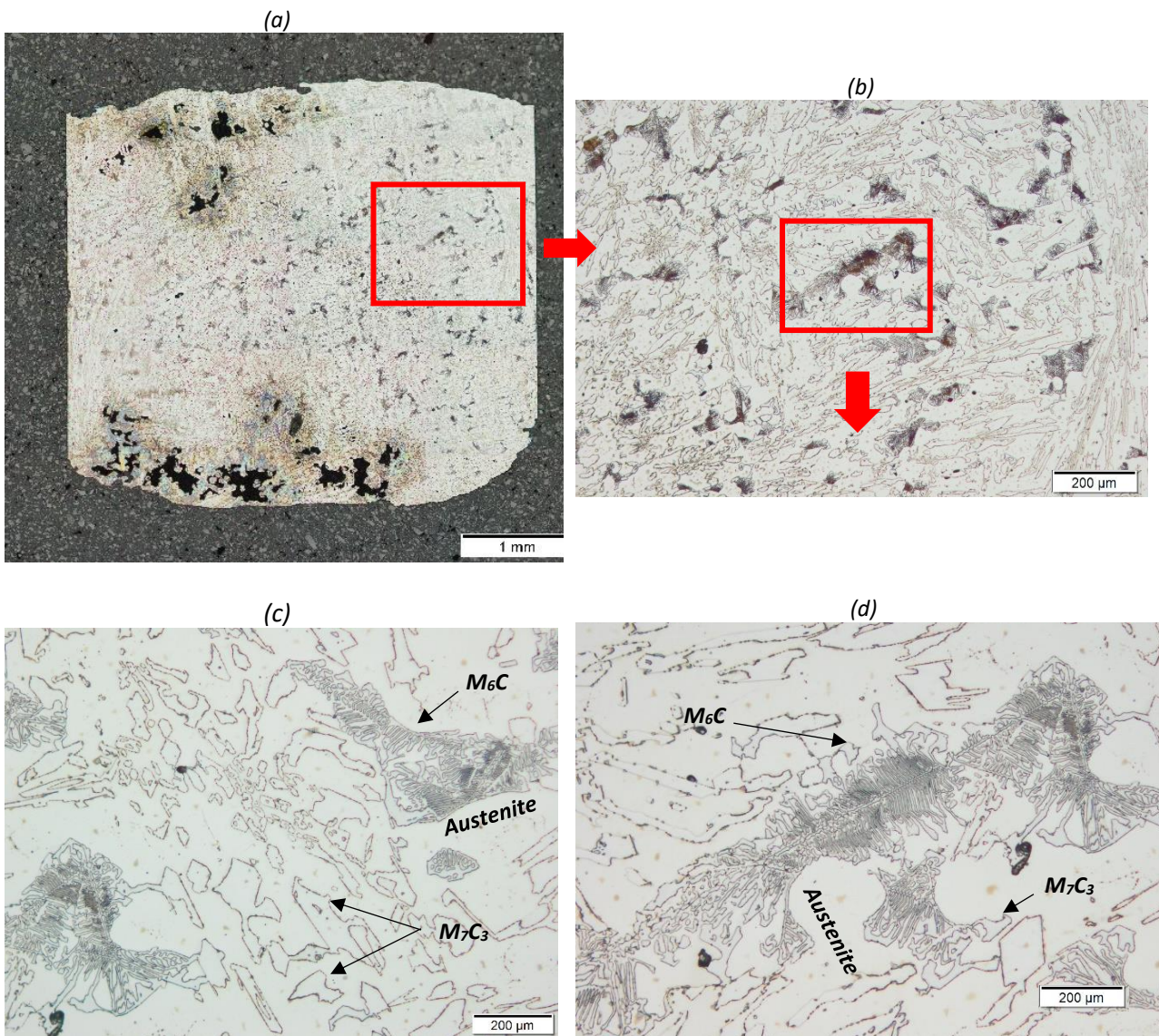


Figure 53: Optical microscope observation on SS316L+20%SiC powders after DTA tests

In the overview (Figure 53a) an inhomogeneous solidification can be noticed because of holes present on the top and on the bottom zone. The microstructure visible in Figure 53b presents high carbides density of different types. In fact, as indicated in Figure 53c-d there are M_7C_3 and M_6C . Both have big dimensions up to more than 200 μm . Most of M_7C_3 have polygon shape with a high surface, protrusions and cavities [36], while M_6C present a central thin line from where start ramification thin at the beginning and larger at the end [37]. Austenite is the first phase to be formed.

4.1.2 Milled powders

Different millings were done in order to achieve better results on the clad samples. The milling was performed on a powder mix of SS316L + 20% SiC and on SiC powder alone.

4.1.2.1 SS316L + 20% SiC powder

As explained in section 3.2.1 for this milling was done different stage. For each stage was checked a small quantity of powders with SEM.

- Stage 1

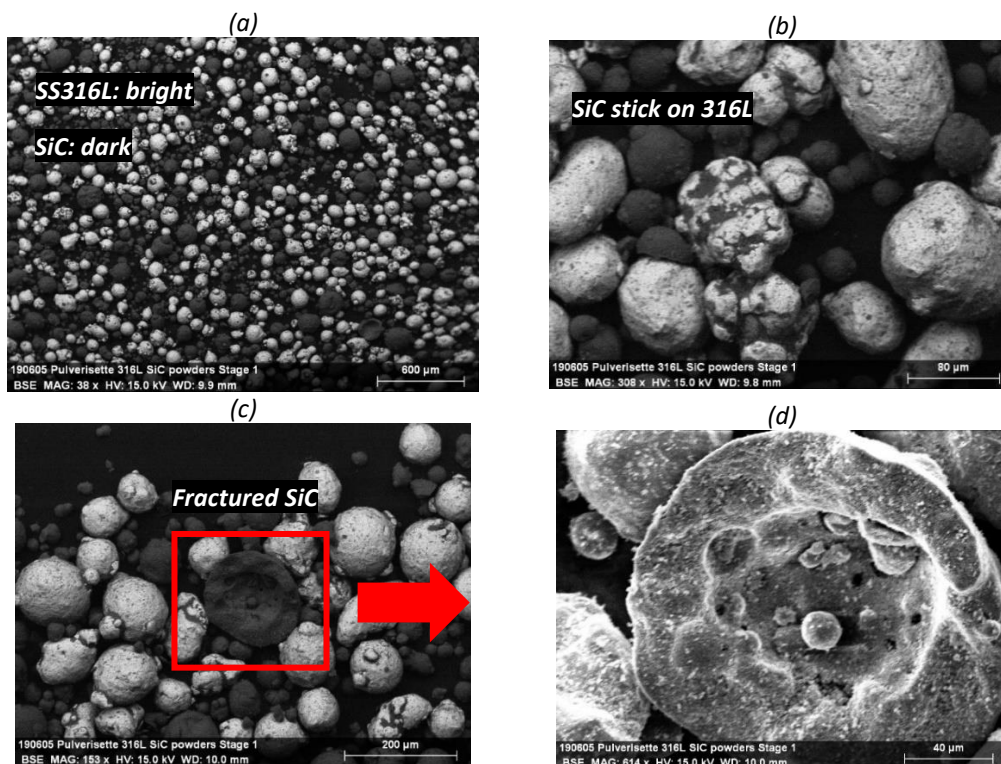


Figure 54: Stage 1 (30 min milling)

After 30 minutes of milling, the mixing is visibly homogeneous in Figure 54a. SS316L particles present SiC on the surface because of the continuous friction between them during the milling. The result of this is the stick of SiC on SS316L (Figure 54b).

An important observation of this stage is the presence of SiC cavities particles: in fact as is possible to notice from Figure 54c-d, the SiC particle is fractured and inside of it there is a big cavity.

- Stage 2

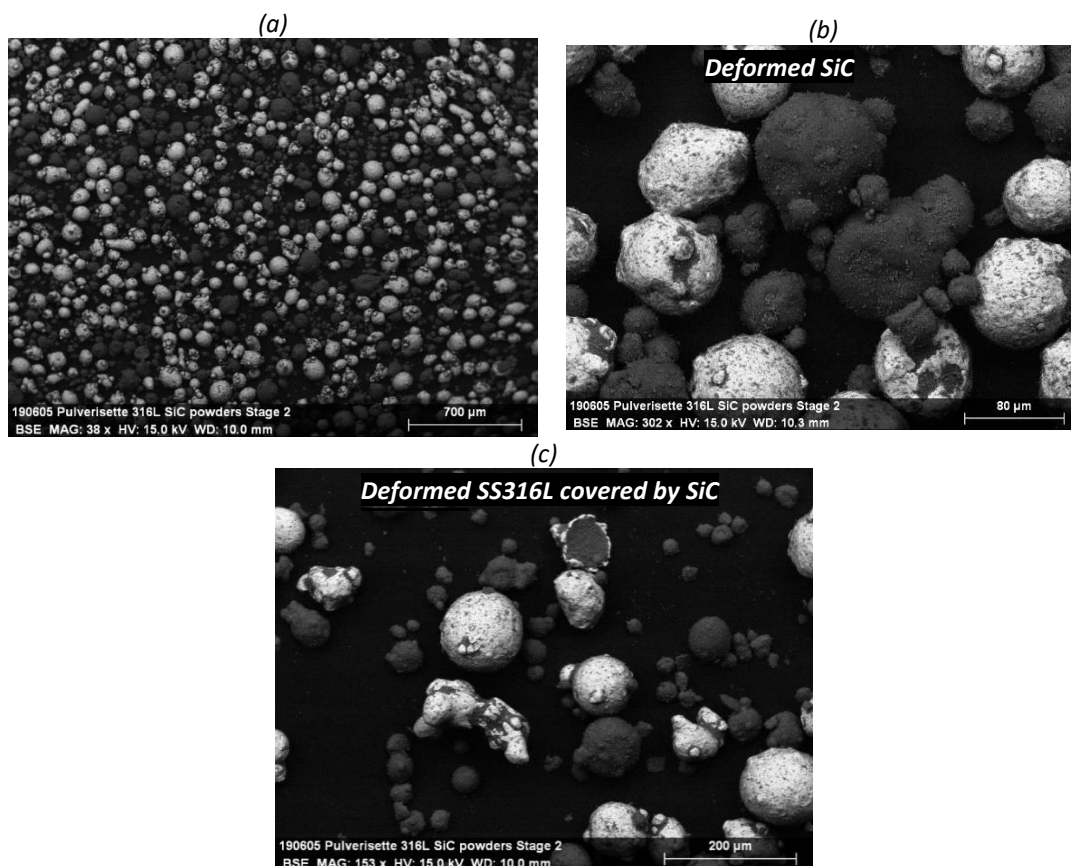


Figure 55: Stage 2 (1 h milling)

After 1 hour of milling, SiC and SS316L particles start to deform (Figure 55b). The phenomenon of SiC on SS316L surface and fractured SiC particles increases, due to the more contact time between the two different powders, as is possible to see in Figure 55c: on the top part is visible a deformed SS316L particles covered by SiC.

- Stage 3

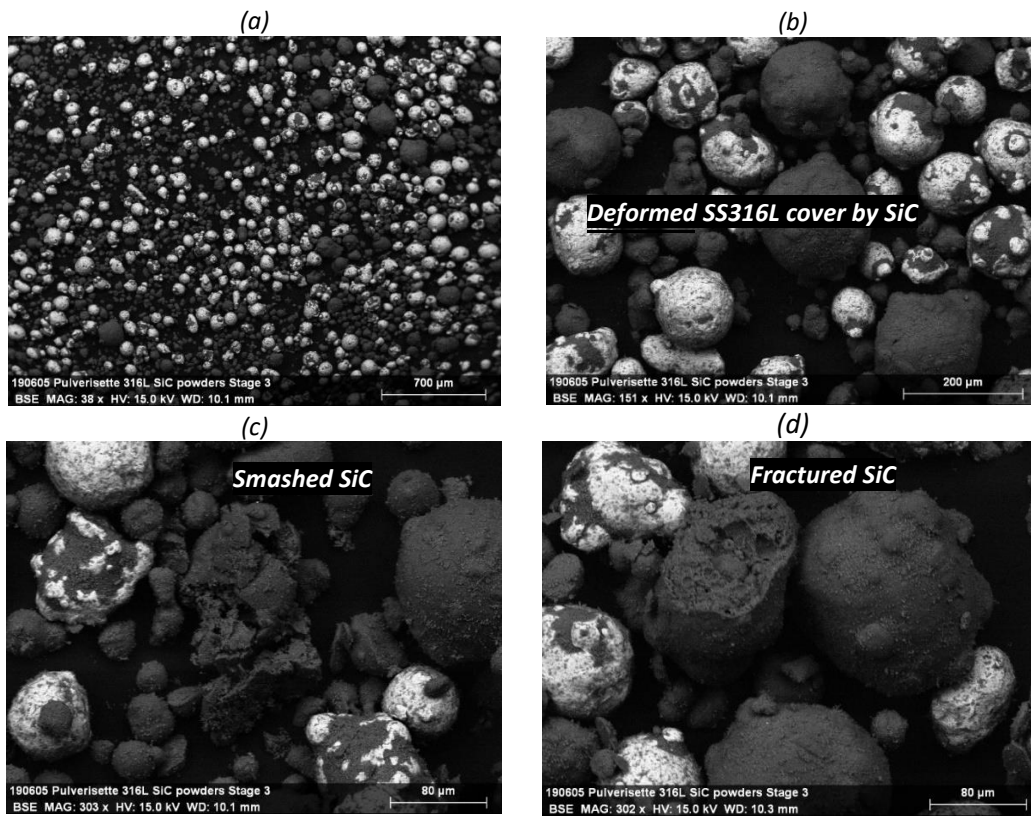


Figure 56: Stage 3 (2 h milling)

After 2 hours milling more SiC is stick on SS316L particles (Figure 56b). SiC particles dimension is lower than the previous stage because the number of fractured particles is increased. Some of SiC particles are smashed (Figure 56c-d), and this leads to many small fragments with irregular shape.

- Stage 4

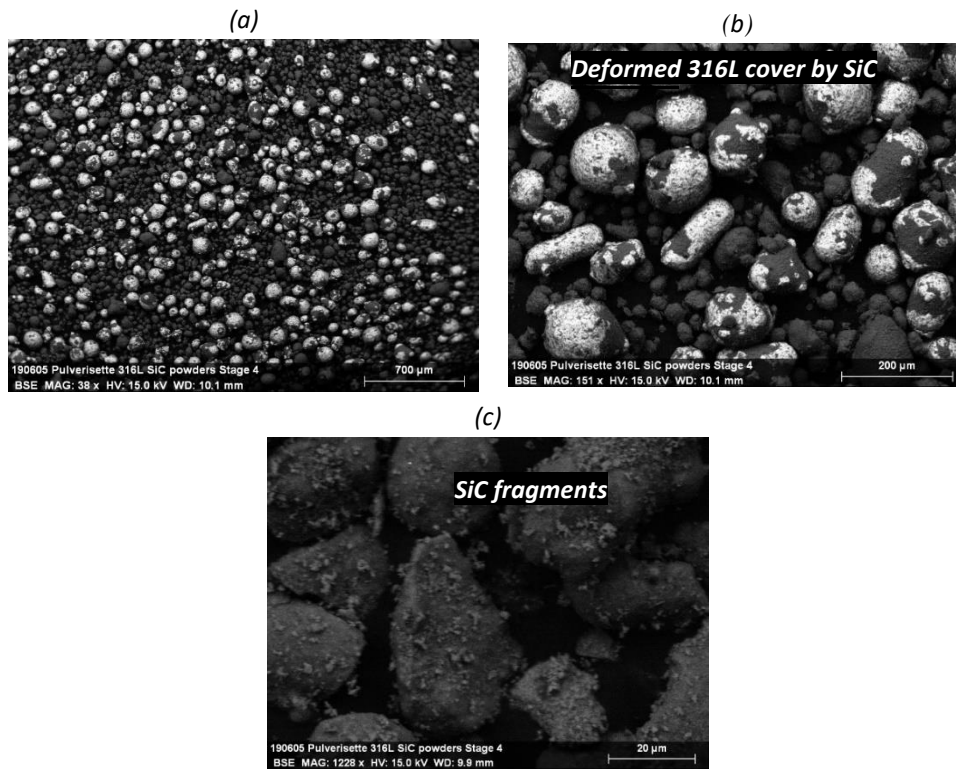


Figure 57: Stage 4 (4 h milling)

After 4 hours milling there are several SS316L deformed particles, with a large part of the surface covered by SiC (Figure 57b). The number of fragments of SiC particles is increased, as is possible to see in Figure 57c: some scraps are less than 20 μ m.

- Stage 5

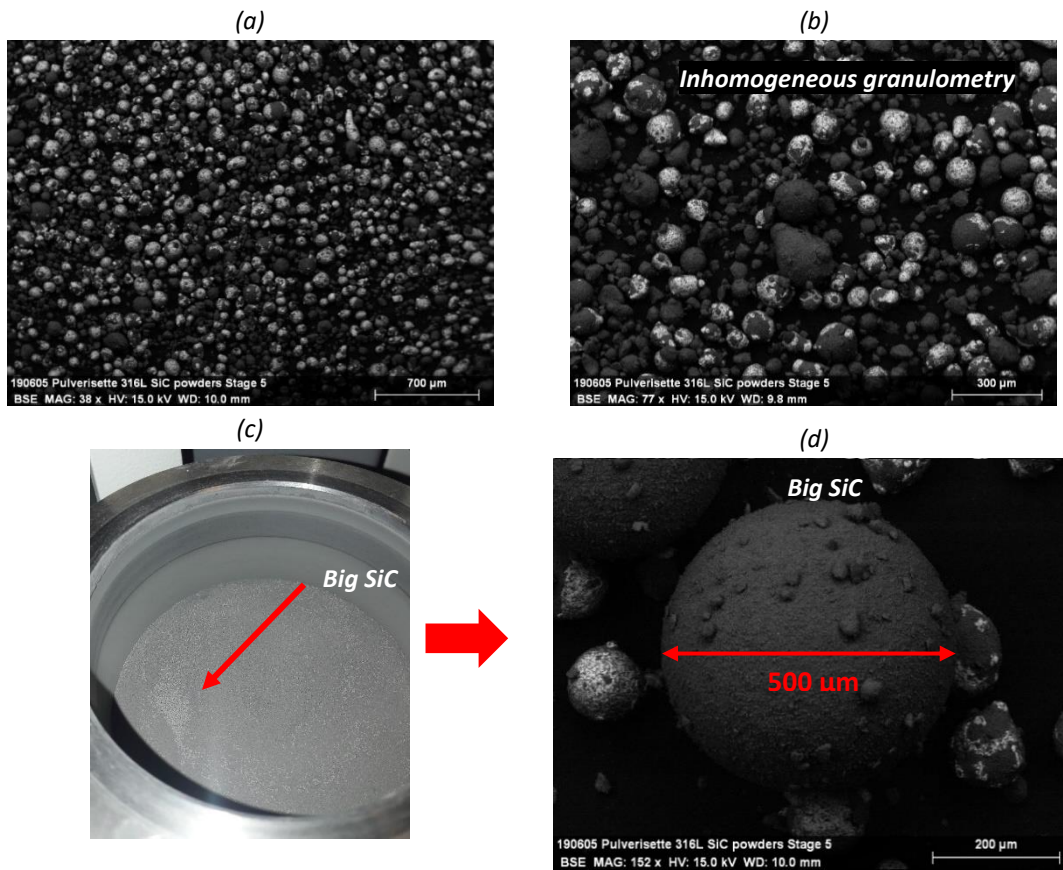


Figure 58: Stage 5 (6 h milling)

After 6 hours milling there is not a homogeneous granulometry because the dimension of powders changes from particle to particle (Figure 58b). When the bowl was opened, on the surface there were several big grey particles. The dimensions of them is up to 500 μm Figure 58c-d.

DTA heating curves for each stage are shown in Figure 59.

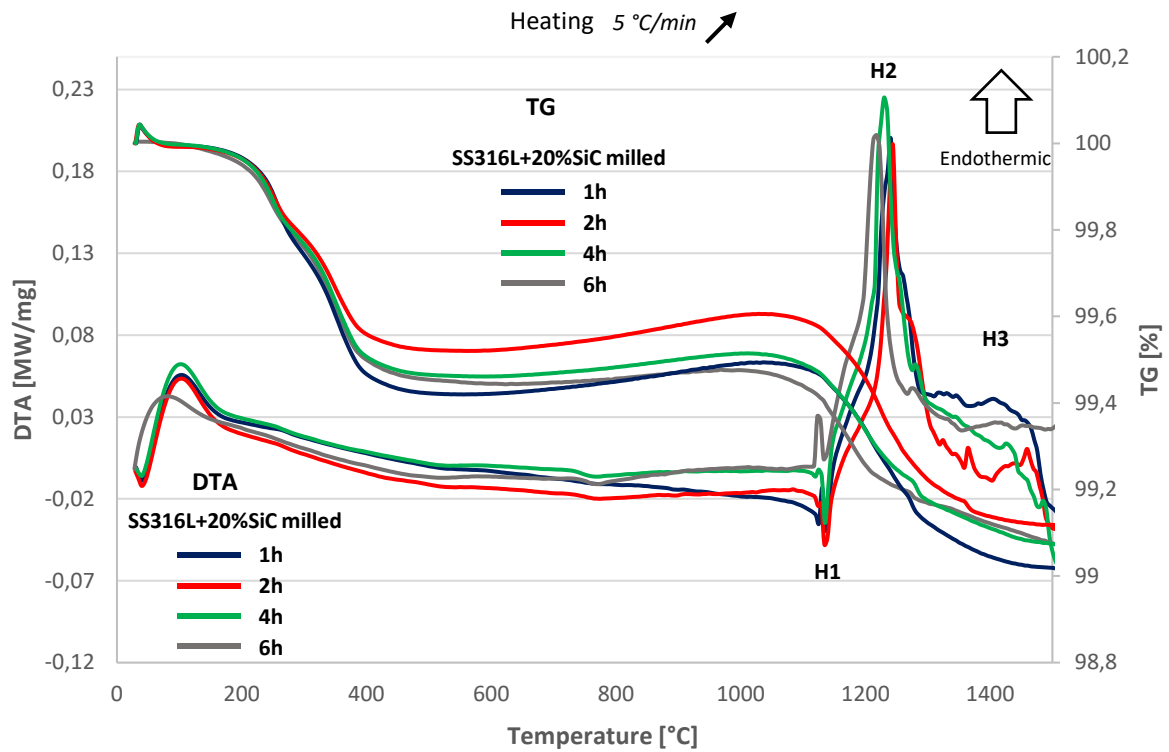


Figure 59: DTA & TG heating curves for SS316L+20%SiC powders

Peak	Start Temperature [°C]	Max/Min Temperature [°C]	End Temperature [°C]	Reaction or phase transformation
H1	1110	?	1150	Oxidation/Reduction
H2	1140	1220	1270	Austenite fusion
H3	1280	?	?	SiC fusion

Table 20: Principal heating for 316L+20%SiC milled powders

4.1.2.1 Silicon Carbide powder

For the milling of SiC powders different parameters were changed, in particular the ball to powder weight ratio and the milling time, as was explained in chapter 3.2.2.

Figure 60 shows the milling effect for each set up with two different magnification.

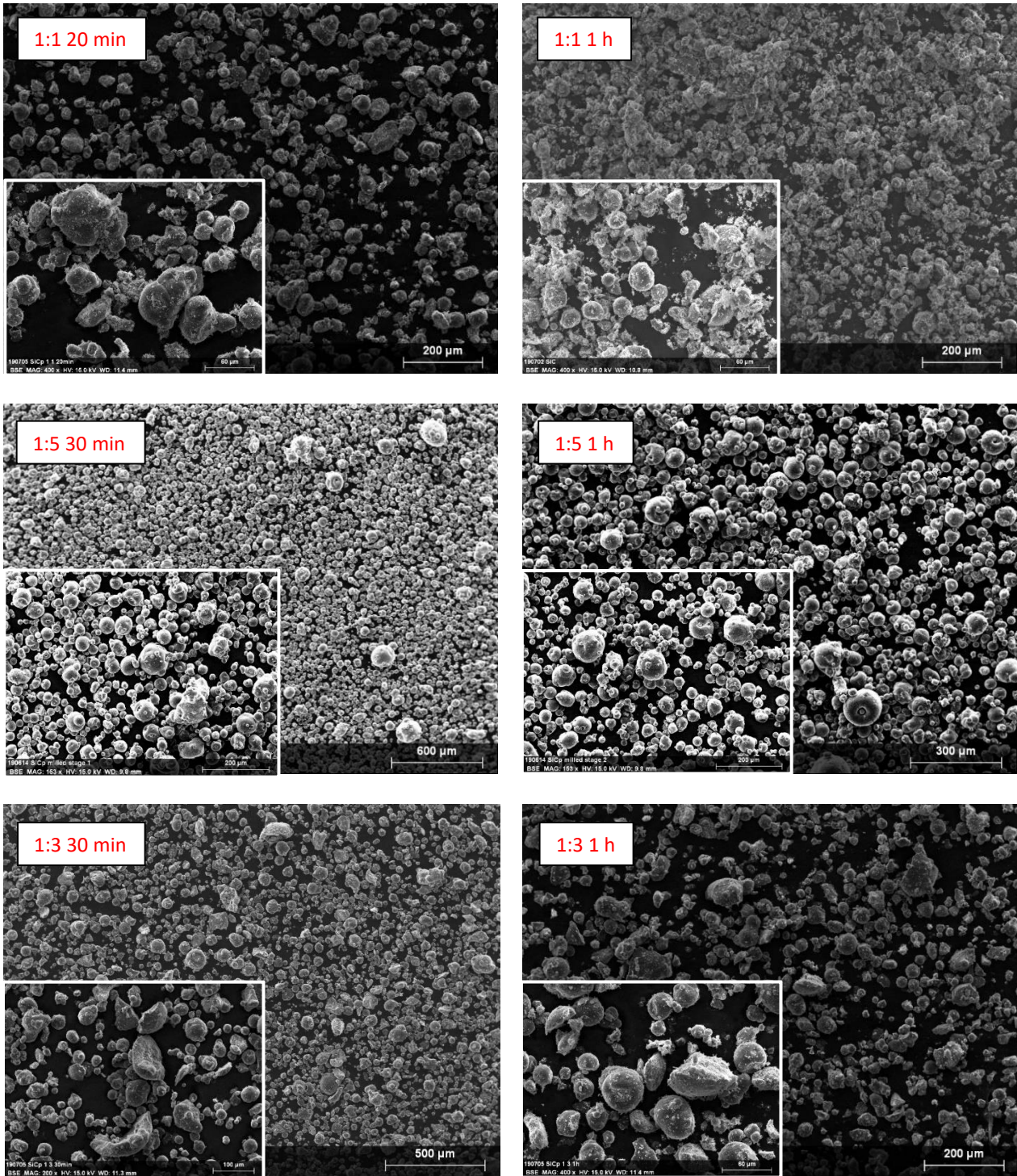


Figure 60: SEM micrograph of different milling on SiC powders

Referring to Figure 60, milled powders with ball to powder ratio of 1:1 were checked after 20 minutes and after 1 hour of milling. For both this milling time, the result is not good because powders have suffered a strong milling due to the high number of balls. In fact, is possible to notice after 1 hour that some particles are completely destroyed.

The balls number was decreased to a ball to powder ratio of 1:5. In this case the result is the contrary of the previous because the milling is not enough strong to deformed and fractured the particles, both after 30 minutes and 1 hour.

The ball to powder ratio was changed in 1:3 increasing balls number, and powders were checked after 30 minutes and 1 hour. After 30 minutes only big particles are smashed. Instead after 1 hour the milling is stronger because the number of small fragments is increased.

DTA tests were done on powder 1:5 after 30 minutes and on 1:3 after 1 hour. Both these milled SiC powders were mixed with original SS316L powders. The DTA curve is shown in Figure 61.

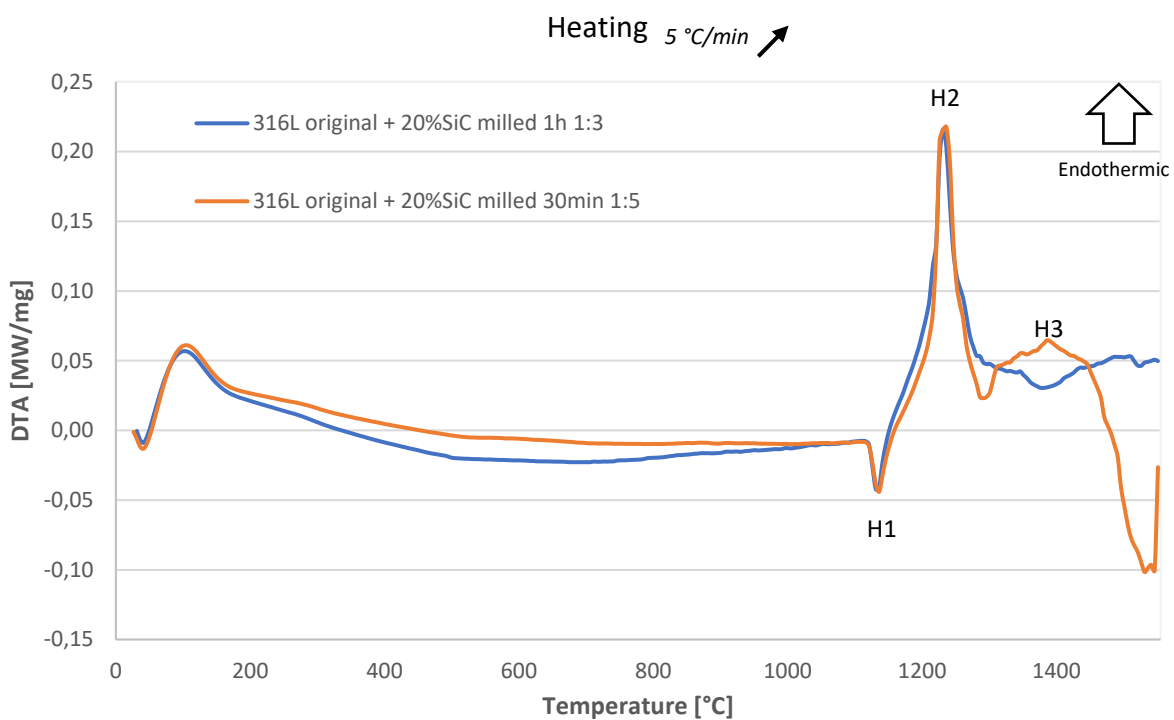


Figure 61: DTA heating curve for SS316L original + 20%SiC milled powders

Peak	Start Temperature [°C]	Max/Min Temperature [°C]	End Temperature [°C]	Reaction or phase transformation
H1	1116	1135	1146	Oxidation
H2	1150	1230	1300	Austenite fusion
H3	1280	?	1520	SiC fusion

Table 21: Principal heating peaks for 316L original + 20%SiC milled

X-Ray Diffraction (XRD) was performed on the following powders (Figure 62): SS316L original, SiC 1:3 1 hour milling, SS316L + 20% SiC 1:5 1 hour milling. The aim was to check the possible formation of phases on SS316L + 20% SiC after milling.

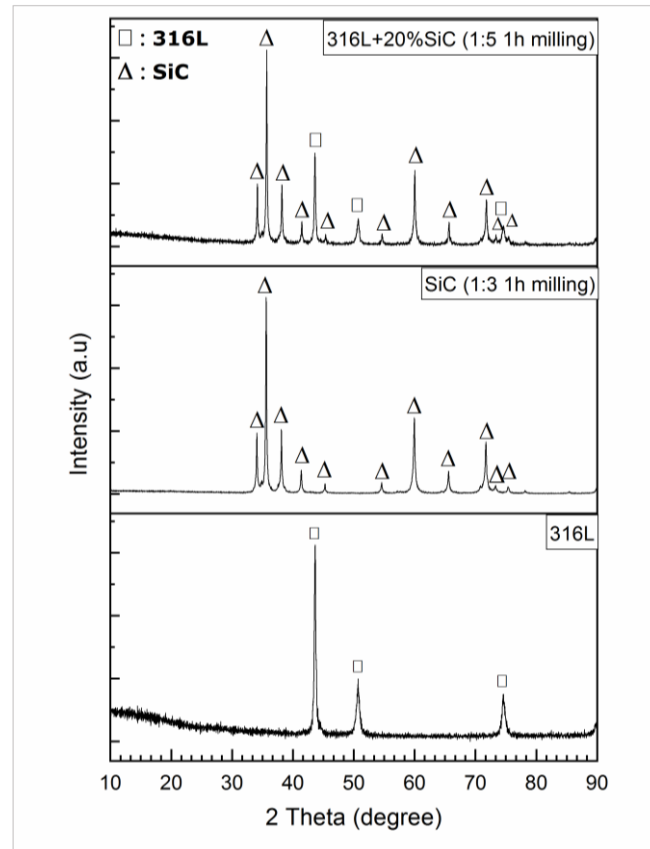


Figure 62: XRD on powders

With this analyse is shown that there is no formation of intermetallic phases as Fe+Si in the mix SS316L + 20% SiC powders. In fact, the recognise peaks of SS316L and SiC (1:3 1h milling) correspond to the peaks of 316L + 20% SiC (1:5 1h milling).

4.2 Laser cladded deposits characterization

The results of laser cladded deposit characterization include microscopy observations and thermal analyses. First the results on the sample S10.0 and subsequently the sample S20.0 are presented. For S10.0 a macro-hardness test on the internal section was done.

4.2.1 Cladded deposit SS316L + 10% SiC

4.2.1.1 Microscope observations

The sample S10.0 was observed with OM.

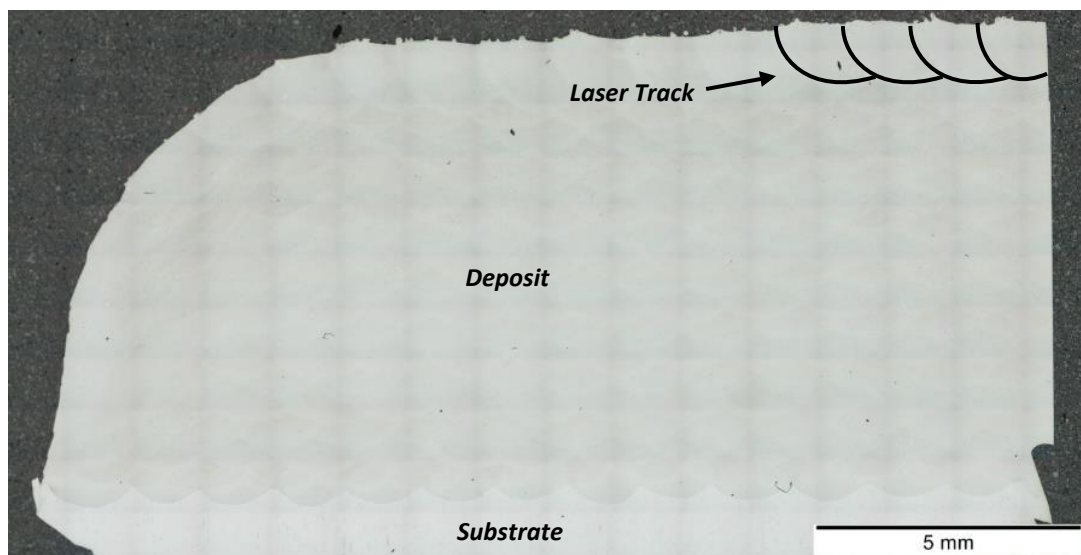


Figure 63: Overview of sample S10.0

Microscope observations were performed on the left side of the sample S10.0 Figure 63, where the laser tracks are highlighted.

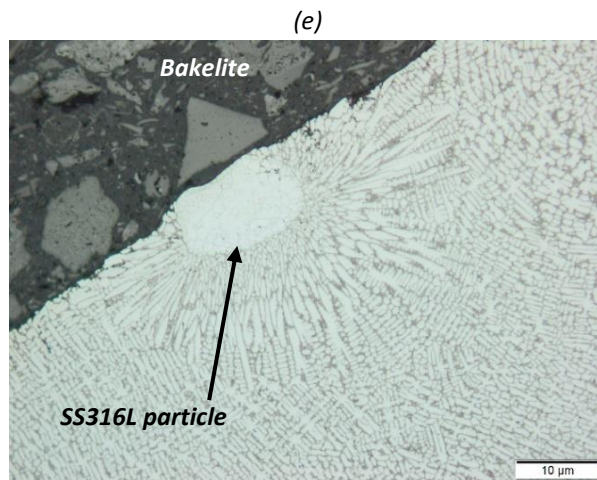
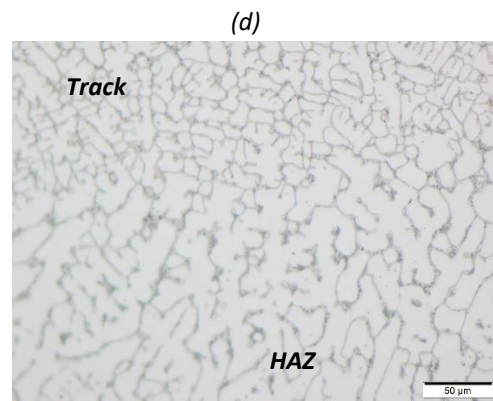
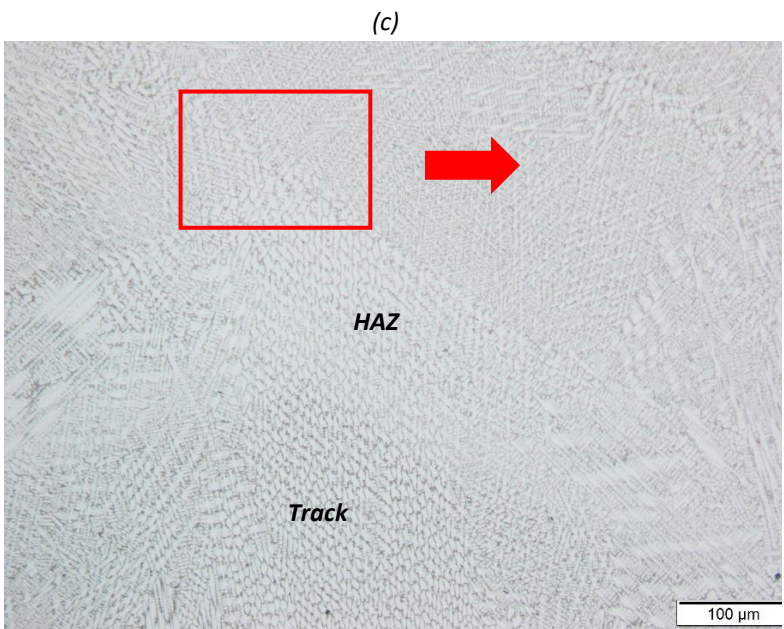
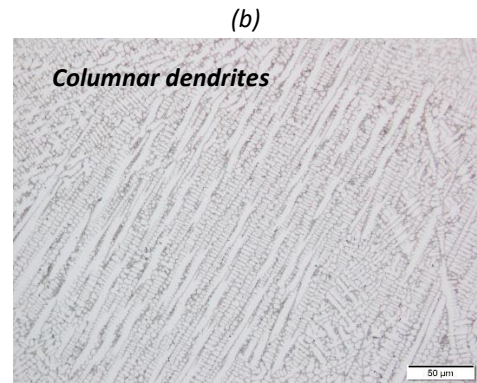
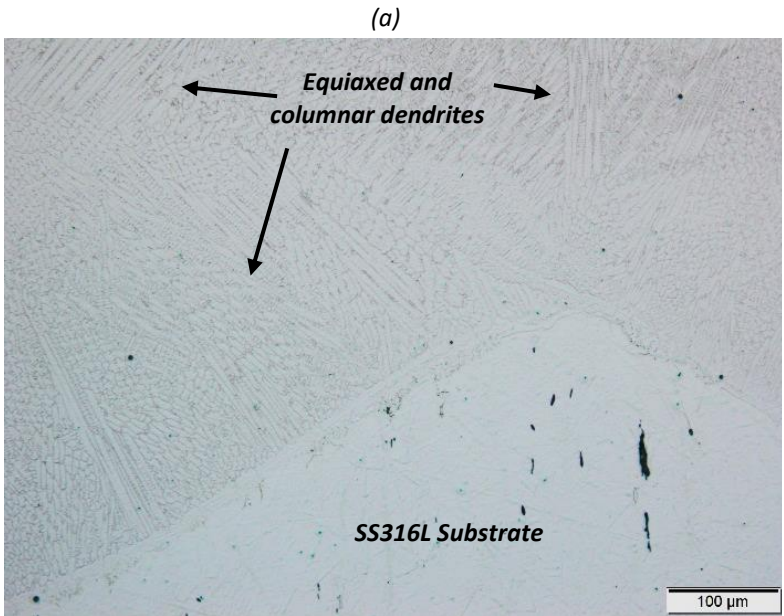


Figure 64: Optical microscope observations on S10.0

Focusing on the boundary between the substrate and the deposit (Figure 64a-b) two different type of microstructure, columnar dendrites and equiaxed dendrites are indicated. They start to grow from the substrate.

Figure 64c-d correspond to the central part of the deposit. In this area the two different zones are present: Track and Heat Affected Zone (HAZ). Referring to Figure 64d the difference between them is clear. The track is characterized by an interconnected network carbide, meanwhile the Heat Affected Zone is composed by an unconnected structure with a lower carbides density.

In the external surfaces of the deposit are present many unmelted SS316L particles. They get trapped in the deposit and from their surface start growing dendrites in radial direction (Figure 64e).

Track and HAZ were further investigated with SEM.

First the bottom right corner of Figure 64a was observed. In particular, the zone indicated by the red square.

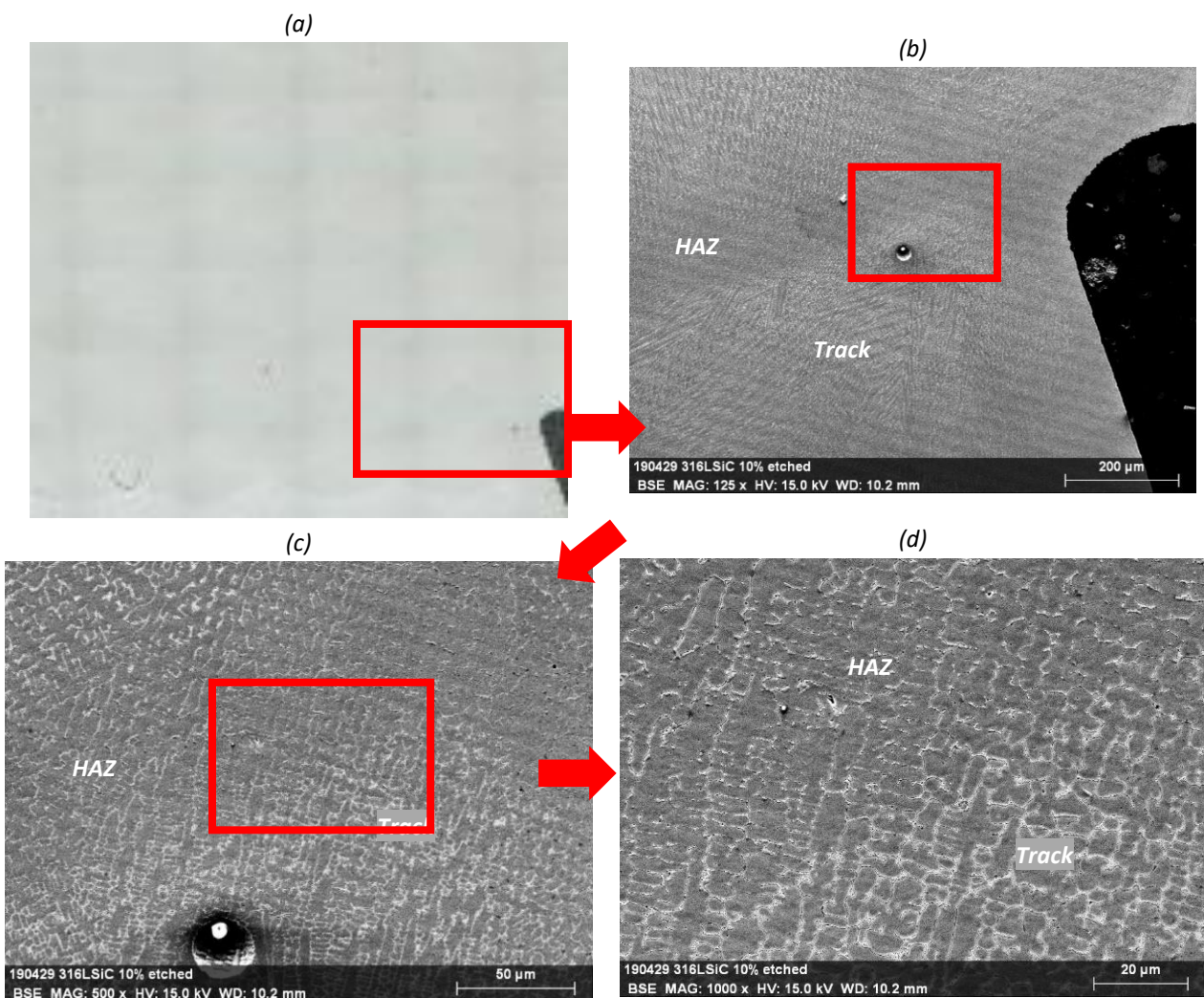


Figure 65: SEM micrograph of sample S10.0

Figure 65b shows different zones as marked by the different shades of grey, corresponding to different microstructures. In the bottom part of the micrograph is present a bright grey zone containing some equiaxed and columnar dendrites. Above the first zone a small darker area is observed, but the microstructure cannot be resolved due to the low magnification. Finally, at the top, another bright grey zone with columnar dendrites is visible. Figure 65b is useful as it offers the possibility to appreciate the boundary between the bright and the dark zones. In order to check the difference between these zones, in Figure 65c-d is shown a close up on the boundary.

Figure 65d allows to see the different carbide structure with better quality than the others figures. In comparison with Figure 65b, the bright zone corresponds to the track, while the dark zone corresponds to the heat affected zone.

Afterwards, an investigation on the track was done.

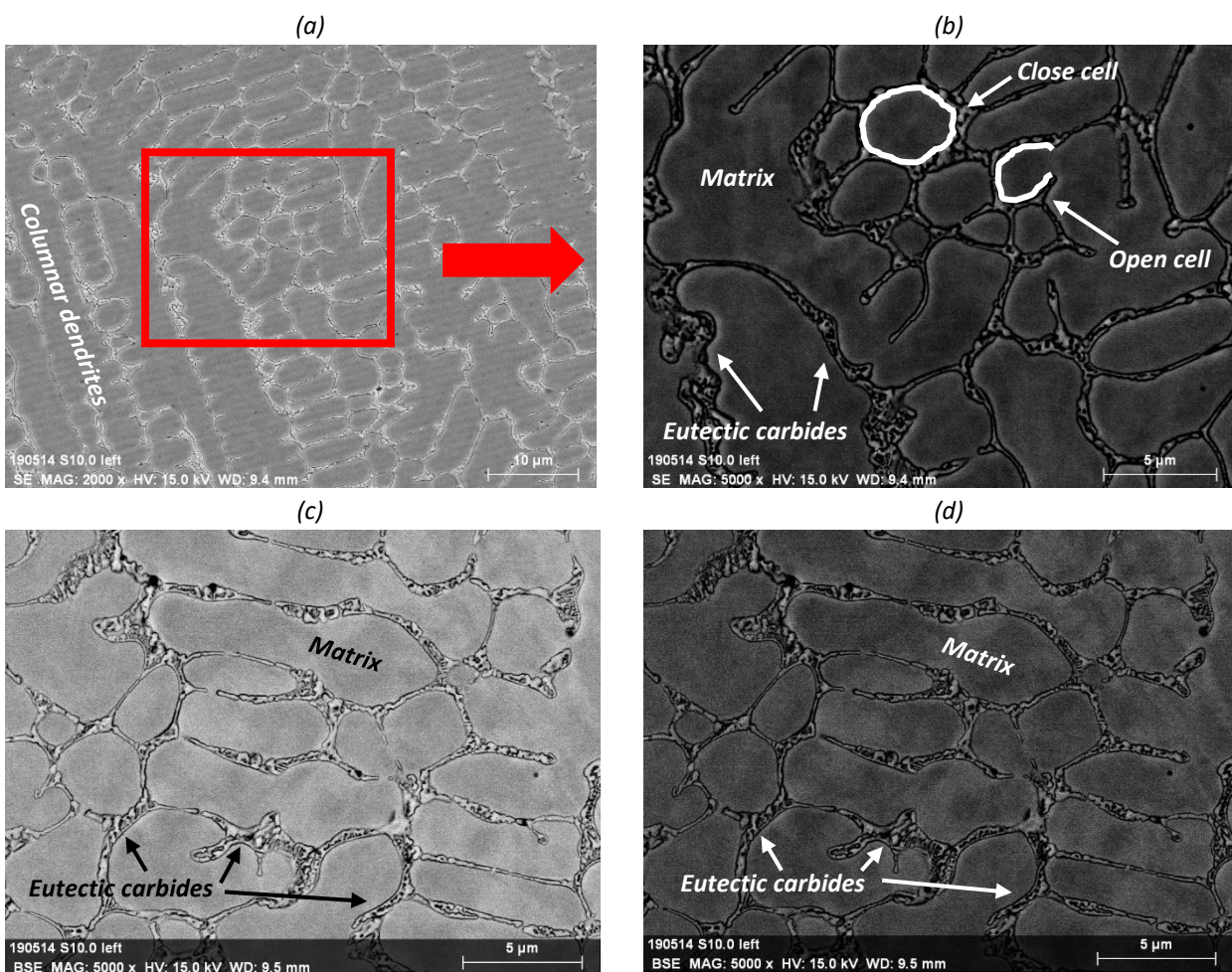


Figure 66: Track zones

In Figure 66 different micrographs of microstructure on the track are shown, in SE or BSE mode at different magnification. Figure 66b is a focus in BSE mode of Figure 66a, while Figure 66c-d are the same zone but in SE and BSE mode respectively.

The matrix can be distinguished from carbide networks. In particular eutectic carbides present different colours. In BSE mode the phases with element with high weight are bright, meanwhile the phases with lightweight elements are darker.

The microstructure of the track is characterized by columnar and equiaxed dendrites, in which completely closed cells or opened they can form, as is visible in Figure 66b.

To check the nature of the phases present on the track zone, some chemical analyses were performed. The quantity of Cr, Mo and C was checked in particular in the zones where carbides are visible, while for the matrix the attention was focused on iron.

In Figure 67 is shown the zone and the line where the chemical analyse was performed.

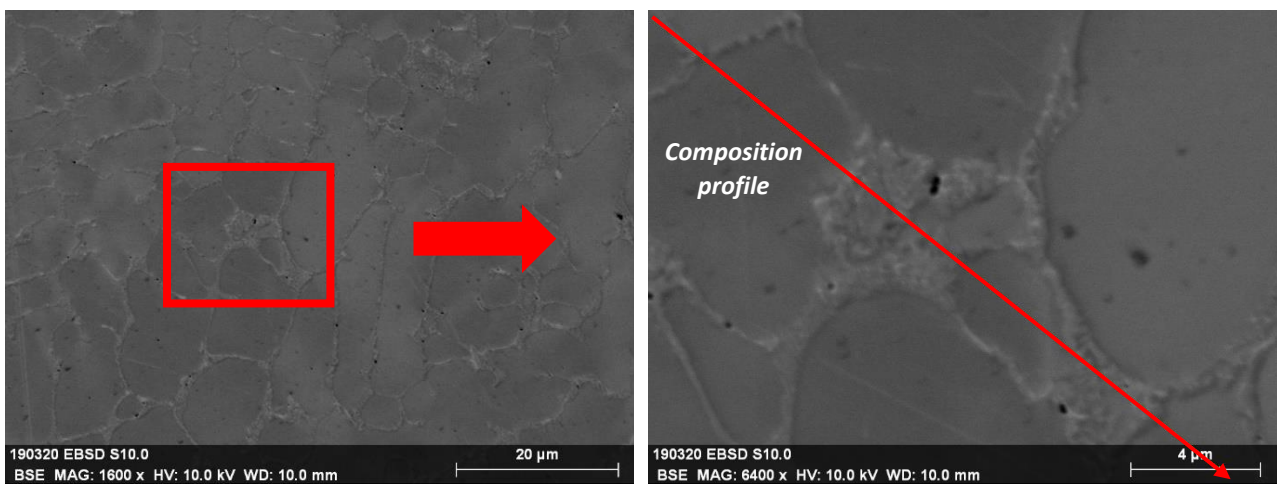


Figure 67: Chemical analyse zone on the track

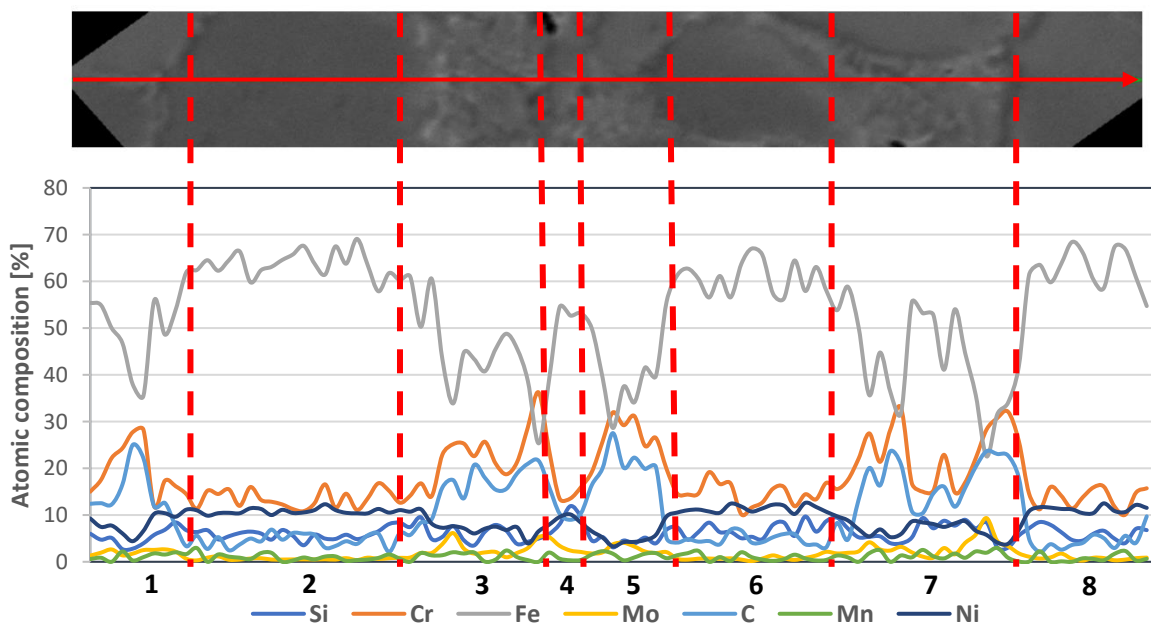


Figure 68: Composition profile on the track zone

Atomic Composition [%]

Zone	Si	Cr	Fe	Mo	C	Mn	Ni	Phase
1	5,41	18,74	51,23	1,81	12,90	1,36	8,55	Cr-Mo carbide
2	6,05	13,78	62,82	0,77	5,04	0,88	10,67	Matrix
3	5,74	22,85	43,26	2,69	16,96	1,40	7,12	Cr-Mo carbide
4	6,82	22,15	44,04	3,16	15,62	0,95	7,27	Cr-Mo carbide
5	4,99	25,45	42,64	2,55	17,05	1,25	6,06	Cr-Mo carbide
6	6,57	14,42	61,01	0,71	4,91	0,94	11,44	Matrix
7	6,64	21,37	45,79	2,84	14,50	1,28	7,58	Cr-Mo carbide
8	5,89	13,98	62,69	0,77	4,72	0,67	11,27	Matrix

Table 22: Atomic compositions [%] on the track

Table 22 illustrates the difference in composition between the matrix and carbides. In particular the amount of C in the carbides is higher than the matrix, as expected. The contrary is for iron. The carbides forming elements are Cr and Mo, in fact they are present in high amount in zones 1,3,5,7. There is no presence of Si carbides, because the amount of Si is similar in the matrix and in carbides. At the light of this results, the track is characterized by the presence of Cr – Mo eutectic carbides.

After the investigation on the track, a focus on the Heat Affected Zone was done. In Figure 69 some micrographs from SEM are present, in different position of the sample and with different magnification.

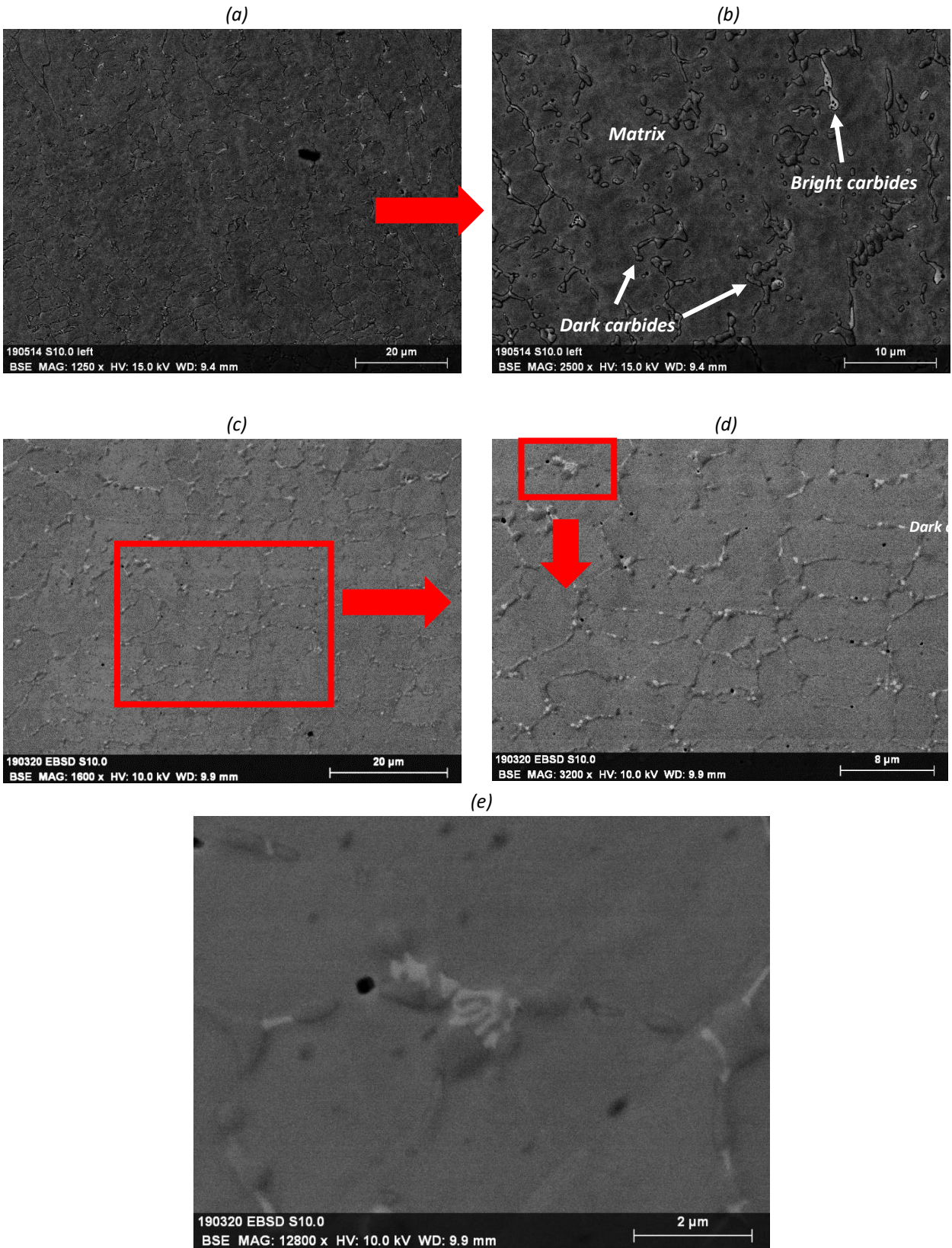


Figure 69: Heat Affected Zone

In the heat affected zone there is not the presence of a carbides network but there are different types of isolated carbides. Bright and dark carbides are clearly distinguished (Figure 69b). They have a different morphology: dark carbides present a globular or thin shape, instead bright carbides present a lamellar shape. It is possible to notice that the carbide is not formed by a single phase but by two different phases (Figure 69e).

In the zone of Figure 69b a composition profile was done (Figure 70).

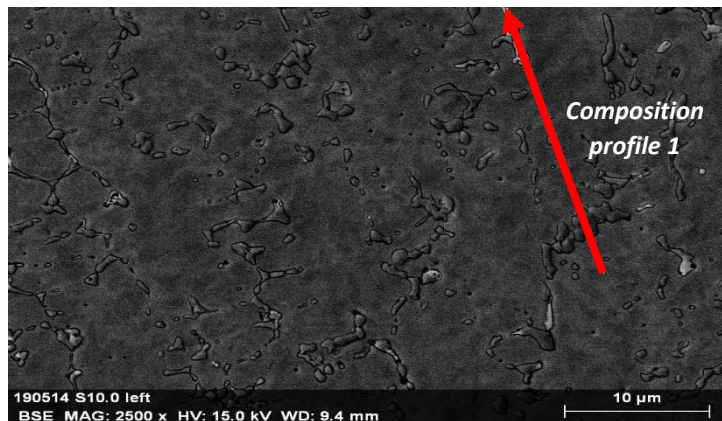


Figure 70: Chemical analyse 1 on the heat affected zone

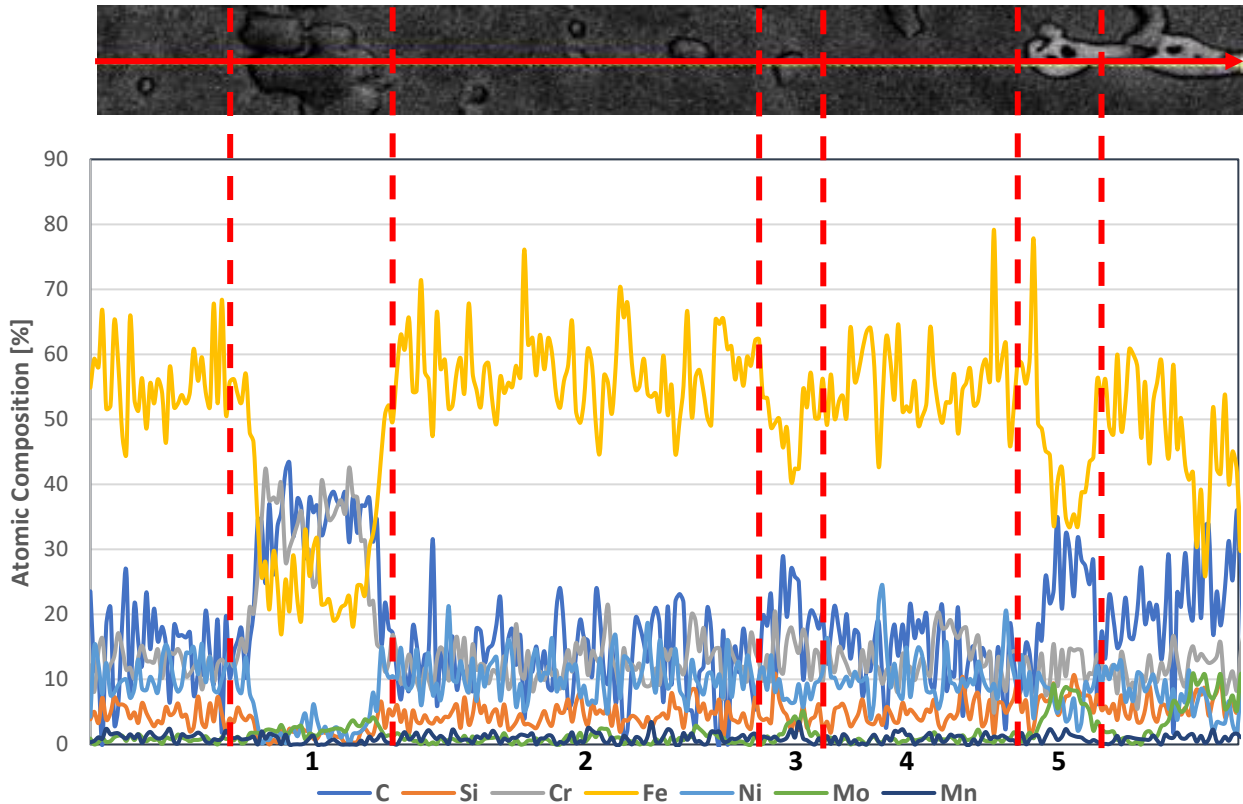


Figure 71: Composition profile on the heat affected zone

Atomic Composition [%]								
Zone	C	Si	Cr	Fe	Ni	Mo	Mn	Phases
1	32,64	1,83	30,71	28,38	3,54	2,29	0,58	Cr carbide
2	13,56	4,47	12,49	57,02	10,64	0,80	0,99	Matrix
3	20,20	4,62	14,14	49,17	8,61	2,21	1,02	Cr carbide
4	13,78	4,83	13,08	55,76	10,85	0,81	0,86	Matrix
5	21,47	6,11	11,22	48,03	8,37	3,84	0,93	Mo carbide

Table 23: Atomic compositions [%] on the heat affected zone

Checking the values of C and Fe in the zone 2 and 4, it is possible to notice the presence of the matrix. Instead zones 1, 3, 5 correspond to a carbide composition because of the high amount of C. It is possible to distinguish the two type of carbides discussed above: dark and bright carbide. The dark carbides are in zones 1 and 3. In this case zone 1 has a higher amount of C than zone 3 because it is a coarsened carbide. The same is valid for the quantity of Cr. The dark regions are Cr carbides. While the bright carbide in zone 5 has less quantity of Cr than dark carbide in zone 1, but there is a higher amount of Mo. The bright regions are Mo carbides.

In addition to chemical analyses, the Electron Backscattered Diffraction (EBSD) analyses was carried out. The aim of this was to examine the crystal lattice of various phases of the microstructure, in order to identify them together with the classical microscopy. The phases considered for the investigation are shown in Table 24.






Phase	Colour
Austenite	
Iron silicide	
Cr ₇ C ₃	
(Cr,Mo) ₂₃ C ₆	
(Fe,Mo) ₃ C	

Table 24: EBSD phases

The zones of the EBSD analysis is on the right of a macrohardness indent. This zone was chosen since exhibit the transition from the track microstructure (on the left) and the HAZ (on the right) (Figure 72b-c).

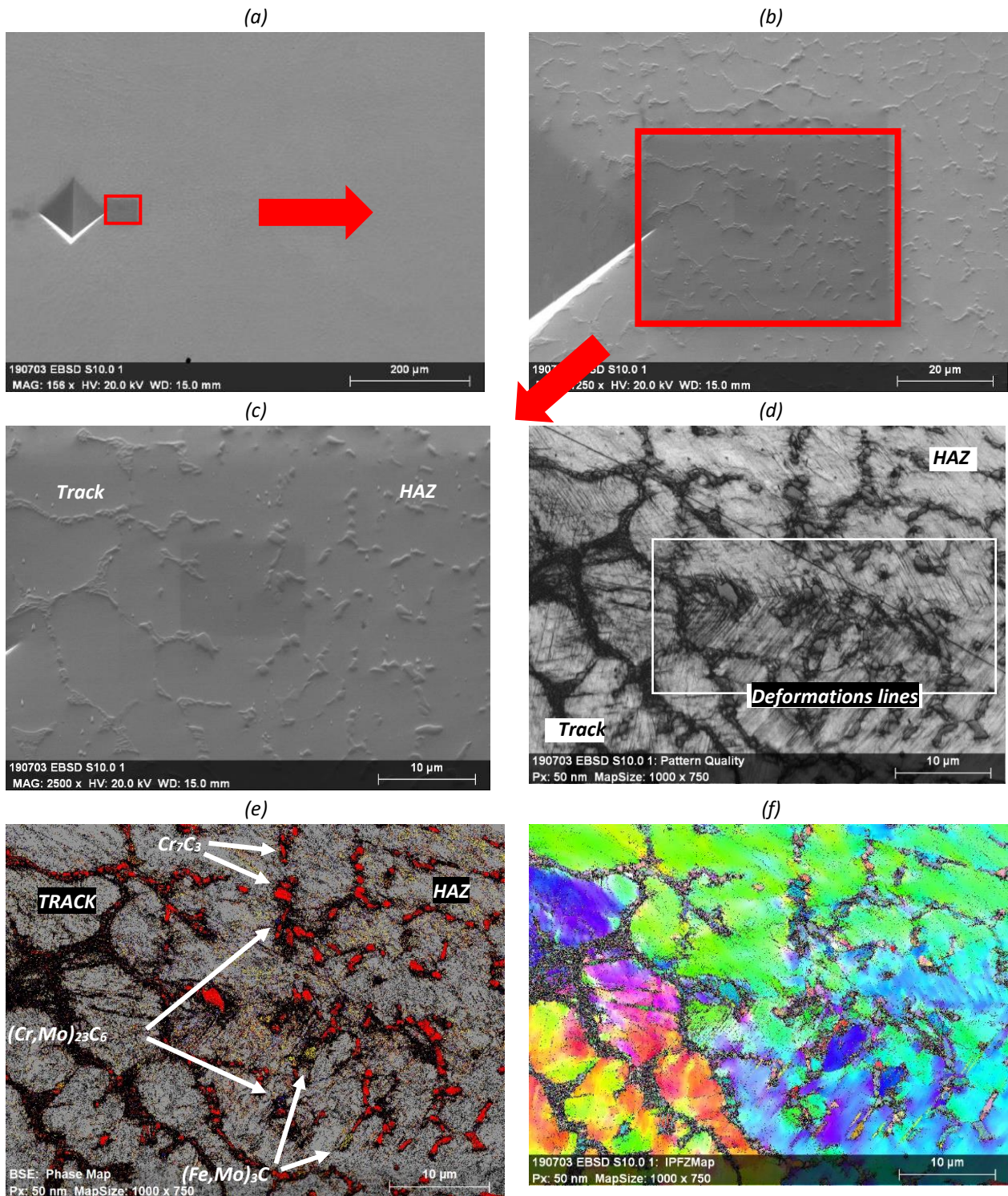


Figure 72: EBSD on sample S10.0

Figure 72a-b-c show the EBSD zone with an increasing magnification. With the pattern quality (Figure 72d) it is possible to understand if the EBSD analysis had a good result. The darker zones mean a low-quality result because the lattice structure was not well indexed. While the bright zones mean a good indexation. The phases in the heat affected zone had a better indexation than the track phases,

especially the carbides network. As it is indicated, it is possible to see many diagonal lines converging in the same zone of the micrograph: they are the consequence of the deformation induced by the macro-indentation.

In Figure 72e the phase map is shown. The grey colour corresponds to Austenite, in fact it is situated in the matrix areas. The other main identified phase is Cr_7C_3 carbide (red) with an orthorhombic lattice. This phase is present in high quantity in the heat affected zone. Moreover, it is possible to see $(\text{Cr},\text{Mo})_{23}\text{C}_6$ carbides in the blue areas with a face cubic centred structure. The yellow points represent a Fe – Mo carbide (M_3C). This phase is located in the transition zone of track and HAZ.

In Figure 72f it is possible to notice different coloration in the matrix areas. Each colour represents a different solidification direction of the austenite, because of the different angle in the crystallography orientation of the austenite phase. The solidification starts during the laser cladding process and it can have different directions.

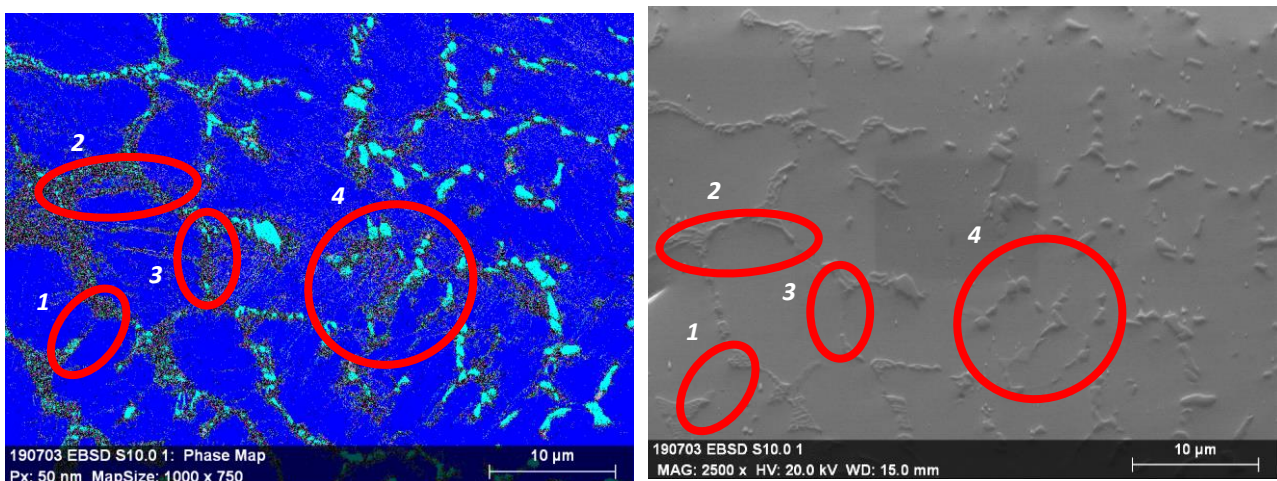


Figure 73: EBSD phase map vs SEM micrograph

In Figure 73a the same analyse is shown, with less matching bonds and then less constraints for the identification of the phases in the dark zones of the pattern quality. The result is shown in order to have some insights about those dark zones. Four of those intercellular zones are highlighted with red circle. In the EBSD phase map (Figure 73a) an agglomeration of points are observed, while in the SEM micrograph (Figure 73b) they are not clearly visible. All the zone of the carbides network in this case correspond to iron-silicide phases, but a careful interpretation of this is mandatory, because in the previous EBSD with high matching bonds these phases are not presented.

These iron – silicide phases form a connection between different zones of the carbide network, as it is visible in the comparison of Figure 73a-b. But considering the EBSD of Figure 72a, they are to be considered as a different type of distorted austenite or distorted carbide.

In order to check the composition of these zones, chemical analyses were done on the EBSD zone.

Four significant points were chosen, as is shown in Figure 74.

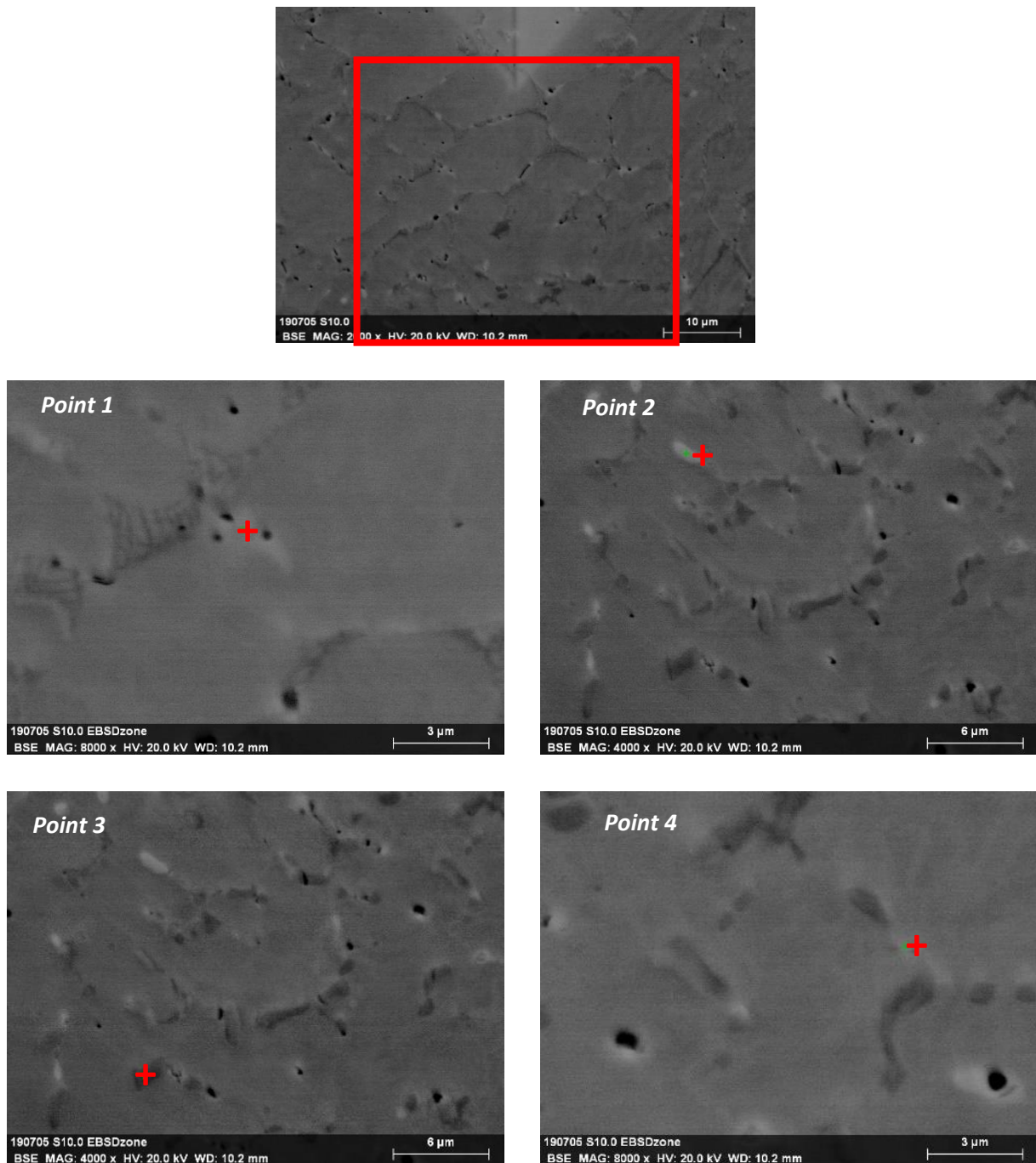


Figure 74: Investigation on the EBSD zone

Points 1 and 4 are in correspondence of a light halo in the carbides network, in the recognised zones by the EBSD discussed above. Point 2 is on a bright carbide while point 3 is on a dark carbide. The compositions of the microstructure in these points is shown in Figure 75.

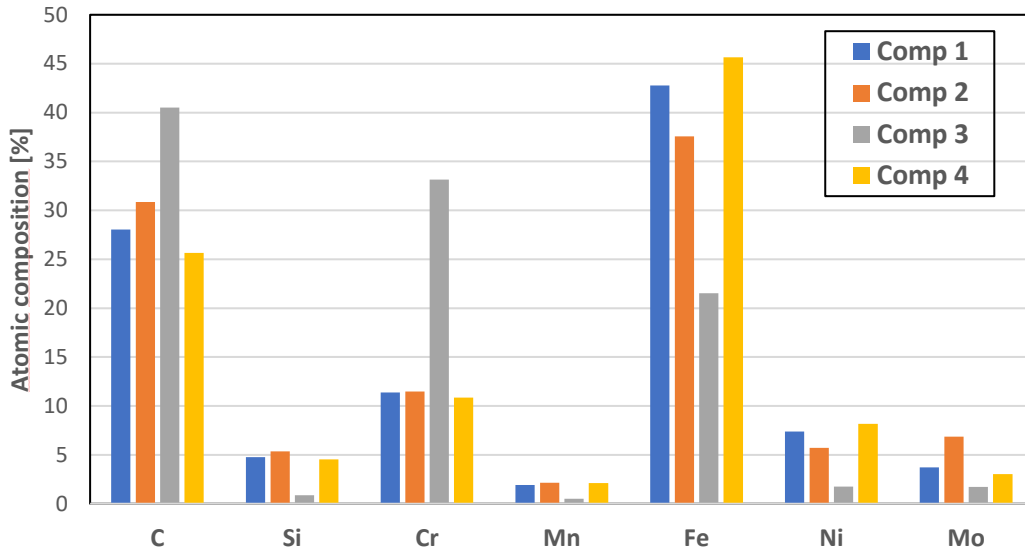


Figure 75: Compositions of the points on the EBSD zone

The point 3 in the dark carbide has a high quantity of Cr and C, more than the others points. Points 1, 2 and 4 represent the same phase, but the bright carbide of the point 2 is more define because its higher quantities of Cr and C. While light halo carbides of points 1 and 4 have not a clear nature and morphology. Due to this, a profile composition was done along a line passes through the carbide of the point 4 (Figure 76).

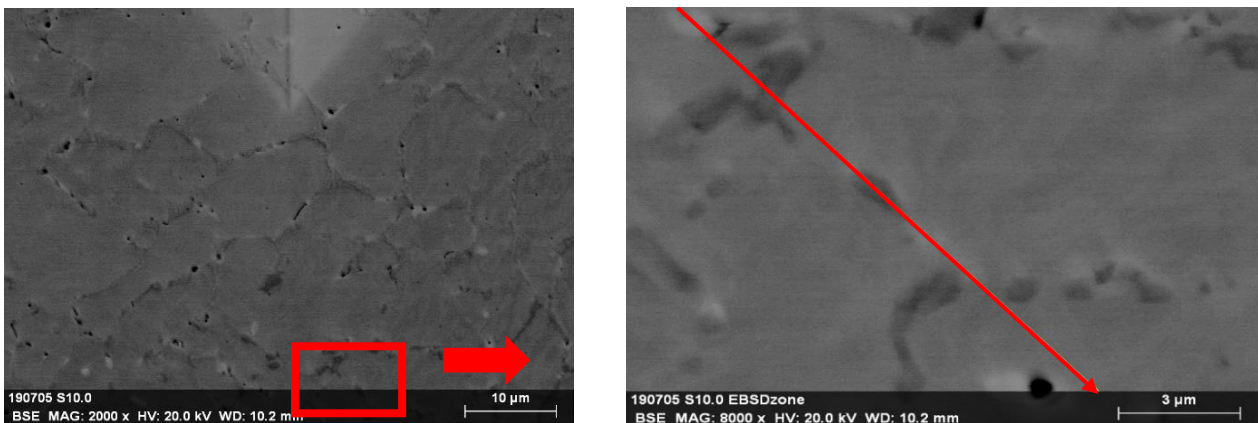


Figure 76: Chemical analyse on the EBSD zone

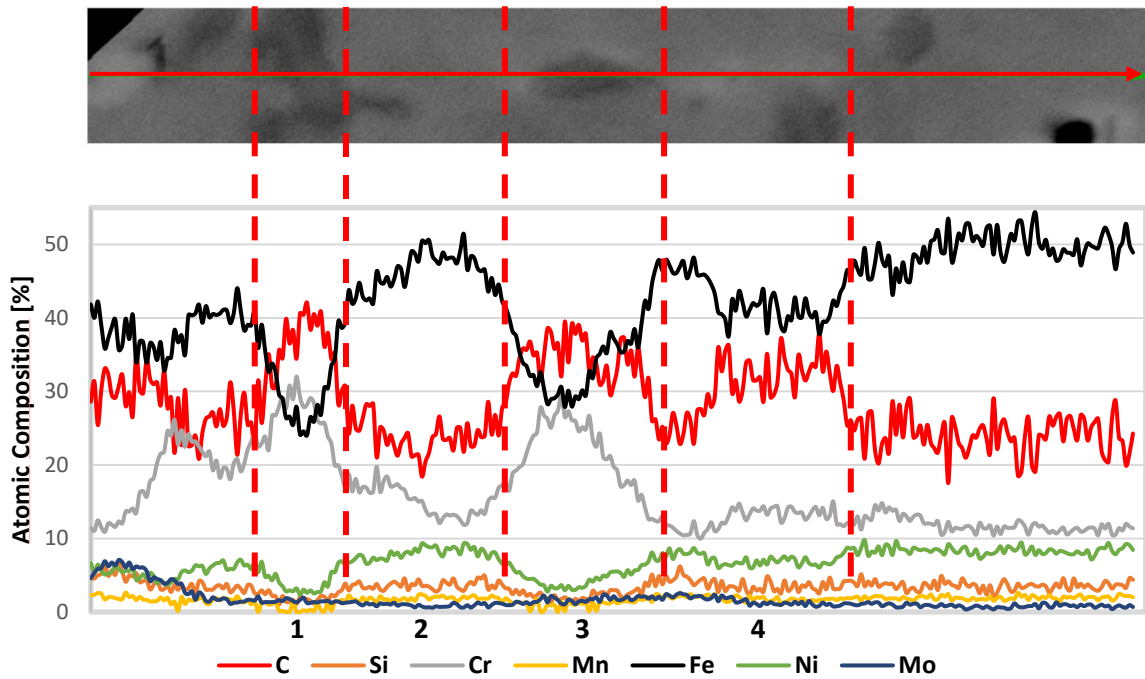


Figure 77: Profile compositions on the EBSD zone

Atomic Composition [%]								
Zone	C	Si	Cr	Mn	Fe	Ni	Mo	Phase
1	33,82	2,22	24,93	0,77	32,23	4,53	1,47	Cr carbide
2	23,97	3,67	15,17	1,83	46,39	7,99	0,96	Cell border/ Matrix
3	33,33	2,54	21,10	1,22	35,25	4,99	1,53	Cr carbide
4	30,28	3,75	12,69	1,85	42,73	7,09	1,57	Cell border
5	24,42	3,59	11,87	1,93	49,02	8,32	0,85	Matrix

Table 25: Compositions on the EBSD zone

The analyse in Figure 77 identify three main zone: 1 and 3 correspond to the dark carbide, in particular a Cr carbide, because the high amount of Cr and C. Zone 5 correspond to the matrix. Zone 4 correspondent to the bright area has an intermediate composition between the matrix and the carbide. Finally, the zone 2 present an intermediate composition between the matrix and the zone 4. Zone 2 has lower amount of Si and Mo than the zone 4.

As resume of these compositions, the elements show a composition gradient from the external to the internal of a cell, from the cell border to the matrix.

4.2.1.2 Thermal analysis

The pieces chosen for the DTA are the number 1 and 3 for the core, in order to compare the difference between the external and the internal laser track, and the number 3 of the surface in order to compare the difference between the core and the surface of the deposit (Figure 36).

In the next figures are shown the three heating (Figure 78) and cooling (Figure 79) curves.

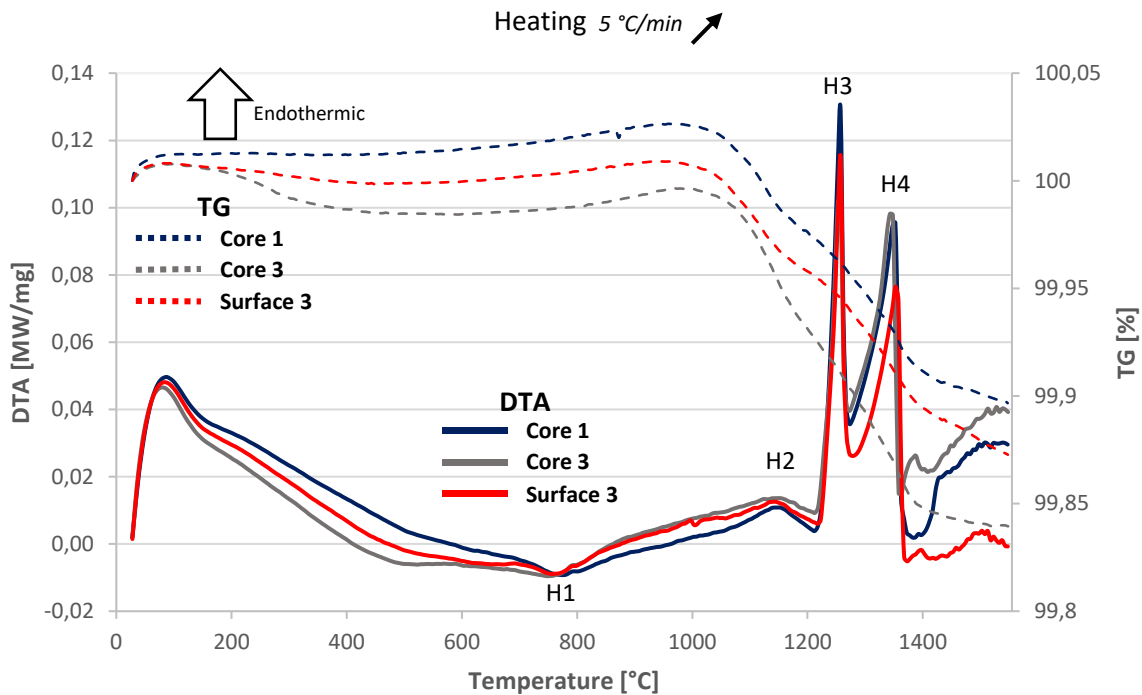


Figure 78: DTA and TG heating curves for S10.0

Peak	Start Temperature [°C]	Max/Min Temperature [°C]	End Temperature [°C]	Reaction or phase transformation
H1	?	?	?	Unknown
H2	1120	1150	1200	Reheating
H3	1210	1255	1270	Eutectic carbide fusion
H4	1280	1350	1370	Austenite fusion

Table 26: Principal heating peaks for S10.0

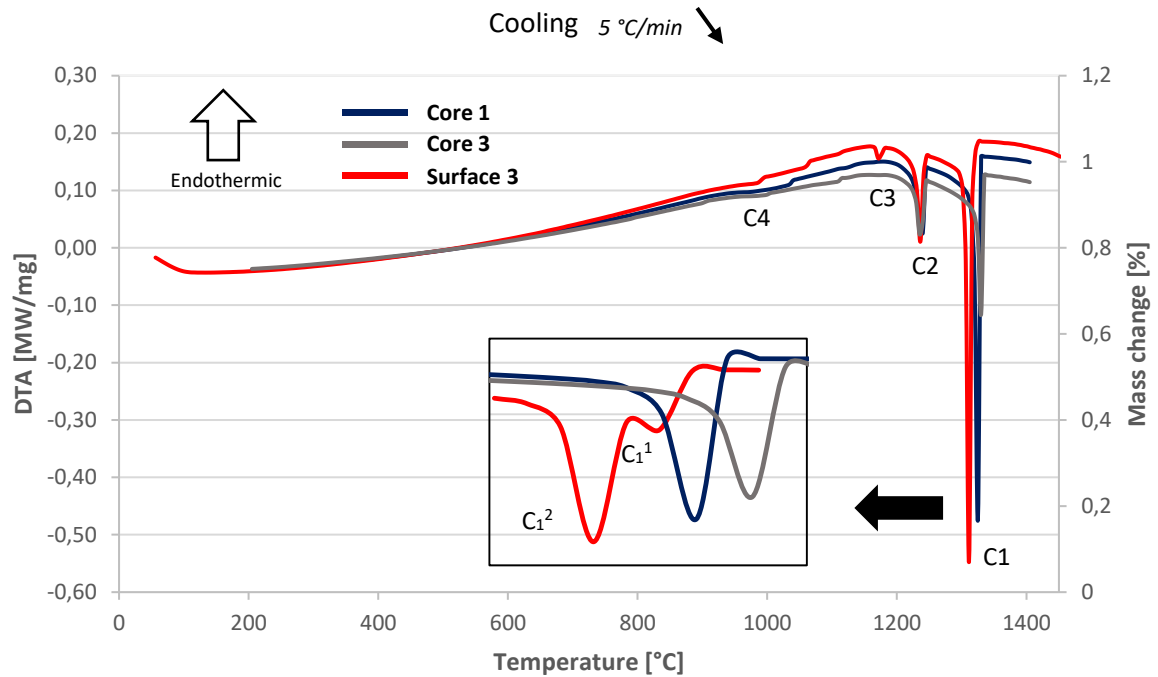


Figure 79: DTA cooling curves for S10.0

Peak	Start Temperature [°C]	Max/Min Temperature [°C]	End Temperature [°C]	Reaction or phase transformation
C1	1336	1323	1306	Peritectic reaction
C ₁ ¹ (Surface 3)	1327	1317	1312	Austenite solidification
C ₁ ² (Surface 3)	1312	1307	1302	δ ferrite solidification
C2	1256	1236	1216	M ₇ C ₃ solidification
C3 (Surface 3)	1191	1171	1161	M ₂ C solidification
C4	1150	?	890	Precipitation from peritectoid [47]

Table 27: Principal cooling peaks for S10.0

The three samples after DTA tests were observed with OM. ‘Core 1’ and ‘Core 3’ exhibit similar microstructure; only observations on ‘Core 1’ are shown (Figure 80, Figure 81).

Surface 3

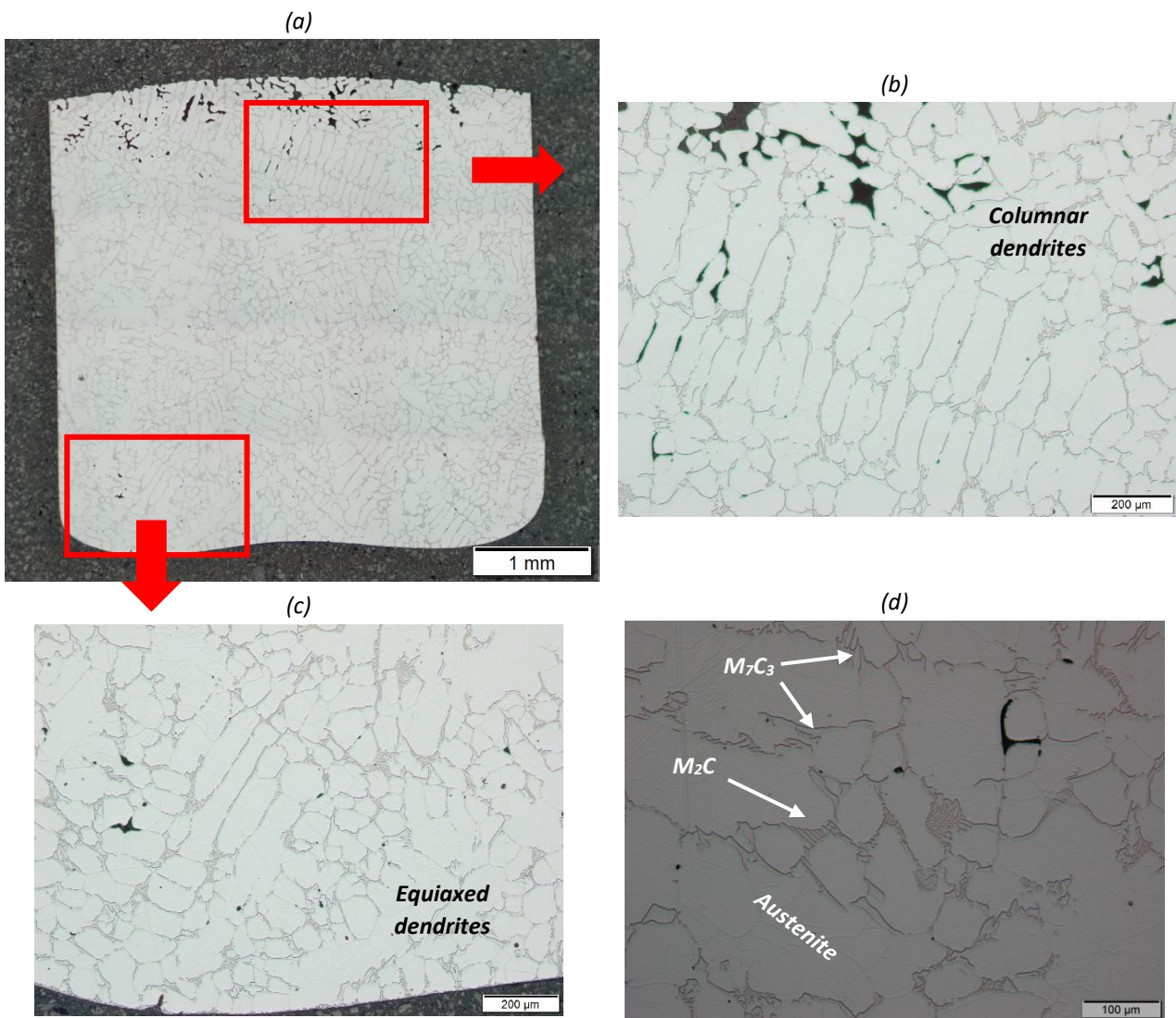


Figure 80: Optical Microscope observations on sample 'Surface 3' after DTA

In the sample 'Surface 3' after the DTA tests were formed in the top of the overview (Figure 80a-b) columnar and equiaxed dendrites. In Figure 80d the phases are highlighted. Two different types of carbides are present, M_7C_3 and M_2C .

Core 1

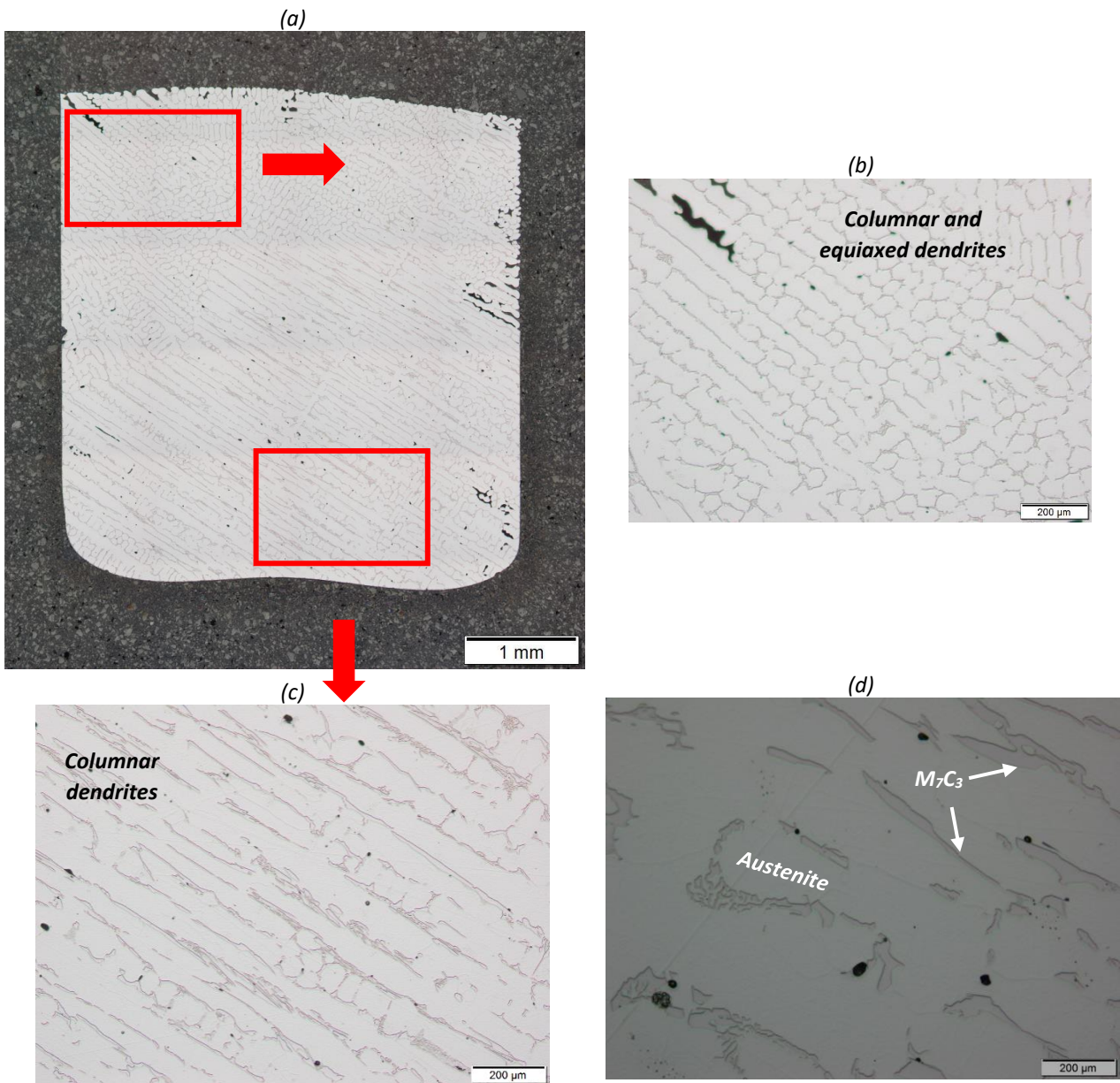


Figure 81: Optical Microscope observations on sample 'Core 1' after DTA

On the sample 'Core 1' is formed a columnar dendritic microstructure with different solidification direction (Figure 81b-c). The identify carbide is M_7C_3 type (Figure 81d).

On the sample S10.0 also a specific thermal analyse was performed to check the microstructure formed before the H3 peak of 1255 °C (Figure 78). In particular the heating was stopped at 1240 °C. The heating temperature was of 5°C/min, while the cooling temperature was of 20°/min in order to ‘freeze’ the microstructure formed at that peak. The parts of the sample S10.0 used for these tests was ‘Core 2’ (Figure 36).

In Figure 82 is shown the heating curve compared with a heating curve on the deposit up to 1550 °C previously showed, in particular the curve of ‘Surface 3’. As is visible in the zoom, the H3 peak present a non linear DTA heating curve because of the slope changing of the derivative of the DTA curve, due to the presence of different types of carbides.

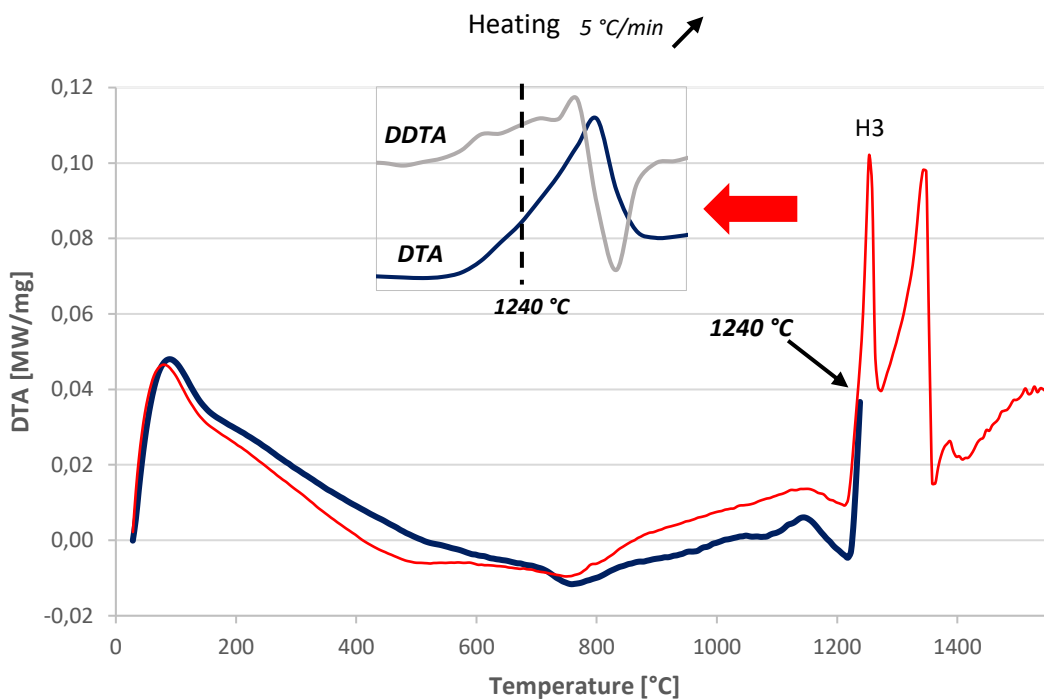


Figure 82: DTA heating curves up to peak H3

The sample after the DTA test was observed with Optical Microscope and Electron Microscope, and a cartography was performed in order to check the composition (Figure 83).

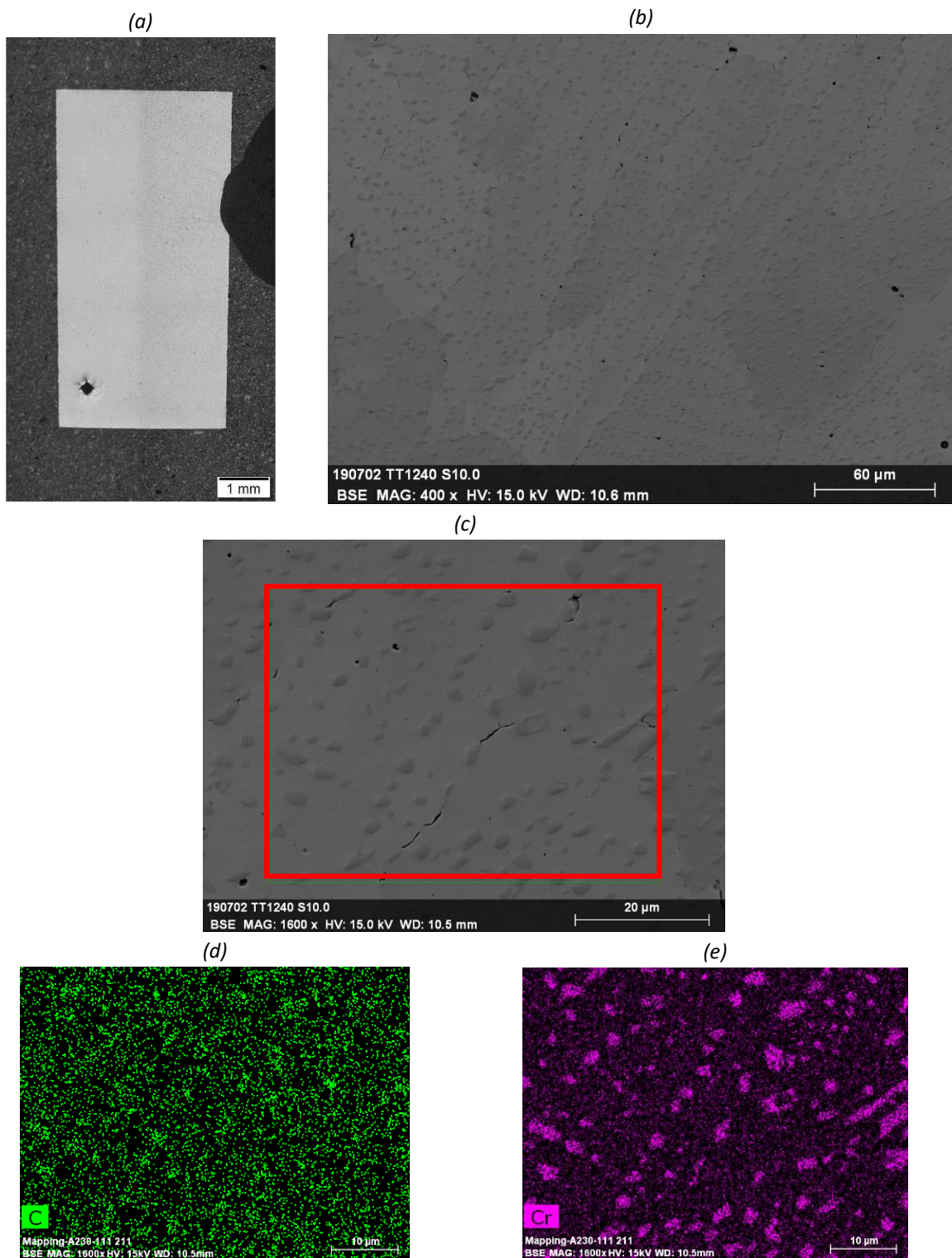


Figure 83: Observations on sample 'Core 2' after thermal analyse up to 1240 °C

In Figure 83a is visible an overview of the sample after the DTA. In Figure 83b-c is visible the globular morphology of the carbides. This microstructure is formed because of a high cooling rate. The main element identify by the cartography are Cr and C (Figure 83d-e) in correspondence of the carbides in Figure 83c.

4.2.1.3 Macrohardness

The macro-hardness test was done on the left part of the sample S10.0 (Figure 84) The grid points have a distance one from the other of 1 mm. The first line on the bottom was done on the substrate of SS316L, in order to have a comparison with the deposit. The two points in the upper right corner and the two points near the top of the deposit were not considered for the results.

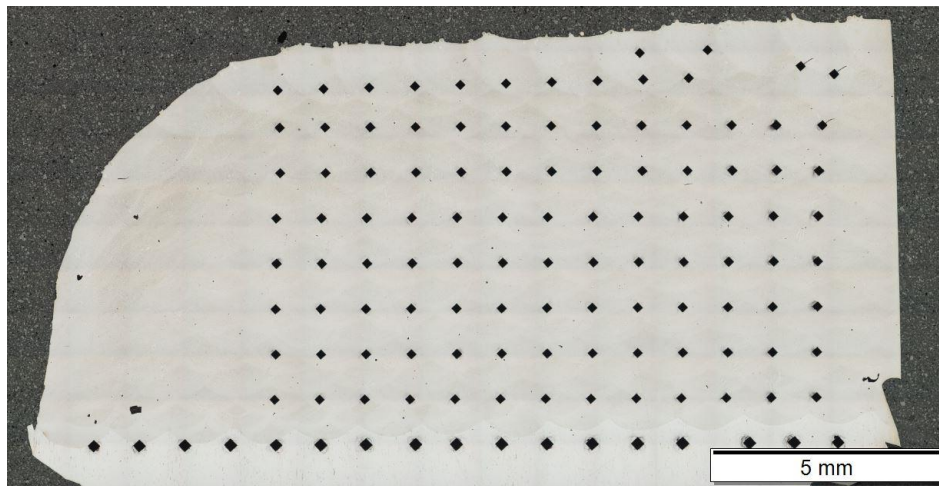


Figure 84: Macrohardness grid on left section of S10.0

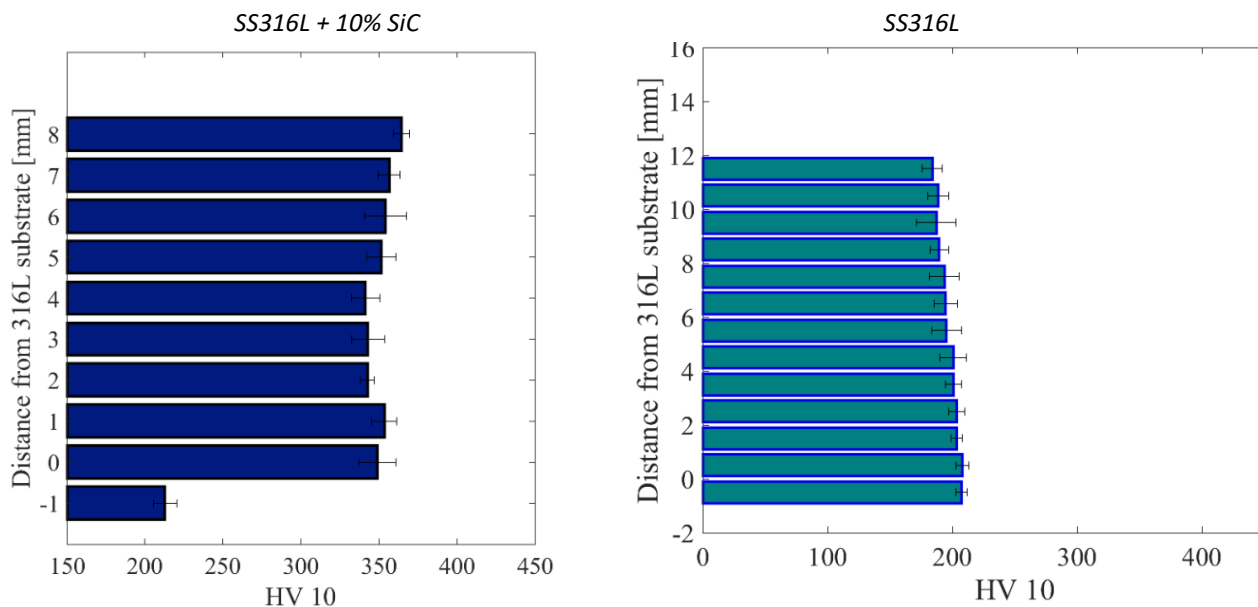


Figure 85: Macrohardness: SS316L+10%SiC vs SS316L

In Figure 85a are present the average hardness for each line on the macro grid in Figure 84. The trend is linear and the average hardness for all the line (except the line -1 corresponding to the substrate) is of 348 HV. The standard deviation has not big values range. The hardness is visible better in comparison with the cladded SS316L (200 HV) (Figure 85b).

4.2.2 Cladded deposit SS316L + 20% SiC

In this section, observations on the cladded deposit of SS316L + 20% SiC are reported. Samples S20.0 and S20.06 were produced with original powders, while sample S20.07 was produced with milled powders, as explained in chapter 3.3.

4.2.2.1 Microscope observations

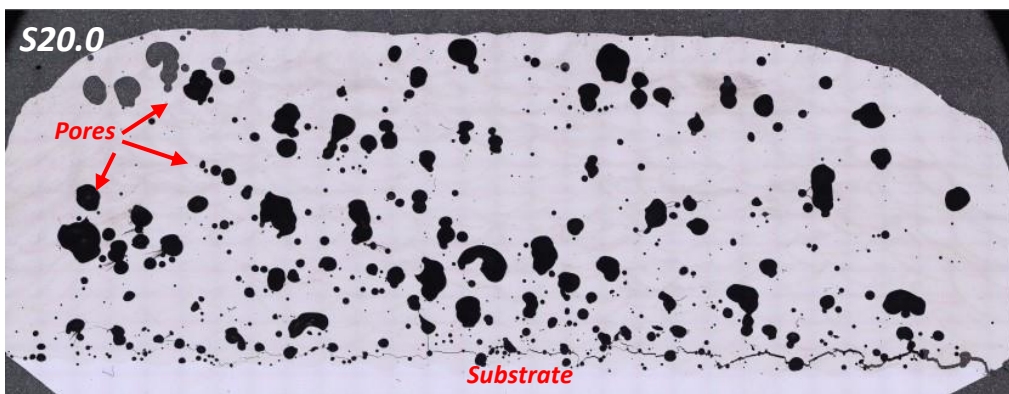


Figure 86: Overview of the sample S20.0

The sample S20.0 presents a lot of big porosities and also a crack between the substrate and the deposit (Figure 86).

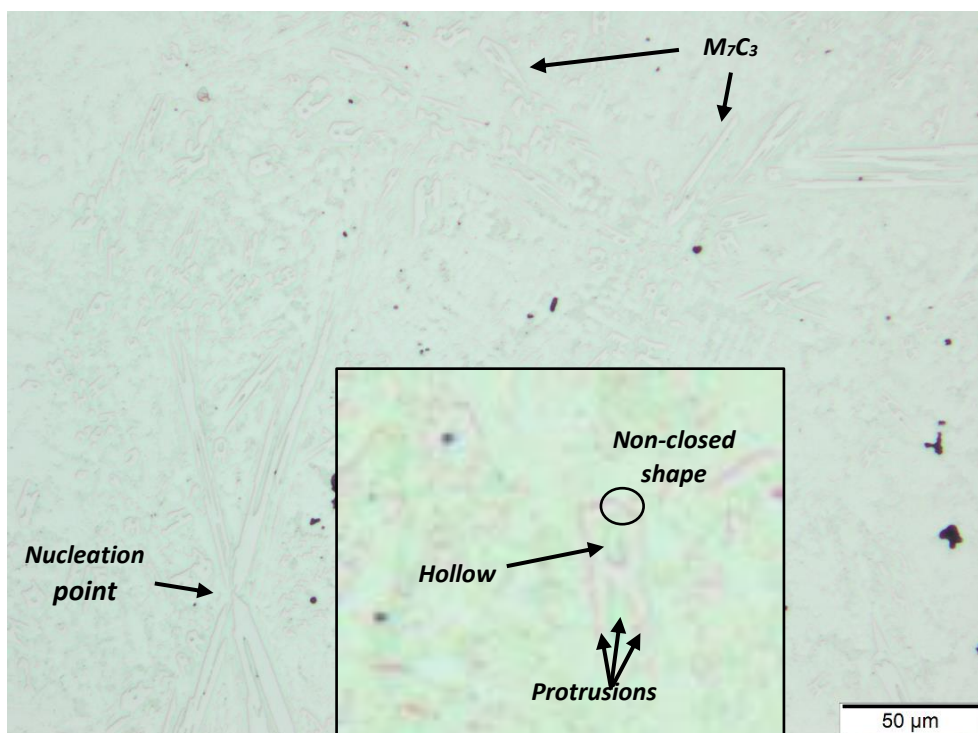


Figure 87: Optical microscopy observation on sample S20.0

A general view of the microstructure by Optical Microscope is shown in Figure 87. The carbides are big, with a size up to more than 50 μm . The morphology of them is like M_7C_3 type [36]. On the bottom left of the figure is visible a nucleation zone from where carbides start to grow, while the most of other carbides are randomly arranged. In the box is visible a focus on M_7C_3 carbides. They present a non-closed hollow-hexagon shape, with hollows and protrusions.

With SEM some investigation on the microstructure were done, in particular some chemical analyses in order to check the nature of carbides.

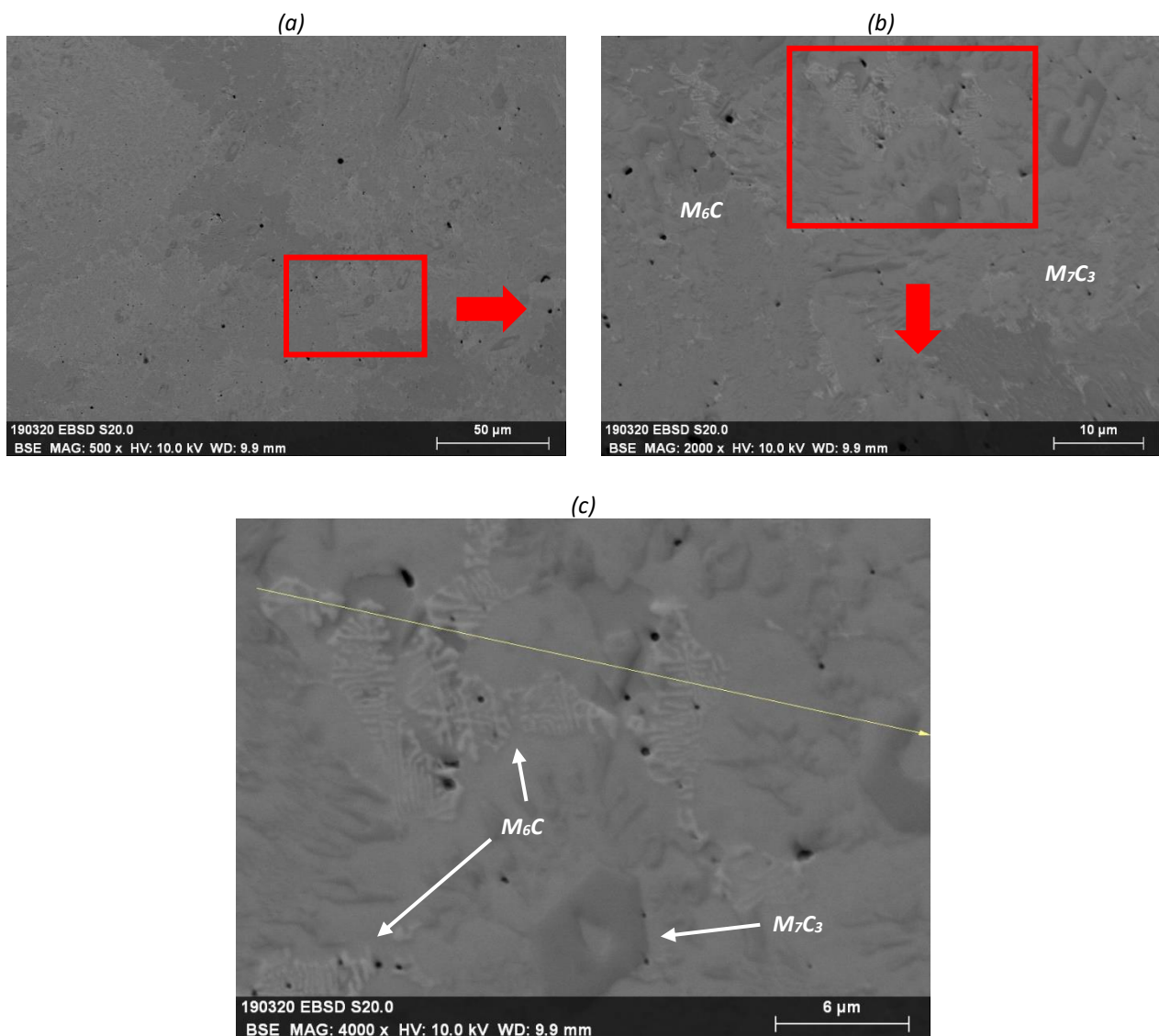


Figure 88: SEM observations on sample S20.0

In Figure 88b-c are highlighted the two different types of carbides that characterized the SS316L +20% SiC cladded deposit microstructure. There are M_7C_3 , discussed above, and also M_6C [37]. The first type is dark in SEM micrograph and the second is bright. Eutectic M_6C morphology is influenced

by the presence of a central platelet from which arises secondary platelets separated by austenite. These secondary platelets are thicker at the end, interrupting the continuity of the austenite.

In order to check the composition of these carbides, some chemical analyses were done.

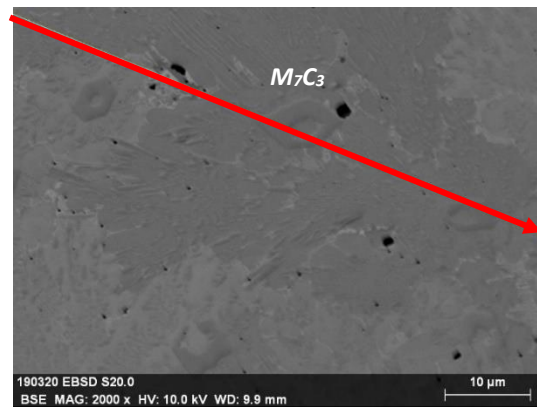


Figure 89: Chemical analyse 1 on sample S20.0

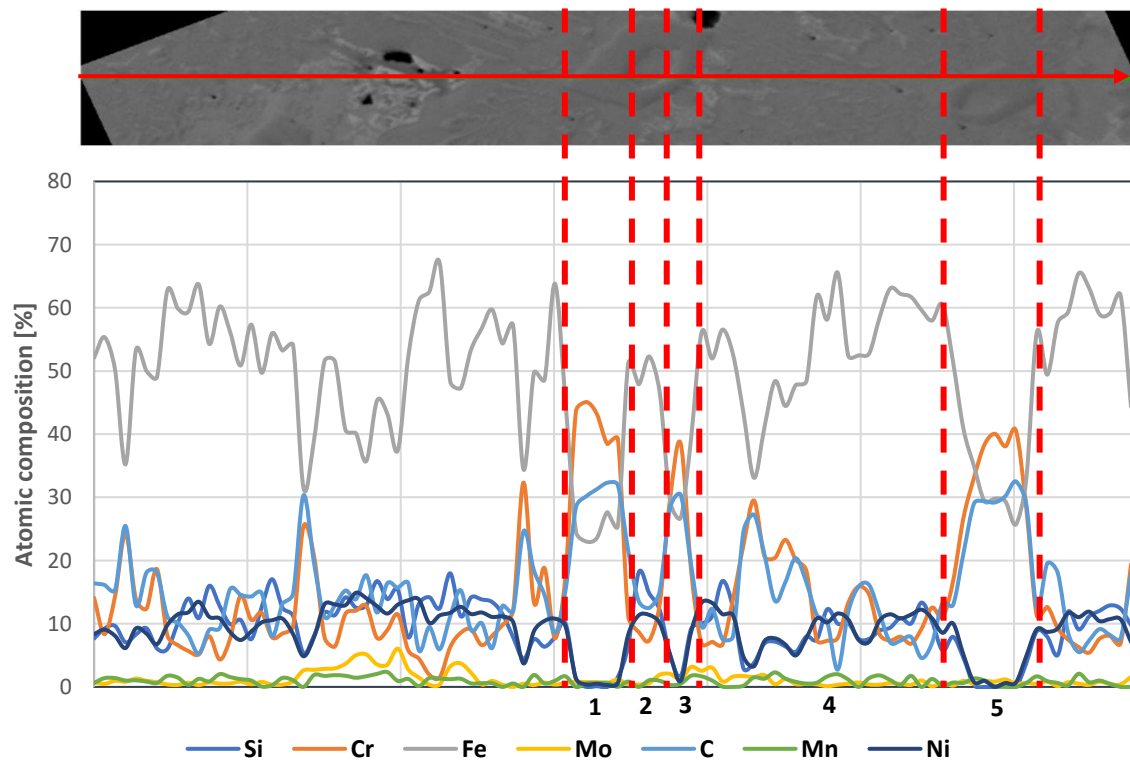


Figure 90: Composition profile 1 on sample S20.0

Atomic Composition [%]

Zone	Si	Cr	Fe	Mo	C	Mn	Ni	Phase
1	2,79	34,04	31,54	0,73	27,26	0,62	3,01	M ₇ C ₃
2	12,91	10,08	49,51	0,83	15,69	0,72	10,28	Matrix
3	7,63	21,33	39,64	2,18	20,56	1,04	7,62	M ₇ C ₃
4	8,40	14,32	53,51	0,71	13,09	1,00	8,98	Matrix
5	3,39	28,58	37,99	0,71	24,55	0,70	4,09	M ₇ C ₃

Table 28: Atomic Compositions 1 [%] in sample S20.0

Composition of zone 1, 3 and 5 where the line passes through the M₇C₃ shows a high quantity of Cr and C. The zone 4 has also a high quantity of Mo, due to the neighbouring of a bright carbide (Table 28).

Another chemical analyse was done on the M₆C bright carbide (Figure 91). It exhibits high values of Mo and C (Table 29).

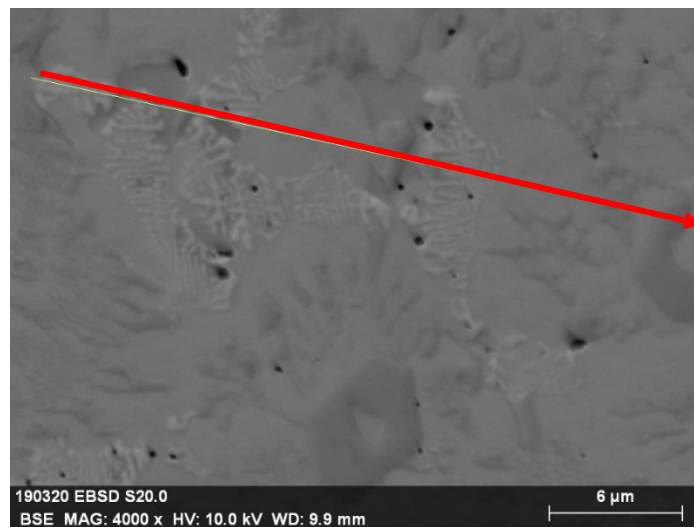


Figure 91: Chemical analyse 2 in the sample S20.0

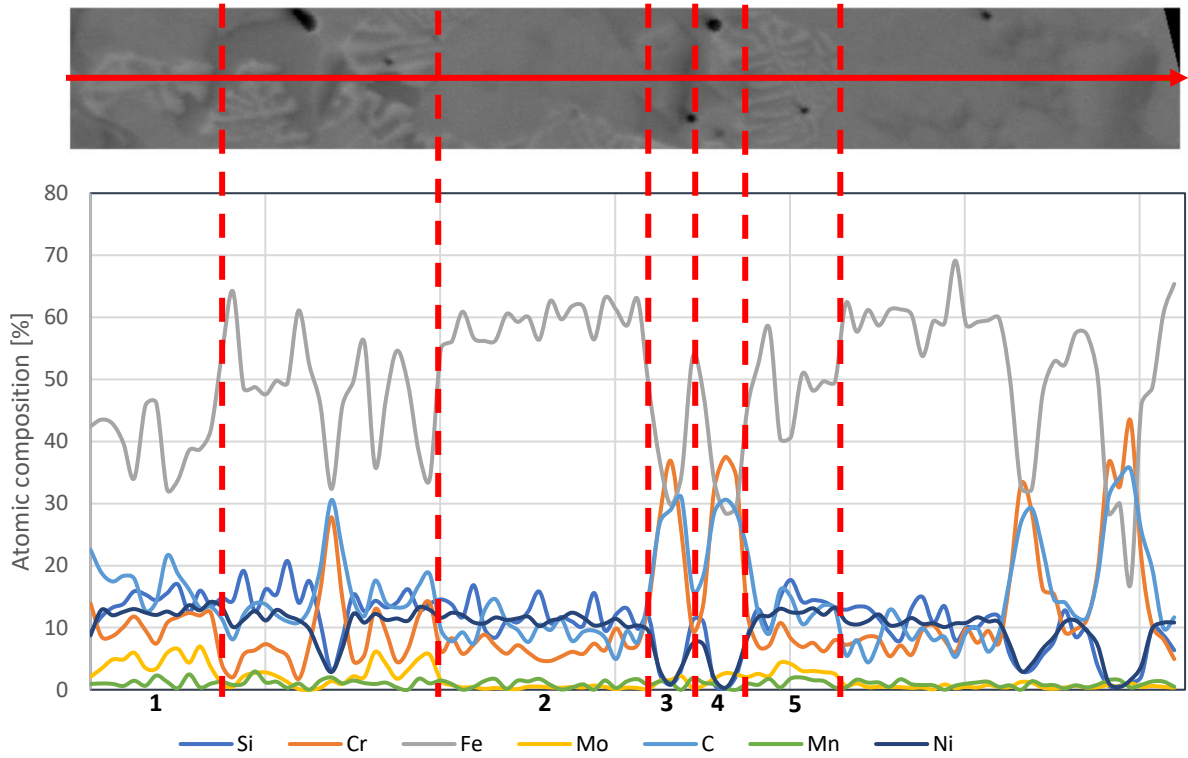


Figure 92: Composition profile 2 on sample S20.0

Atomic composition [%]

Zone	Si	Cr	Fe	Mo	C	Mn	Ni	Phase
1	14,43	9,39	43,12	3,94	15,77	1,08	12,23	M ₆ C
2	11,94	6,71	59,47	0,36	9,38	0,89	11,21	Matrix
3	5,91	22,70	40,73	1,11	23,62	1,02	4,89	M ₇ C ₃
4	6,50	20,69	42,13	2,06	21,45	0,82	6,31	M ₇ C ₃
5	14,51	7,83	48,84	2,93	12,26	1,12	12,48	M ₆ C

Table 29: Atomic composition 2 [%] in the sample S20.0

In addition to the microscopy observation, the porosities were analysed with ‘Stream Analyse Software’ (chapter 3.4.2). With this software, the pores developing in the section was investigated.

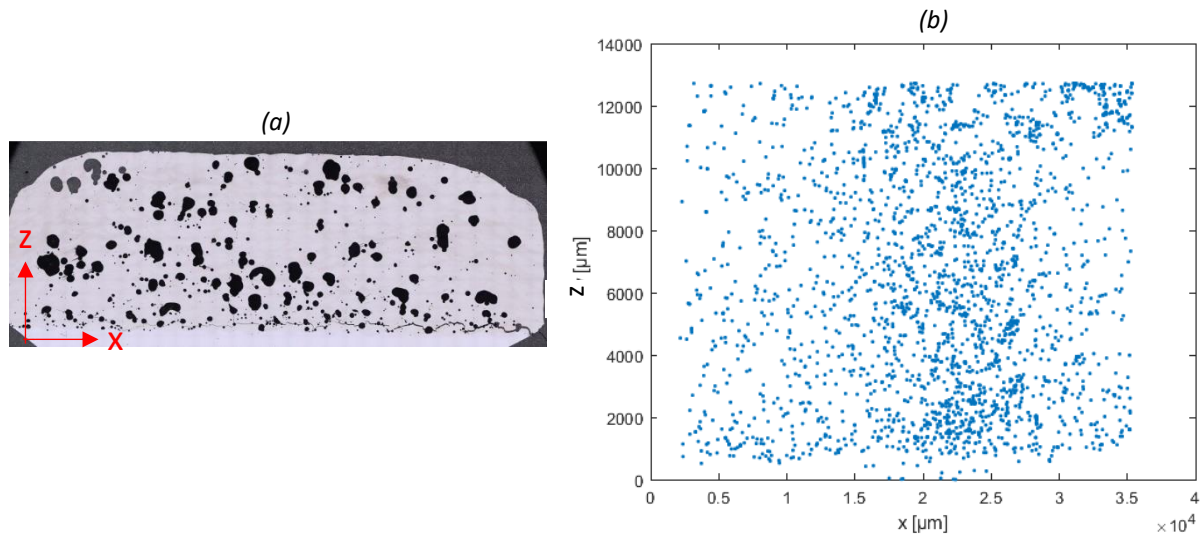


Figure 93: 2D pores distribution in the sample S20.0

In Figure 93b is reported 2D pores distribution in the section. The major density is on the centre of the section.

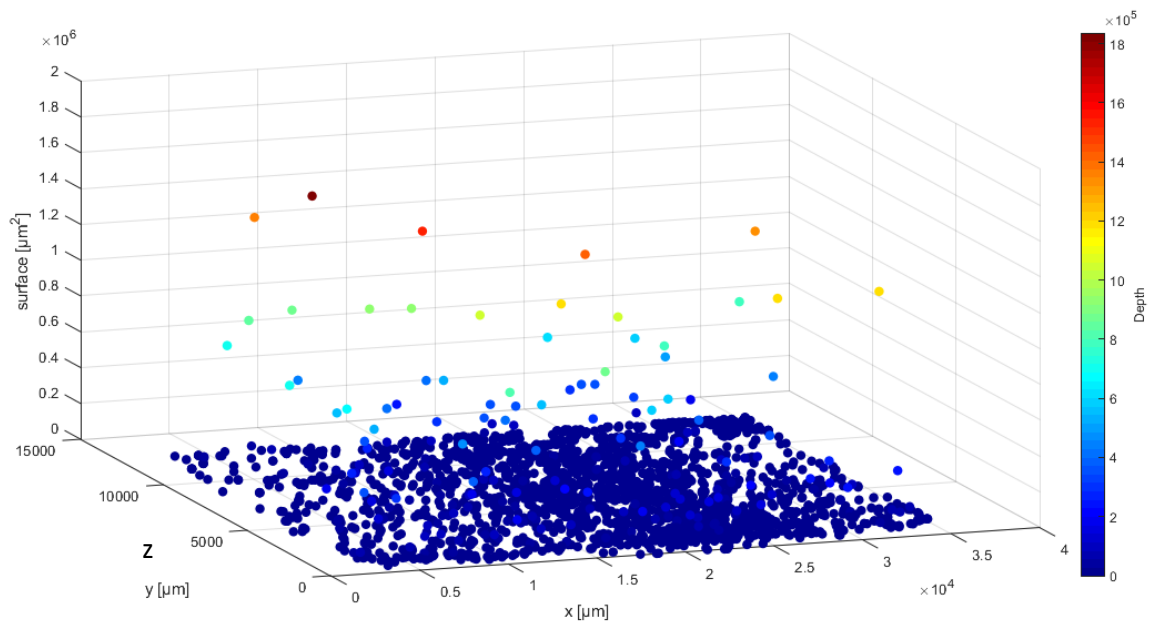


Figure 94: 3D pores distribution in the sample S20.0

More significantly is the Figure 94 where 3D pores distribution is reported in function of x and z axis, and the surface area. It is possible to notice that the most of pores have small dimensions, only few pores have big dimensions.

To understand if there is correlation between pores dimensions and distance from the substrate, the section was divided in 4 zones (Figure 95) and the amount of pores for each zone was checked. In particular pores were divided in 4 dimension surface groups.

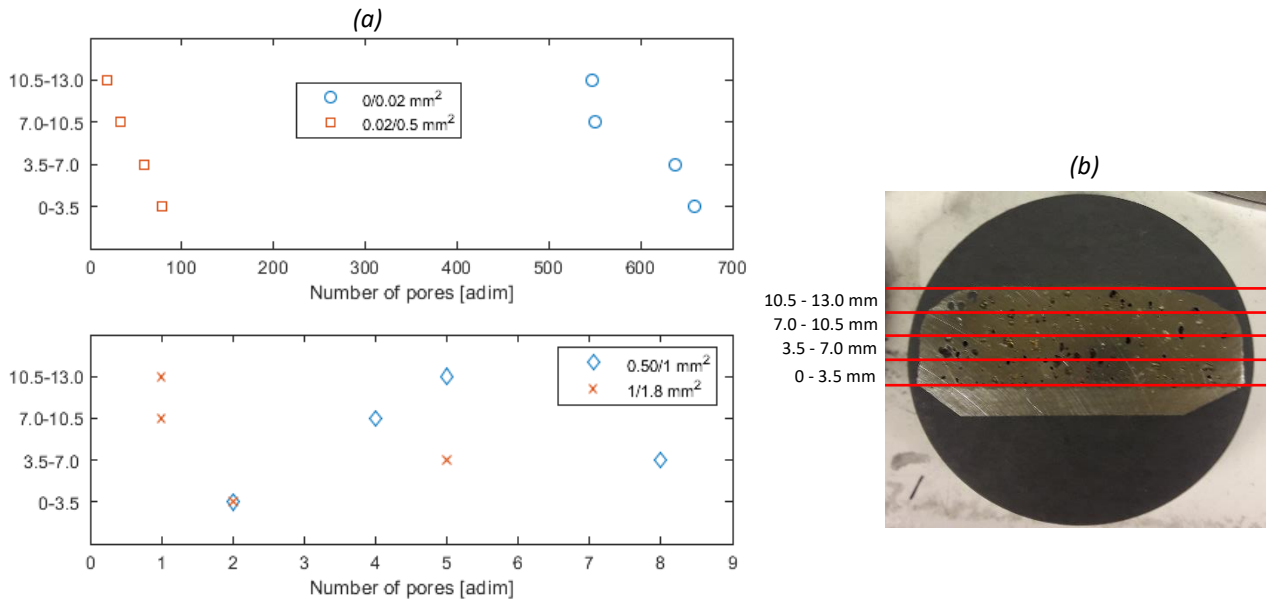


Figure 95: Dimensional evolution of the pores in the sample S20.0

The smaller pores (0/0.02 – 0.02/0.5 mm²) present a linear trend of distribution from bottom to top of the section, in particular the number of them decrease from bottom to top as is visible in the first graph of Figure 95a. Bigger pores have not a linear distribution.

The other samples with the 20% of SiC were observed by Optical Microscope. First the sample S20.06 is shown.

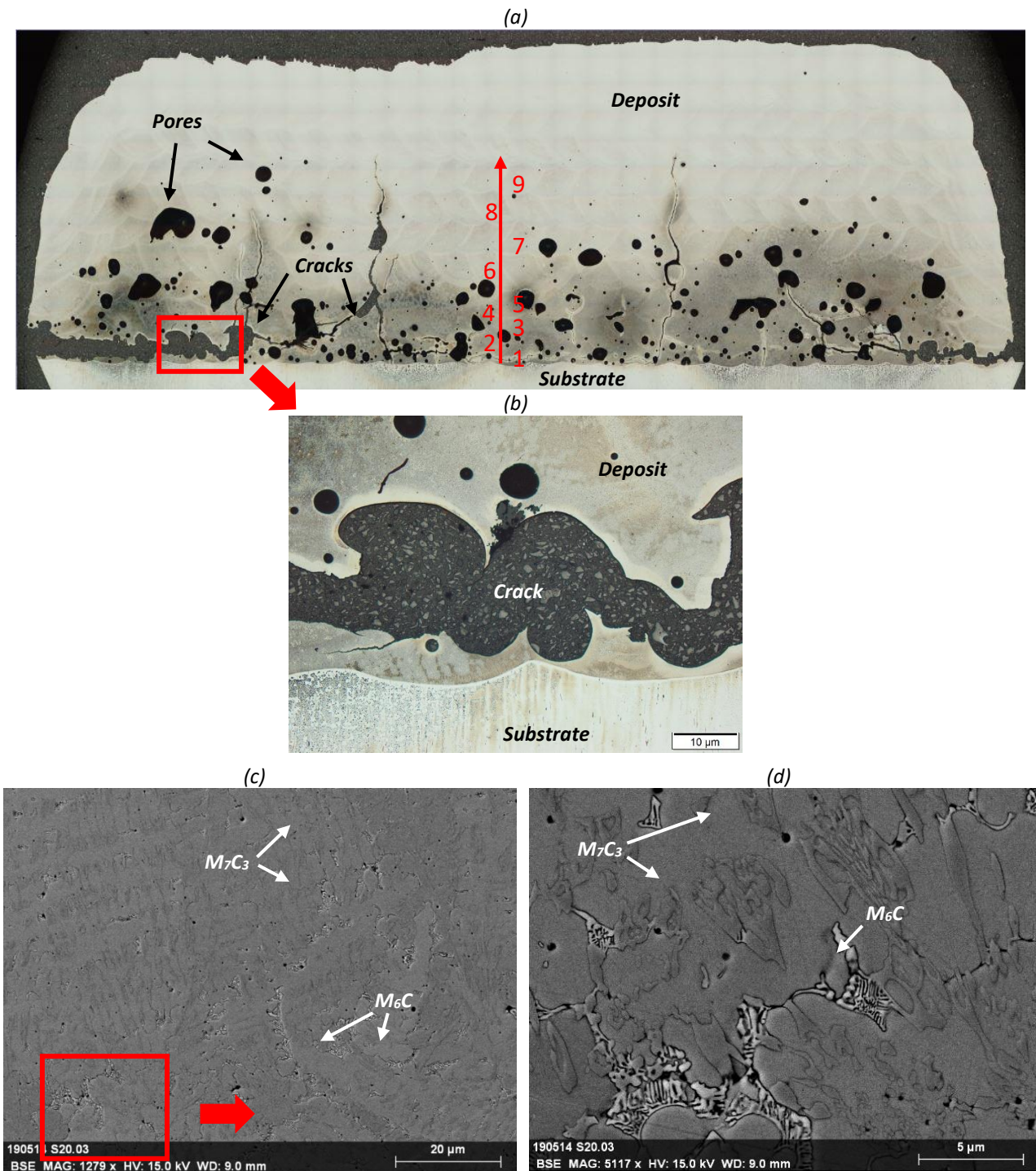


Figure 96: Optical microscope observations on the sample S20.06

The overview of the sample S20.06 (Figure 96a) allows to observe the presence of pores only on the bottom part of the sample, in particular in the first 9 layers of the deposit and not in the whole section. Cracks are present both in horizontally and vertically direction. A focus on the boundary between the substrate and the deposit shows a good interaction between them (Figure 96b).

In Figure 96c-d is visible the microstructure of this sample: M_6C (bright) and M_7C_3 (dark) are present, as in the sample S20.0.

Afterwards, for the cladding of sample S20.07, a pre-mix of SS316L + 20% SiC milled powders were used.

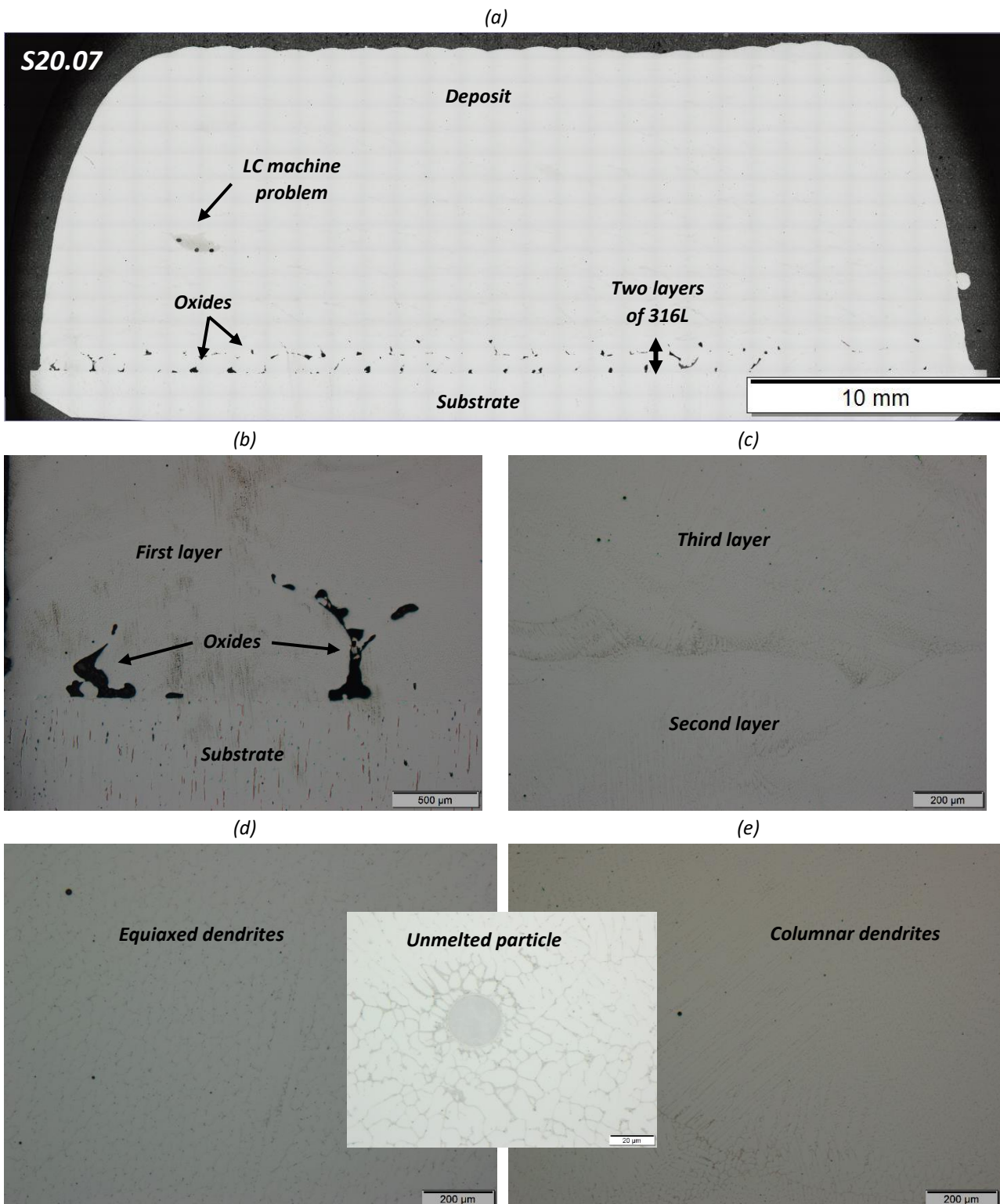


Figure 97: Optical microscopy observations on the sample S20.07

An overview of the sample S20.07 is shown in [Figure 97a](#). The first two layers are composed by SS316L, in order to avoid fracture between substrate and deposit. After these layers, the deposit is composed by milled powders. The difference with the previous samples of SS316L + 20% SiC is the absence of porosity. A defect is visible in [Figure 97a](#), but it is not a problem of powders.

The substrate does not present the laser track path ([Figure 97b](#)). There are also the presence of oxides in the first two SS316L layers. While the second SS316L layer and the third layer of SS316L + 20%SiC have a good interaction without big porosities or cracks ([Figure 97c](#)).

The microstructure is characterized by columnar and equiaxed dendrites ([Figure 97d-e](#)).

The unmelted particle highlighted in the box is characterized by a thin layer that isolates it from the matrix, and where the growth of carbides start. It can be a SiC particle or another type of particle that had contaminated the pre-mix of powders.

5 DISCUSSION

5.1 Role of oxygen contamination

The characteristics of the raw material (in particular the SiC powders) have a huge impact on the final deposit. These particles have been chosen in the market because of their morphology, adapted for the laser cladding. The 5% of oxygen reported in the datasheet (Annex 2) was supposed to be a process defect, in the form of SiO₂. Instead, it corresponds to actual air bubbles trapped into porosities.

The presence of oxygen was detected comparing thermal analysis results and microscope observations on powders. In particular, as shown in chapter 4.1.1.4, the DTA heating curve of the original SS316L + 20% SiC powder exhibits an oxidation peak at 1130 °C, and SiC powders after milling show fractured particles that contain cavities (Figure 54).

The aim of the milling procedure was to induce fractures and deformation of SiC powders in order to release the trapped oxygen. Different milling procedures were tested, considering previous works on powder milling preparation [53]. In particular, SiC and SS316L + 20%SiC powders were milled with different milling time and balls-to-powder weight ratios (chapter 4.1.2). In this study, powder preparation by mechanical alloying (MA) through ball milling had an important role on the final properties of the cladded deposit, because the repeated deformation, fracturing and cold welding resulted in a change of morphology, size and microstructure of powders. Furthermore, ball milling increases cost and possibly lead times. SiC powders were milled separately or with SS316L powders in order to establish the best procedure. The separate milling was not successful, and it did not lead to any evident changes, in spite of the many different parameters tested. Instead, the milling on the SS316L + 20% SiC with 1:5 balls to powders weight ratio lead to beneficial effects.

DTA analysis were used in order to verify the effectiveness of the milling procedures. Figure 98 shows that the heating curves are all very similar, presenting the same peaks, except for the range 1040 – 1200 °C shown in Figure 99.

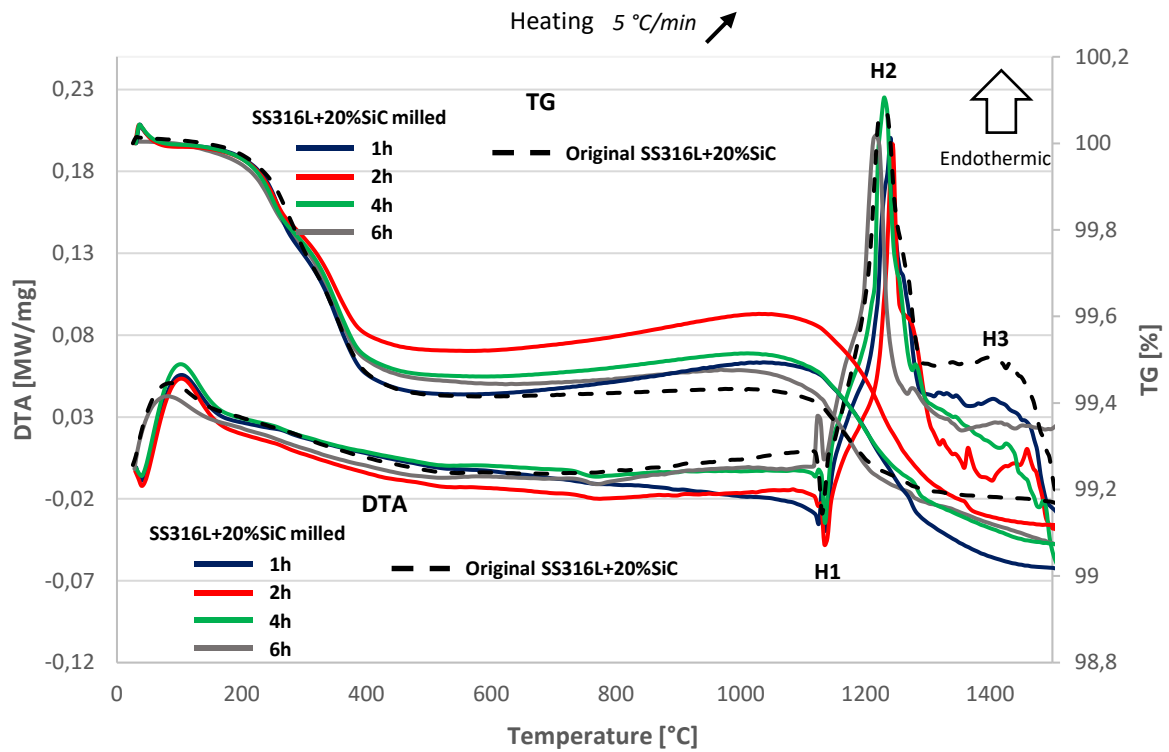


Figure 98: DTA & TG heating curves for SS316L+20%SiC powders

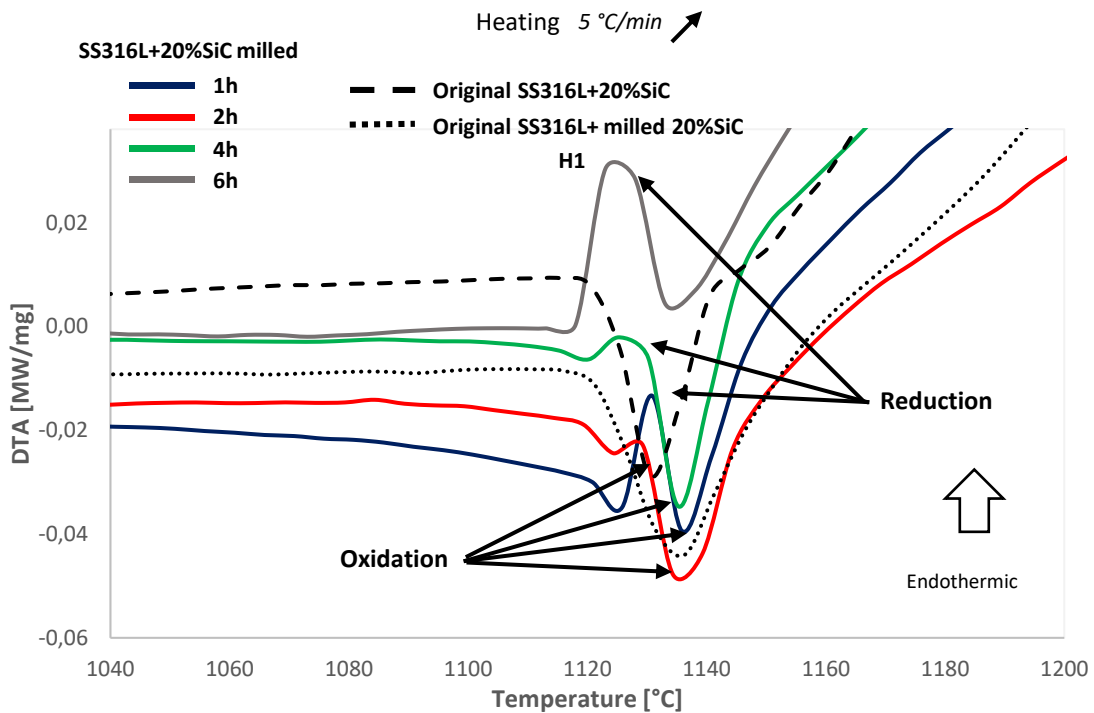


Figure 99: Focus on DTA H1 heating peak

Two main reactions characterize the peak H1 (Figure 99). It is possible to observe that exothermic peaks referred to oxidation are present in every condition, except after 6 hours milling. Endothermic peaks referred to carbothermal reduction is present from 1 hour milling. The behaviour of powders

in this range temperature is not completely clear, because it was not possible to check the reactions product. Nevertheless, there is a clear evolution through the difference milling steps.

Oxidation is due to the presence of oxygen and oxidation-sensitive elements such as Si present in the SiC powders. The oxidation leads to the formation of SiO₂ and CO₂, according the following reaction:



The exothermic oxidation peak of curves of SS316L + 20% SiC milled powders is interrupted by an endothermic peak due to a carbothermal reduction. This reaction is due to the presence of C in SiC powders and it leads to the reduction of the less stable oxide. According to the Ellingham diagram (Figure 100) [54] and the study of R. Calderon [55], at about 1130 °C, C reduce the Cr₂O₃ presents on the surface of SS316L particles, due to its lower stability compared to SiO₂. The result of this reaction is the formation of CO and Cr₃C₂, according to the following equation:

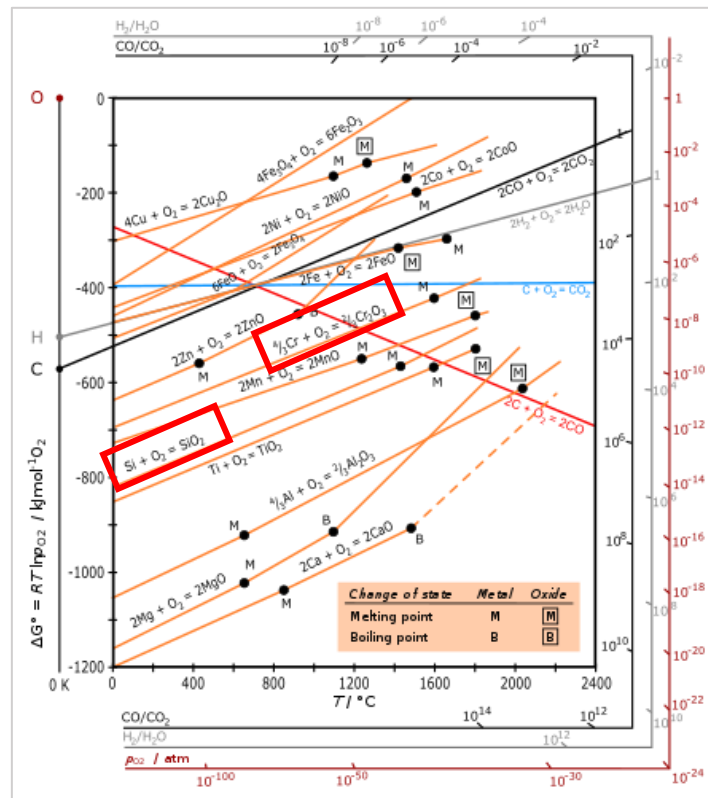
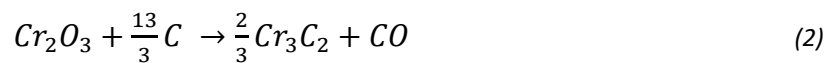


Figure 100: Ellingham diagram [54]

The comparison between TG and DTA is a good method to understand the thermal behaviour of powders, since it shows the mass change during the thermal test. All the TG curves (Figure 98) show a first decrease from the beginning of the test up to 400°C due to the escape of a large part of trapped

air (Figure 101), and a second decrease starting from peak H1 due to the beginning of austenite fusion with a consequent decrease in mass, since the remaining air escapes.

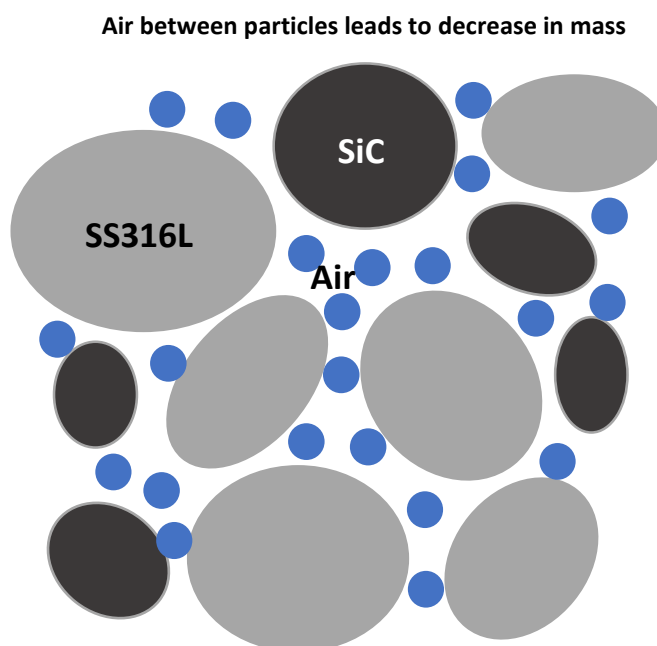


Figure 101: Air between powders

The TG curve for the original powders shows a plateau in the range between 400 °C and 1135 °C because there is no reaction between SiC and SS316L, and only oxidation occurs at high temperature. Meanwhile, the milling leads to a reaction between SiC, SS316L and oxygen (present in the undeformed SiC particles) with the formation of Cr_2C_3 and/or SiO_x . In fact, there is an increase in mass in the range 400 °C – 1135 °C for the intermediate milling steps. Finally, the TG curve after the 6 hours milling exhibits a lower increase of the mass than the previous stage, but it is not possible to quantitatively compare with the others curves since a different ‘blanc’ as reference was used for the DTA test.

The different milling steps and the relative DTA test were performed in order to choose the best milling result comparing DTA H1 peaks and microscope observations (*chapter 4.1.2*) on powders. The curve of the original SS316L + 20% milled SiC powders exhibit the oxidation peak, while curves of milled mixture of SS316L + 20% SiC powders exhibit a complex peak. After 1 hour of milling the main reaction is the carbothermal reduction. In fact, SiC powders start to deform and to fracture, so the oxygen is released. The surface of some SS316L particles is covered by a discontinuous layer of SiC due to the continuous friction between the powders that occurs during the milling. The resulting granulometry is homogeneous (Figure 55). After 2 hours of milling the main reaction is the oxidation, although the number of SiC fractured is higher than for the previous stage. Some of these

fractured particles are completely smashed and the number of small scraps is increased (Figure 56). In the first 2 hours of milling, the presence of a large population of ‘small’ or ‘big’ particles could lead to respectively a predominant oxidation or reduction. This is due to the different morphology of the porosities. Small SiC particles are more difficult to deform and they have smaller porosities than the larger SiC particles. After 4 hours the carbothermal reduction peak is higher than the previous milling time, but oxidation is still the main reaction. There are several SS316L deformed particles covered by SiC, and the granulometry is visibly heterogeneous because of the high amount of SiC scraps (Figure 57). Finally, after 6 hours milling, the main reaction is the carbothermal reduction and there is no oxidation peak. The granulometry of the powders presents both very small particles (< 20 μm) and big particles (500 μm) (Figure 58).

The aim of the milling was to deform and to fracture SiC powders, but keeping a homogeneous granulometry, as required by the laser cladding process. Considering the DTA/TG results, microscopy observations and considering an optimization of the process time, the best result in these terms was the milled mix SS316L + 20% SiC powders after 1 hour of milling. They were used to produce the sample S20.07.

The reactions just described do not occur during the laser cladding deposition, but they were used as way to evaluate the presence of free air and porosities in the SiC powders.

5.2 Optimization of cladded deposit

The parameters governing the cladding process must be studied with particular attention. These parameters are relevant in determining the clad profile, fusion between layers, homogeneity between layers, dilution of the cladding metal, surface finish, cracking due to thermal stresses, defect such as porosity, etc.

The cladded sample of SS316L + 10% SiC led to good result in terms of production because it did not present porosity or cracks, as shown in chapter 3.3.1. The reinforcements were completely dissolved.

The first deposit S20.0 was produced with the same parameters as the S10.0 that are present in literature (chapter 3.3) [29]. After the fabrication, it was noticed cracks were noticed only in the bottom part, between the deposit and the substrate, while the surface on the top appeared in a good state (Figure 33). When the sample was cut, many porosities were noticed. The main problem that leads to the internal porosity is the presence of cavities inside SiC particles that contain oxygen, as explained in chapter 5.1. When SiC particles dissolve in the molten metal, the oxygen is released and then gets trapped in the melt pool, leaving some empty zones on the deposit that are formed during the cooling. This results in the presence of cracks on the external sides since the deposit is not completely compact. There are some zones of the deposit structure with a high concentration of stresses. Based on mechanical behaviour of a solid, the result of high stress over the limit of the material resistance is its fracture.

As explained in chapter 4.2.1.1, there is an evolution of the small pores (in dimensions) from the bottom to the top of the deposit. This is due to the temperature gradient in the deposit. In fact, the cold substrate and the firsts hot layers of the deposit cause a high temperature gradient that leads to a high solidification rate in the bottom. As consequence, many pores are formed because the oxygen has not enough time to escape from the melt pool by density differences. On the contrary, between the top part and the bottom part of the deposit the temperature gradient is lower and this leads to a lower solidification rate. Because of this, a larger quantity of oxygen has enough time to escape from the melt pool. The big pores are found a randomly throughout the deposit. They are probably due to an agglomeration of many small porosities that have not enough time to 'exit' from the deposit during the solidification (Figure 102).

Considering these results, in order to improve the deposit quality, the laser cladding parameters were changed (chapter 3.3). In particular, for the fabrication of the sample S20.06 the power was increased and the scanning speed was decreased, in order to give enough time to the solidification of the deposit, to let the oxygen escapes. The cracks on the bottom part are still present,

but there is a significant decrease of the porosities. In fact they are present only in the first 9 layers in a total of 19 layers (Figure 102). This is still due to the decreasing temperature gradient between the substrate and the bottom part of the deposit.

Finally, with the pre-milled mix of powders, the deposit S20.07 did not show external cracks and internal porosity (Figure 33, Figure 102). This is due to the absence of oxygen after the milling of the powders. The laser cladding parameters were set up with a low power and an intermediate scanning speed between that of the S20.0 and of the S20.06. The first 2 layers were deposited as SS316L alone in order to avoid possible cracks at the interface. It is possible that these additional layers are not necessary. They present internal oxides visible with microscopy observation (Figure 97). However, the aim was to eliminate the porosities of the deposit with the 20% in volume of SiC, so the presence of oxides in the first two layers of SS316L was not investigated.

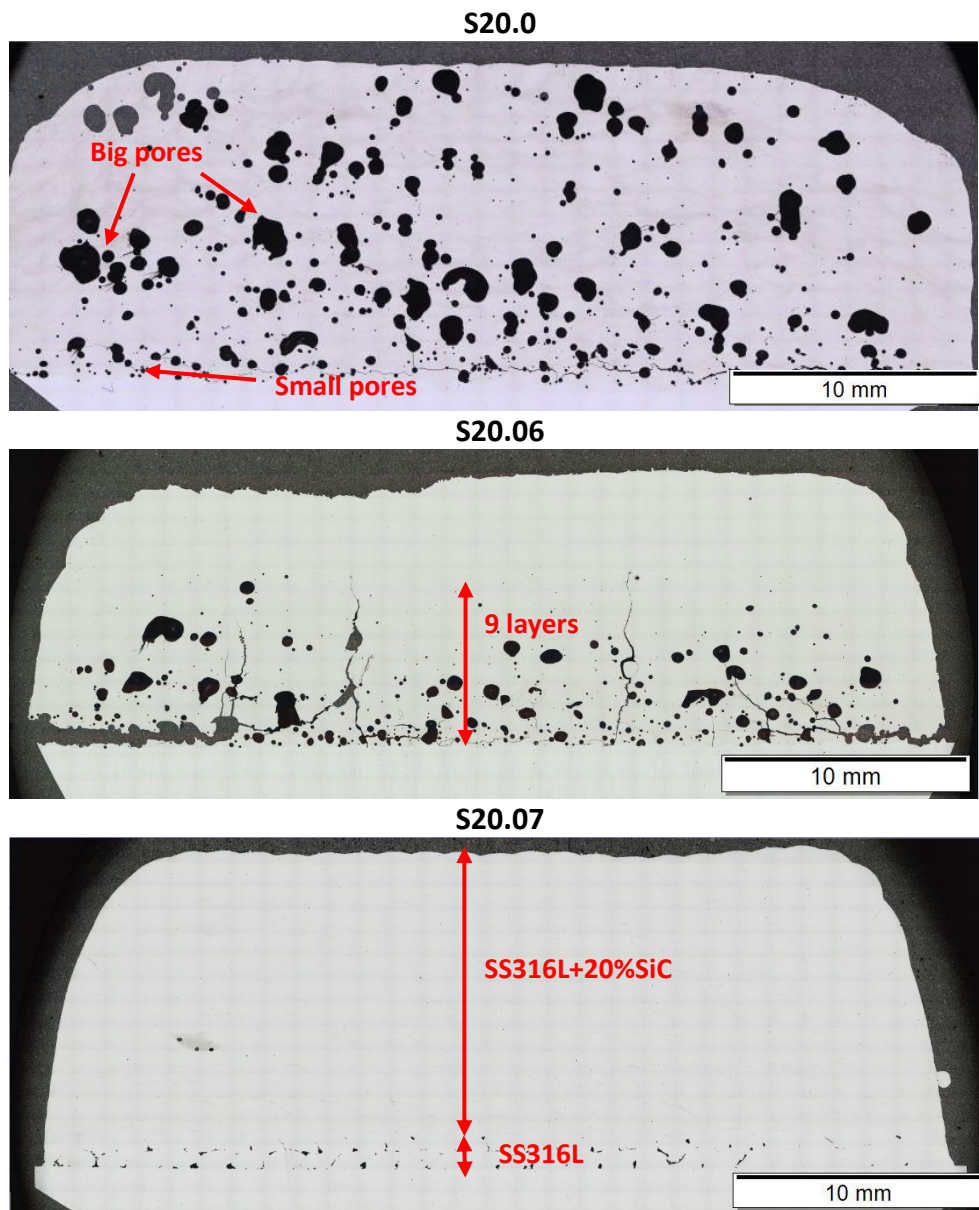


Figure 102: Evolution of SS316L+20%SiC cladded deposit

5.3 Evolution of SS316L with SiC addition

The classic microstructure of 316L Stainless Steel is modified by the addition of SiC. However, the characterization showed a microstructure without the presence of SiC. Final properties of the cladded deposit depend on the type, volume fraction and morphology of carbides, as well as on the properties of the matrix.

The presence of Cr leads to the formation of hard carbides, such as $M_{23}C_6$, M_7C_3 and M_3C_2 depending on Cr/C ratio [56]. Cr has desirable effects on the mechanical and physiochemical properties of the matrix alloy. However, an excessive precipitation of Cr carbides might deplete the Cr content of the stainless steel matrix hence compromising its corrosion resistance. Dutta Majumdar et al. [29] have shown that the corrosion resistance of a 316L+SiC cladded deposit is equivalent or better when compared with conventional SS316L [57]. The other element that increase the hardness of carbides and/or leads to strengthen the alloy matrix is Mo that promotes formation of M_7C_3 , M_2C and M_6C .

The microstructure of the cladded deposit of 316L + 10%SiC showed a better macro-hardness (348 HV) in comparison to the conventional cladded SS316L (200 HV) (chapter 4.2.1.3), because of the presence of hard carbides in the microstructure.

The presence of Mo and Cr leads to the formation of different phases in the S10, in particular in the track and in the heat affected zone. Microstructural observations on the track have shown a cellular/dendritic microstructure with primary austenite and eutectic $(Cr,Mo)_{23}C_6$ carbides among the cells (Figure 103), according to a similar morphology observed in a previous study [34]. One should notice that the typical size range of the phases in the as-cast process of the cited study is 10 μm , while in the current microstructure by laser cladding, this typical size is 1 μm .

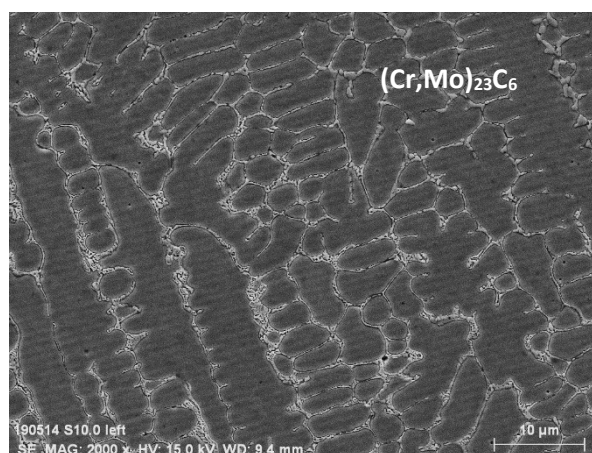


Figure 103: Track microstructure on sample S10.0

Meanwhile, Cr_7C_3 and Mo_2C carbides were found in the heat affected zone. Indeed, during the deposition of a new track, a heat affected zone is formed from the microstructure of the prior tracks. The heat affected zone presents modified carbides, and the precipitation of Cr_7C_3 and Mo_2C from $(\text{Cr},\text{Mo})_{23}\text{C}_6$. These two carbides are present in the intergranular spaces and they are characterized by a smooth boundary that clearly outline the interface with the matrix. However, they do not form two separately distinct phases, but they are connected by an undefined boundary. In the SEM observations of the heat affected zone, Cr_7C_3 are dark and with a globular shape, while the Mo_2C are bright with a lamellar shape (Figure 104).



Figure 104: Heat affected zone microstructure on sample S10.0

Table 30 list the chemical composition of the various phases.

		Atomic composition [%]						
		Phase	C	Fe	Cr	Mo	Si	Ni
		Matrix	4.7-14	55-64	12.5-14	0.5-0.8	4.5-6.6	10.5-11.5
<i>Track</i>		M_{23}C_6 eutectic	12-18	41-51	18-26	1.8-3.2	5-7	6-9
<i>HAZ</i>		Cr_7C_3	20-30	28-49	15-30	2-3	1.8-4.6	3.5-6
		Mo_2C	15-20	44-48	11-19	3.8-5.5	6.1-7.8	7.5-8.4

Table 30: Atomic composition [%] of phases on S10.0 microstructure

The eutectic carbide inside the track has an intermediate composition between the Cr_7C_3 and Mo_2C of the HAZ, while the matrix of the track is enriched in C, Si and depleted in Mo.

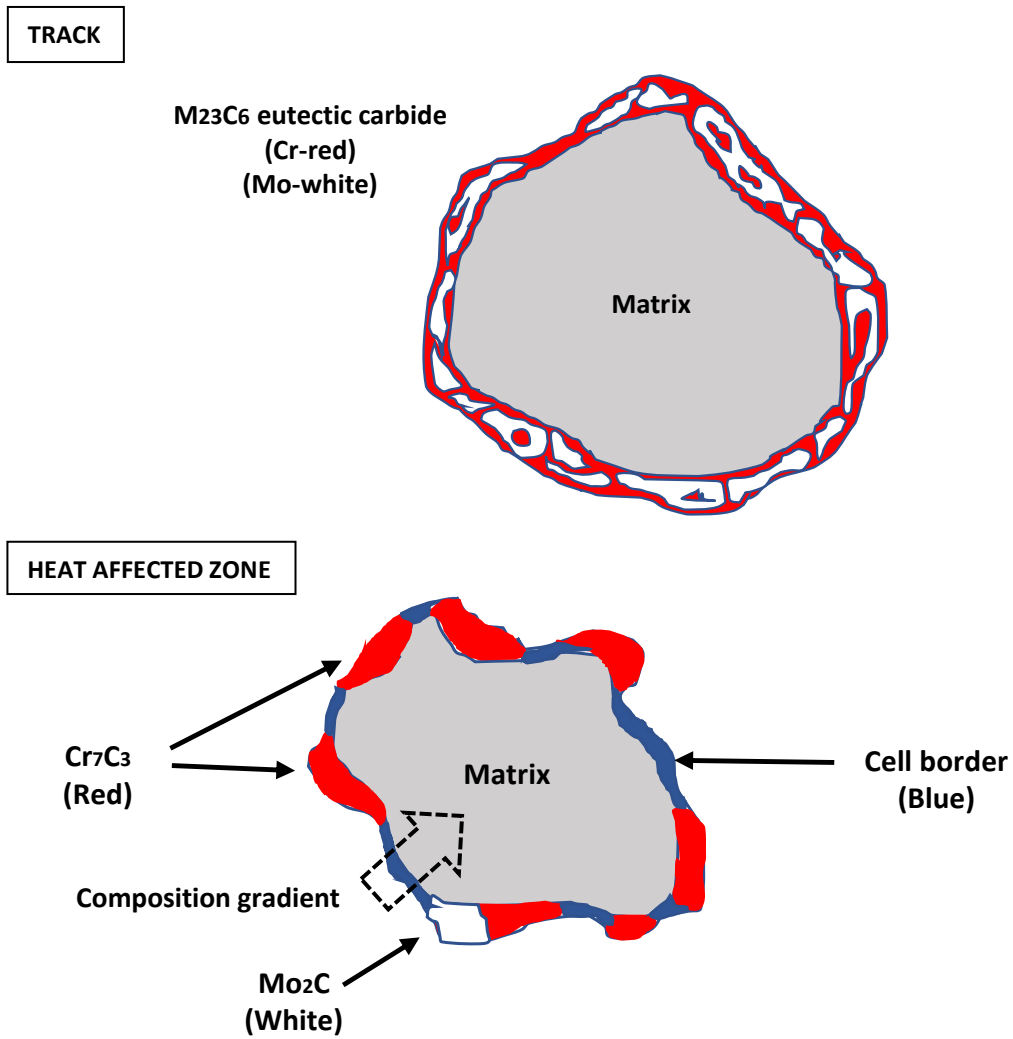


Figure 105: Schematic reconstruction of a single grain in the track and in the heat affected zone

The track is generally formed by a connected carbide network, while the heat affected zone present an unconnected structure with an inhomogeneous composition (Figure 105). In particular, some zones enriched in Si and Mo at the cell boundary could not be observed as shown in Figure 73. EBSD analysis revealed the presence of a distorted lattice in those boundaries since their indexation was lower than for the austenite of the neighbour cells.

Atomic composition [%]						
Phase	C	Si	Cr	Fe	Ni	Mo
Cell border	30,28	3,75	12,69	42,73	7,09	1,57
Matrix HAZ	24,42	3,59	11,87	49,02	8,32	0,85

Table 31: Atomic composition [%] of the grain and the cell border in the heat affected zone

The composition of the ‘cell border’ is intermediate between carbides and matrix (Table 31). This is due to the thermal gradient of the heat affected zone discussed above that leads to the degradation of the eutectic carbides. Most of Cr and Mo precipitate locally in preferential zone forming carbides, leaving the residual in the ‘cell border’ zone.

The EBSD revealed locally the presence of $(Fe,Mo)_3C$ and $(Cr,Mo)_{23}C_6$ carbides, but these carbides do not form an homogeneous phase, except for some small areas. $Cr_{23}C_6$ carbides are identified by EBSD as the same crystalline phase of austenite (Face-Centered Cubic FCC), so in the area where they are present as isolated points they are to be considered as austenite. The $(Fe,Mo)_3C$ carbide are identified as Base-Centered Monoclinic (BCM) crystalline structure. This is a consequence of an increased cooling rate during solidification that promotes a freezing of alloying element in the liquid. When the carbides are formed under such condition, they can exhibit crystal lattices that are different from the equilibrium conditions [58].

An important method to establish the solidification sequence consist in analysing the DTA heating curve by a reverse approach. In order to elucidate the solidification sequence, the DTA heating peaks are correlated with the chemical compositions and morphological features of the phases present in the microstructure. The cooling curve of the DTA test is not useful because there is a high difference between the cooling rate occurring during the laser cladding and during the DTA cooling step. Indeed, the formed microstructure is completely different in terms of dimensions: in the cladded deposit the typical size range is 10 μm , while in the sample after DTA test, it is about 100 μm .

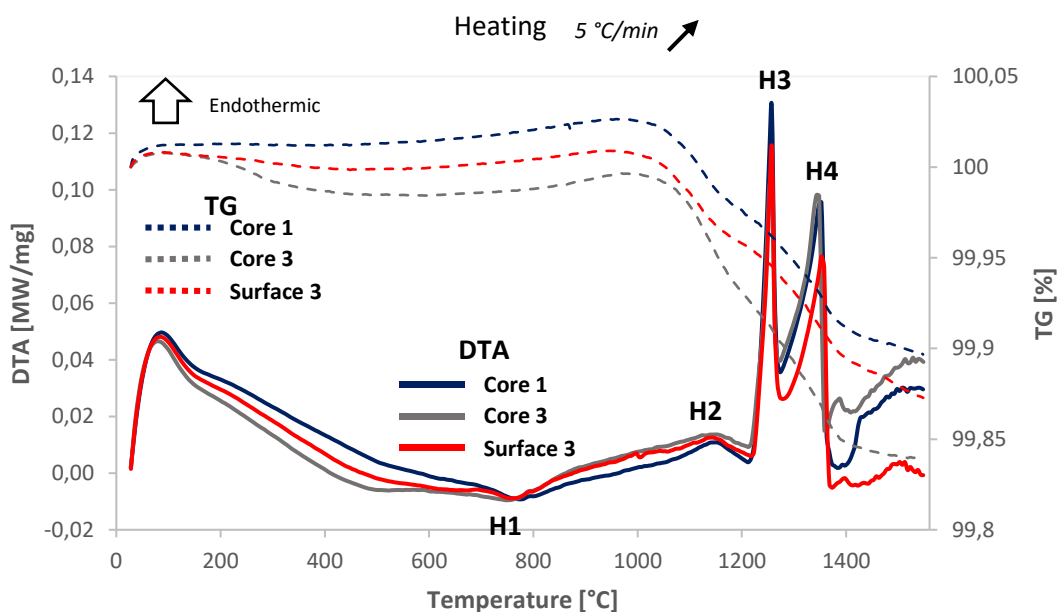


Figure 106: DTA & TG heating curves of SS316L+10%SiC cladded deposit

As explained in chapter 4.2.1.2, three different DTA tests were performed on the cladded 316L+10%SiC deposit (Figure 106). The three curves exhibit the same trend during heating. The only difference is in the curve 'Surface 3', where the peaks H3 and H4 have a lower height because of the smaller weight of the sample 'Surface 3' in comparison with the samples 'Core 1' and 'Core 3' (chapter 3.4.1). The TG curves trend is similar for the three samples. After a plateau until 1000°C, the temperature become critically for the material and the fusion starts. The transformations that occur above 1380°C are not useful for this analyse and they are not considered.

Following the peaks backwards, the solidification starts with the peak H4 (Figure 107). The precipitation of carbides starts at lower temperature, so the peak H4 corresponds to the formation of primary austenite. In fact there is a continuous change of the DTA derivative curves. It characterizes the matrix of the cladded deposit.

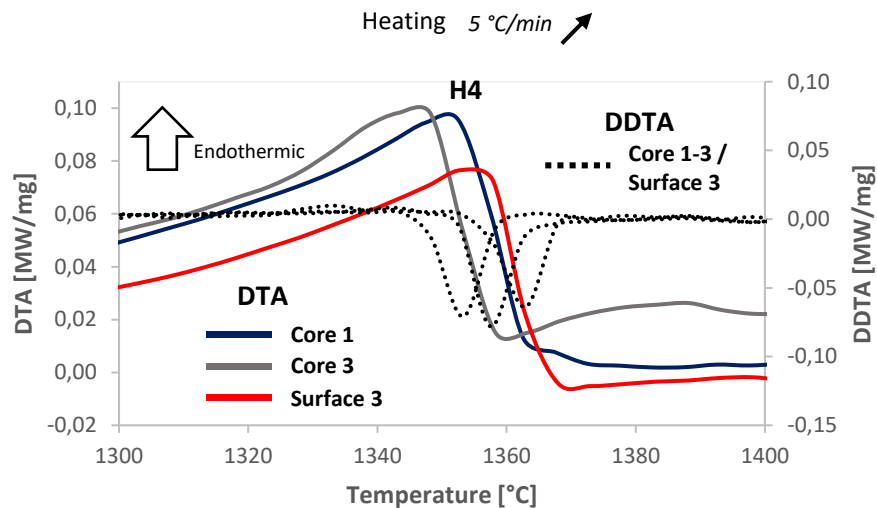


Figure 107: Focus on peak H4

The second constituent formed during the solidification (peak H3) is the $(Cr,Mo)_{23}C_6$ eutectic carbide located in the intercellular region (Figure 103). The derivative of the DTA curve (Figure 108) does not show a linear trend because of the melting of the Cr_7C_3 and Mo_2C observed in the heat affected zone [47]. Both carbides are formed in this range since their compositions are quite similar.

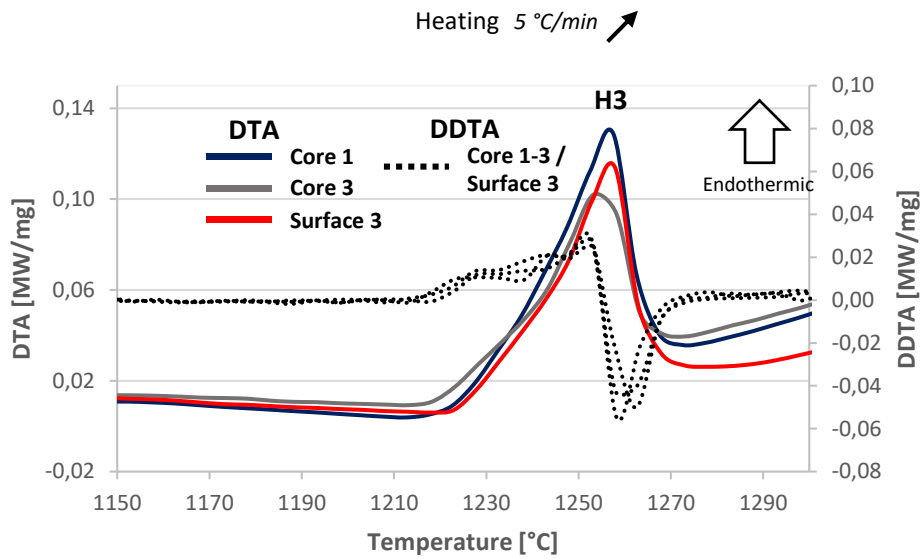


Figure 108: Focus on peak H3

Peak H2 was observed in the study cited above [47], but the nature of the corresponding phase is not clear, while peak H1 is unknown. Microscope observations and chemical analyses have been carried out, but modifications were not observed.

With the addition of 20% in volume of SiC the microstructure changes, due to higher amount of SiC and of porosities. In fact, the oxygen inside the SiC powders can obstacle the melt pool during the laser cladding process and forming different phases.

Two different carbides characterize the microstructure of the SS316L + 20% SiC cladded samples S20.0 and S20.06: M_7C_3 and M_6C (Figure 109). In this case M_7C_3 has a different morphology if compared to those of the sample S10.0, similar to that reported in literature [36], because of the higher amount of Cr and C. The size is larger as well, probably due to the presence of gas to and macro-segregation.

Mo promotes the formation of M_6C , characterized by the presence of a central platelet of M_6C carbide, from which secondary platelets of M_6C arises, separated from each other by austenite. These secondary platelets are usually thicker at the end, interrupting the continuity of the austenite [37]. M_6C and M_2C (present in the cladded deposit of SS316L + 10% SiC) are both a Fe – Cr – Mo phase but with different chemical composition.

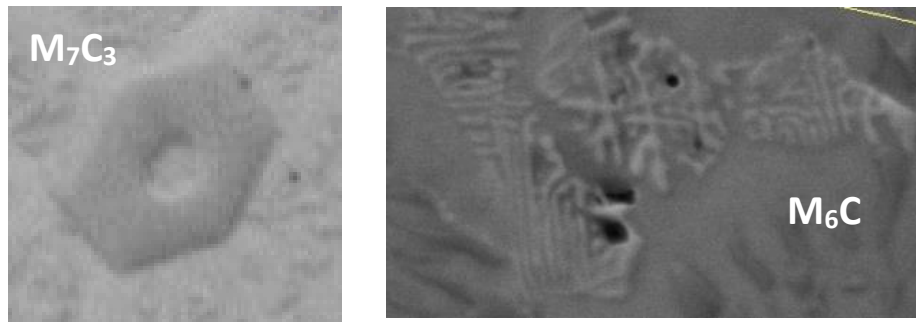


Figure 109: Phases present on samples S20.0 and S20.06

In Table 32 is shown the chemical composition of the phases.

Atomic composition [%]

Phase	C	Fe	Cr	Mo	Si	Ni
Matrix	9.4-15.7	49.5-59.5	6.7-14.3	0.4-0.8	8.4-13	9-11.2
Cr₇C₃	20.5-27.3	31.5-42.1	20.7-34	0.7-2	2.8-7	3-7.62
Mo₆C	12.2-15.8	43.1-48.8	7.8-9.4	2.9-3.9	14.4-14.5	12.2-12.5

Table 32: Atomic composition [%] of phases on S20.0 and S20.06 cladded deposit

All the formed phases, although they present the same elements as in the deposit S10.0, have a different composition.

Finally, the latest cladded deposit S20.07 with the pre-mill powders present a different microstructure similar to the sample S10.0. It is characterized by the presence of columnar and equiaxed dendrites with bigger grains (Figure 97). Any M₇C₃, M₂C or M₆C were observed, but in this sample were not done chemical analyses.

6 CONCLUSIONS

- The characterization of both volume percentages of SiC showed a complete dissolution of the SiC powder in the SS316L.
- Microstructure investigation of the SS316L + 10% SiC cladded deposit, chemical analysis and thermal analysis allowed to understand the phases formed and the solidification sequence. This deposit is formed by a SS316L matrix enriched in C and Si with $M_{23}C_6$ (M=Cr, Mo) eutectic carbides that formed columnar and equiaxed dendrites. The eutectic carbide is degraded in the Heat Affected Zone due to a thermal effect that leads to a locally precipitation of Cr and Mo with the formation of Cr_7C_3 and Mo_2C . Due to this, a single grain in the Heat Affected Zone exhibits a different composition in the border if compared with the centre. The microstructure is reinforced by the presence of those carbides, if compared with the unreinforced cladded SS316L. Indeed, the macro-hardness is increased from 200 HV to 350 HV.
- With the addition of 20% in volume of SiC, the microstructure exhibits the same phases but with different morphology, due to the presence of gas in the melt pool during the deposition. This element led to the formation of cracks and pores in the SS316L + 20% SiC cladded deposit. The reaction that occurred between the oxygen and the chemical constituent of powders led to a porous deposit.
- A tailored powder preparation was set up in order to achieve a sound deposit with the 20% in volume of SiC. When the SiC powders were milled with SS316L powders, the cladded deposit presented a good external surface without cracks and no internal porosity. This is due to the fracture and deformation of SiC powder occurring during milling that leads to the release of the trapped oxygen.
- There is a clear evolution of the SS316L + 20% SiC cladded deposit in terms of quality. The first sample exhibited porosities and cracks in the whole deposit. Subsequently, with the optimization of parameters of the Laser Cladding technology, porosities and cracks were restricted only in the first layers. Finally, thanks to the preparation of powders with milling process, the deposit was compact, and it did not exhibit porosities and cracks.

7 PROSPECTS

- In order to compare the microstructure of the cladded deposits with 10% and 20% of SiC in terms of dimensions and phases, characterization of the SS316L + 20% SiC with milled powders should be performed.
- As shown in the results of this work, the addition of SiC in a SS316L matrix improved the macro-hardness. In these terms, it is also interesting to investigate the nano-hardness in order to compare the result with other MMCs.
- Corrosion tests can be performed on the SS316L/SiC composite, in order to compare this property with the conventional SS316L.
- One of the challenge that leads to the addition of different material as reinforcements of SS316L is the improvement of its wear resistance. The characterization of SS316L+SiC cladded deposit showed the presence of Cr carbides, that are responsible of a high wear resistance. It will be interesting to check the wear behaviour of this composite.
- Possible fabrication of deposits with a mix of SS316L + 30% SiC milled powders

8 REFERENCES

- [1] Danninger H, de Oro Calderon R, Gierl-Mayer C. Powder Metallurgy and Sintered Materials. Ullmann's Encycl Ind Chem. 2017;1-57. doi:10.1002/14356007.a22_105.pub200
- [2] Martin TA, Causey DH, Sheffner AL, Wheeler AG, Currihan JR. Powder Metallurgy Methods and Applications. J Med Chem. 1967;10(6):1172-1176. doi:10.1021/jm00318a0460
- [3] Al-mangour B, Angeles L. Powder Metallurgy of Stainless Steel: State-of-the Art, Challenges, and Development.; 2016.
- [4] Li R, Shi Y, Wang Z, Wang L, Liu J, Jiang W. Densification behavior of gas and water atomized 316L stainless steel powder during selective laser melting. Appl Surf Sci. 2010;256(13):4350-4356. doi:10.1016/j.apsusc.2010.02.030
- [5] Metals – Alloy design and powder production for selective laser melting – Advanced Ceramics and Powder Metallurgy.
- [6] Popovich A, Sufiiarov V. Metal Powder Additive Manufacturing. Intech. 2016;i(tourism):13. doi:http://dx.doi.org/10.5772/57353
- [7] Salzman S. Characterizing Metal Oxide Coated Carbonyl Iron (CI) Particles using Microscopic Techniques. 2009;20(Ci):2-8.
- [8] GGP Metalpowder AG _ Products _ Ultralight Electrolytic Copper Powders.
- [9] Fritz V. Lenel. Powder metallurgy — principles and applications. Mater Des. 1981;2(4):223. doi:10.1016/0261-3069(81)90028-5
- [10] Matthey J, Dawes J, Bowerman R, Trepleton R. Introduction to the Additive Manufacturing Powder Metallurgy Supply Chain Exploring the production and supply of metal powders for AM processes. Technol Rev. 2015;(3):243-256. doi:10.1595/205651315X688686
- [11] Dongdong Gu. Laser Additive Manufacturing Of High Performance Material.
- [12] ISO (International Organization for Standardization) .
- [13] Udriou R. Powder Bed Additive Manufacturing Systems and Its Applications. Acad J Manuf Eng. 2012;10(4):122-129. http://eng.upt.ro/auif/Lucrari_PDF_2012_4/Udriou-1.pdf.
- [14] Komvopoulos K, Nagarathnam K. Processing and characterization of laser-gladded coating materials. J Eng Mater Technol Trans ASME. 1990;112(2):131-143. doi:10.1115/1.2903299
- [15] R. Vilar. Laser Cladding. J Laser Appl. 1999. doi:10.1007/978-3-319-56711-2_9
- [16] Laser cladding products & solutions. https://www.fst.nl/about/laser-cladding/.

- [17] Chawla N, Chawla KK. Metal matrix composites. *Met Matrix Compos.* 2013;9781461495:1-370. doi:10.1007/978-1-4614-9548-2
- [18] Miracle DB. Metal matrix composites - From science to technological significance. *Compos Sci Technol.* 2005;65(15-16 SPEC. ISS.):2526-2540. doi:10.1016/j.compscitech.2005.05.027
- [19] Rosso M. Ceramic and metal matrix composites: Routes and properties. *J Mater Process Technol.* 2006;175(1-3):364-375. doi:10.1016/j.jmatprotec.2005.04.038
- [20] Li J, Zhao Z, Bai P, et al. Tribological behavior of TiC particles reinforced 316Lss composite fabricated using selective laser melting. *Materials (Basel).* 2019;16(6). doi:10.3390/ma12060950
- [21] Salman O, Funk A, Waske A, Eckert J, Scudino S. Additive Manufacturing of a 316L Steel Matrix Composite Reinforced with CeO₂ Particles: Process Optimization by Adjusting the Laser Scanning Speed. *Technologies.* 2018;6(1):25. doi:10.3390/technologies6010025
- [22] Xu P, Lin C, Zhou C, Yi X. Wear and corrosion resistance of laser cladding AISI 304 stainless steel/Al₂O₃ composite coatings. *Surf Coatings Technol.* 2014;238:9-14. doi:10.1016/j.surfcoat.2013.10.028
- [23] Mertens A, L'hoest T, Magnien J, Carrus R, Lecomte-Beckers J. On the elaboration of metal-ceramic composite coatings by laser cladding. *Mater Sci Forum.* 2017;879(January):1288-1293. doi:10.4028/www.scientific.net/MSF.879.1288
- [24] Mancini E. Studio delle eterogeneità microstrutturali in un rivestimento composito a matrice metallica di acciaio inossidabile 316L e carburo di tungsteno. 2017.
- [25] Tang WM, Zheng ZX, Ding HF, Jin ZH. A study of the solid state reaction between silicon carbide and iron. *Mater Chem Phys.* 2002;74(3):258-264. doi:10.1016/S0254-0584(01)00480-1
- [26] Tang WM, Zheng ZX, Ding HF, Jin ZH. Control of the interface reaction between silicon carbide and iron. *Mater Chem Phys.* 2003;80(1):360-365. doi:10.1016/S0254-0584(02)00521-7
- [27] Patankar SN, Tan MJ. Role of reinforcement in sintering of SiC/316L stainless steel composite. *Powder Metall.* 2000;43(4):350-352. doi:10.1179/003258900666078
- [28] Brytan Z, Dobrzański LA, Pakieła W. Laser surface alloying of sintered stainless steels with SiC powder. 2011;47(1):42-56.
- [29] Majumdar JD, Li L. Studies on direct laser cladding of SiC dispersed AISI 316L stainless steel. *Metall Mater Trans A Phys Metall Mater Sci.* 2009;40(12):3001-3008. doi:10.1007/s11661-009-0018-8
- [30] Peckner D, I.M. Bernstein. *Handbook Of Stainless Steels.*

- [31] Zhang Y, Xi M, Gao S, Shi L. Characterization of laser direct deposited metallic parts. *J Mater Process Technol.* 2003;142(2):582-585. doi:10.1016/S0924-0136(03)00663-0
- [32] Lee Y, Nordin M, Babu SS, F. D. Effect of Fluid Convection on Dendrite Arm Spacing in Laser Deposition. 2014.
- [33] Suutala N, Takalo T, Moisio T. The relationship between solidification and microstructure in austenitic and austenitic-ferritic stainless steel welds. *Metall Trans A.* 1979;10(4):512-514. doi:10.1007/BF02697081
- [34] Wiczerzak K, Bala P, Stepien M, Cios G, Koziel T. Formation of eutectic carbides in Fe-Cr-Mo-alloy during non-equilibrium crystallization. *Mater Des.* 2016;94:61-68. doi:10.1016/j.matdes.2016.01.028
- [35] Marya M, Singh V, Marya S, Hascoet JY. Microstructural Development and Technical Challenges in Laser Additive Manufacturing: Case Study with a 316L Industrial Part. *Metall Mater Trans B Process Metall Mater Process Sci.* 2015;46(4):1654-1665. doi:10.1007/s11663-015-0310-5
- [36] Liu S, Zhou Y, Xing X, Wang J, Ren X, Yang Q. Growth characteristics of primary M₇C₃ carbide in hypereutectic Fe-Cr-C alloy. *Sci Rep.* 2016;6(May):1-8. doi:10.1038/srep32941
- [37] Boccalini M, Goldenstein H. Solidification of high speed steels. *Int Mater Rev.* 2001;46(2):92-115. doi:10.1179/095066001101528411
- [38] CES Edu Pack 2018.
- [39] Narushima T, Goto T, Hirai T, Iguchi Y. High-temperature oxidation of silicon carbide and silicon nitride. *Mater Trans JIM.* 1997;38(10):821-835. doi:10.2320/matertrans1989.38.821
- [40] Greenmat - Portail.
- [41] Höganäs AB. Metal powders | Höganäs. 2018. <https://beta.hoganas.com/>.
- [42] H.C. Starck Ceramics GmbH. <https://www.hcstarck.com/en/home.html>
- [43] FRITTSCH <https://www.fritsch-international.com/sample-preparation/milling/ball-mills/>
- [44] Vandormael D. Sirris: driving industry by technology. *Aerosol Jet Print.* <http://sirris.be/aerosol-jet-printing>.
- [45] Irepa Laser _ laser industriel, fabrication additive et formation laser. <https://www.irepa-laser.com/>
- [46] coating equipment powder - medicoat <http://www.medicoat.com/>
- [47] Enrici TM. Microstructural and Thermal Characterization of 316L+WC Composite Coatings by Laser Cladding. 2018:2018.
- [48] Metallographic products, knowledge and service , Struers. <https://www.struers.com/>
- [49] OLYMPUS Global . <http://www.olympus-global.com/en/>.

- [50] Philips XL 30 SEM _ SEMTech Solutions <https://www.semtechsolutions.com>
- [51] NETZSCH [www.https://www.netzsch-thermal-analysis.com/en/](http://www.netzsch-thermal-analysis.com/en/).
- [52] EMCO-TEST __ Hardness testing machines acc. <https://www.emcotest.com/en/>
- [53] AlMangour B, Grzesiak D, Yang JM. Selective laser melting of TiB₂/316L stainless steel composites: The roles of powder preparation and hot isostatic pressing post-treatment. *Powder Technol.* 2017;309(March):37-48. doi:10.1016/j.powtec.2016.12.073
- [54] Mosca E. *ATMOSFERE CONTROLLATE NELLA METALLURGIA DELLE POLVERI* Teoria e pratica. :1-35.
- [55] de Oro Calderon R, Gierl-Mayer C, Danninger H. Application of thermal analysis techniques to study the oxidation/reduction phenomena during sintering of steels containing oxygen-sensitive alloying elements. *J Therm Anal Calorim.* 2017;127(1):91-105. doi:10.1007/s10973-016-5508-5
- [56] Venkatraman M, Neumann JP. The C-Cr (Carbon-Chromium) System. *Bull Alloy Phase Diagrams.* 1990;11(2):152-159. doi:10.1007/BF02841701
- [57] Mertens A, Lecomte-Beckers J. On the rule of interfacial reactions, dissolution and secondary precipitation during the laser additive manufacturing of metal matrix composites: a review. doi:<http://dx.doi.org/10.5772/57353>
- [58] Maurizi Enrici T. Elucidation of the solidification sequence of a complex graphitic HSS alloy under a combined approach of DTA and EBSD analyses. 2019.

9 ANNEXES

Annex 1: Datasheet SS316L powder



Item name
316 L-5520

Item number
111904

Quantity
40.0

Unit
Kg

Your reference
ULG18/1800413/R

CERTIFICATE OF ANALYSIS Page 1(1)

Lot number
2524517

Order no.
0010300939


Production date
2018-01-30

Delivery
2079360

Shippers
3410286

Customer
UNIVERSITE DE LIEGE

Address
**Adm.Factis lin. service controle fact.
Place de Virgi-Aoûl 7
S-4000 LIEGE
Belgium**

	Test result	Unit	Specification		ISSUE 1
			MIN	MAX	
CHEMICAL PROPERTIES					
Carbon	0.015	%		0.030	%
Molybdenum	2.5	%	2.0	3.0	%
Nickel	12.6	%	10.0	14.0	%
Iron Is BALANCE					
Manganese	1.5	%	1.0	2.0	%
Chromium	16.0	%	16.0	18.0	%
Silicon	0.7	%		1.0	%
PHYSICAL PROPERTIES					
Apparent density (Hall)	4.14	g/cm ³			
Flowrate (Hall)	17.3	sec/50g			
SIEVE ANALYSIS					
+180 Microns	0.00	%		0.00	%
+150 Microns	0.04	%		3.00	%
+125 Microns	3.84	%		25.00	%
+106 Microns	13.20	%			
+71 Microns	49.46	%			
+63 Microns	23.58	%			
+53 Microns	9.02	%		15.00	%
+45 Microns	0.84	%		1.00	%
-45 Microns	0.02	%		0.20	%
			Approved by		
					
			Quality Control Manager		

COMMITTEE: H00044-04

Höganäs Belgium S.A. Ruelle De la Pierre 16 B-1300 ATH	Telephone Fax	32 62 261669 32 62 261779	Höganäs Höganäs Sand AB, Fuchuan Branch SHANGHAI - HONGKONG SHANGHAI (CHINA) - CE 113 1163 8308 8802 8808 01 SHANGHAI (CHINA) - CE 113 1163 8308 8802 8808 02 SHANGHAI (CHINA) - CE 113 1163 8308 8802 8808 03	EPN01 France BE 0420 056 801
--	------------------	------------------------------	--	---------------------------------

Annex 2: Datasheet SiC powder



Number PD-9020
Issue 1-29.03.2016

STARCERAM[®] S rtp Grade RQ

Chemical Formula	SiC
Chemical Name	Silicon Carbide
Description of Product	Formulation of silicon carbide and processing additives for pressing, green machining and sintering.

Chemical Characteristics (Mass fraction in wt %)

C	31	-	33	%
B	0.3	-	0.5	%
O	max.		5	%
Fe	max.		0.2	%
Al	max.		0.04	%
Ca	max.		0.01	%

Physical Characteristics (Granule- Size-Distribution vol %)¹⁾

> 200 µm	max.	2	%
< 38 µm	max.	35	%

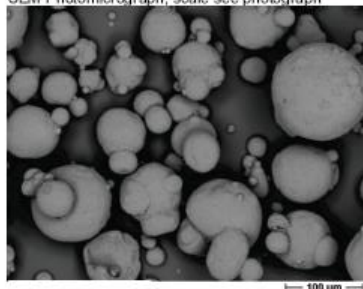
Green Density ²⁾	1.8	-	1.9	g/cm ³
Sintered Density ³⁾	3.10	-	3.15	g/cm ³
Apparent Density ⁴⁾	0.8	-	0.95	g/cm ³

The data indicated relates to the test specimens from which it was obtained and is not unconditionally applicable to other forms of the same material. The data must, therefore, be regarded as indicative only.

1) Beckmann Coulter by Laser Light Diffraction, dry dispersion per ISO 13320, 2)1000 kg/cm², 3) 2100°C, Ar, 0 bar, 4) EN 725-9.

Product Description and Applications

SEM Photomicrograph; scale see photograph



- Packaging** 50 kg steel drums with polyethylene inlet, (60 Liter) 6 drums on euro-pallet (800x1200) = 1 Packaging unit of 300 kg. Other packaging/quantity on request.
- Storage and Handling** STARCERAM® S rlp, as a complex system of organic and inorganic ingredients, is made for early usage. The self-life for unrestricted processability is dependent on the storage conditions and the specific application it is used for. Storage and handling are subject to the rules and regulations in the country of use. Store at room temperature in sealed closed, original container.
- Hazards identification in Advertising (REGULATION (EC) No 1272/2008 Article 48)** Skin sensitisation Category 1.
- Documentation** An inspection document in accordance with EN 10204 is supplied with every shipment.

H.C. Starck Ceramics GmbH
Lorenz-Hulschenreuther-Str. 81
95100 Selb/Germany
Phone +49 9287 807-0, Fax +49 9287 807-477

[Further contact addresses](#)

info@hcastarck.com

www.hcastarck.com

The conditions of your use and application of our products, technical assistance and information (whether verbal, written or by way of production evaluations), including any suggested formulations and recommendations, are beyond our control. Therefore, it is imperative that you test our products, technical assistance and information to determine to your own satisfaction whether they are suitable for your intended uses and applications. This application-specific analysis at least must include testing to determine suitability from technical as well as health, safety, and environmental standpoint. Such testing has not necessarily been done by H.C. Starck. All information is given without warranty or guarantee. It is expressly understood and agreed that the customer assumes and hereby expressly releases H.C. Starck from all liability, in tort, contract or otherwise, incurred in connection with the use of our products, technical assistance and information. Any statement or recommendation not contained herein is unauthorized and shall not bind H.C. Starck. Nothing herein shall be construed as a recommendation to use any product in conflict with patents covering any material or its use. No license is implied or in fact granted under the claims of any patent. In case of order please refer to issue number of the respective product data sheet. All deliveries are based on the latest issue of the product data sheet and the latest version of our General Conditions of Sale and Delivery.